



ANALYSIS, SIMULATION AND OPTIMIZATION OF VENTILATION OF ALUMINUM SMELTING CELLS AND POTROOMS FOR WASTE HEAT RECOVERY

**Thèse
Ruijie Zhao**

Doctorat en génie mécanique
Philosophiae Doctor (Ph.D.)

Québec, Canada

© Ruijie Zhao, 2015

RÉSUMÉ

En raison des quantités d'énergie requises par la production primaire d'aluminium et le rendement relativement faible, les rejets thermiques de cette industrie sont énormes. Ils sont par contre difficiles à utiliser à cause de leur faible température. De plus, tout changement apporté pour augmenter la température des rejets peut avoir un impact important sur la production. La compréhension du transfert thermique et de l'écoulement d'air dans une cuve peut aider à maintenir les conditions de la cuve lorsque des modifications y sont apportées. Le présent travail vise à développer cette compréhension et à apporter des solutions pour faciliter la capture des rejets thermiques.

Premièrement, un circuit thermique est développé pour étudier les pertes thermiques par le dessus de la cuve. En associant des résistances thermiques aux paramètres physiques et d'opération, une analyse de sensibilité par rapport aux paramètres d'intérêt est réalisée pour déterminer les variables qui ont le plus d'influence sur la qualité thermique des rejets de chaleur dans les effluents gazeux. Il a été montré que la réduction du taux de ventilation des cuves était la solution la plus efficace. Ensuite, un modèle CFD a été développé. Un bon accord a été trouvé entre les deux modèles.

Deuxièmement, une analyse systématique de la réduction de la ventilation des cuves a été réalisée par la simulation CFD. Trois problèmes qui peuvent survenir suite à une réduction du taux de ventilation sont étudiés et des modifications sont proposées et vérifiées par des simulations CFD. Le premier problème, maintenir les pertes thermiques via le dessus de la cuve, peut être résolu en exposant davantage les rondins à l'air pour augmenter les pertes radiatives. Le second problème soulevé par la réduction de ventilation concerne les conditions thermiques dans la salle des cuves et une influence limitée de la ventilation est observée par les simulations. Finalement, l'étanchéité des cuves est augmentée par une réduction des ouvertures de la cuve de manière à limiter les émissions fugitives sous des conditions de ventilation réduite. Les résultats ont révélé qu'une réduction de 50% du taux de ventilation est techniquement réalisable et que la température des effluents d'une cuve peut être augmentée de 50 à 60°C.

ABSTRACT

Due to the high energy requirement and ~50% efficiency of energy conversion in aluminum reduction technology, the waste heat is enormous but hard to be recovered. The main reason lay in its relatively low temperature. Moreover, any changes may affect other aspects of the production process, positively or negatively. A complete understanding of the heat transfer and fluid flow in aluminum smelting cells can help to achieve a good trade-off between modifications and maintenance of cell conditions. The present work aims at a systematic understanding of the heat transfer in aluminum smelting cell and to propose the most feasible way to collect the waste heat in the cell.

First, a thermal circuit network is developed to study the heat loss from the top of a smelting cell. By associating the main thermal resistances with material or operating parameters, a sensitivity analysis with respect to the parameters of interest is performed to determine the variables that have the most potential to maximize the thermal quality of the waste heat in the pot exhaust gas. It is found that the reduction of pot draft condition is the most efficient solution. Then, a more detailed Computational Fluid Dynamics (CFD) model is developed. A good agreement between the two models is achieved.

Second, a systematic analysis of the reduction of draft condition is performed based on CFD simulations. Three issues that may be adversely affected by the draft reduction are studied and corresponding modifications are proposed and verified in CFD simulations. The first issue, maintaining total top heat loss, is achieved by exposing more anode stubs to the air and enhancing the radiative heat transfer. The second one is to verify the influence of the draft reduction on the heat stress in potroom and limited influence is observed in the simulations. Finally, the pot tightness is enhanced by reducing pot openings in order to constrain the level of fugitive emissions under reduced pot draft condition. The results have revealed that 50% reduction in the normal draft level is technically realisable and that the temperature of pot exhaust gas can be increased by 50-60 °C.

CONTENT

RÉSUMÉ.....	iii
ABSTRACT.....	v
CONTENT.....	vii
TABLE LIST.....	xi
FIGURE LIST.....	xiii
NOMENCLATURE.....	xvii
ACKNOWLEDGEMENTS	xxi
FOREWORD.....	xxiii
CHAPTER 1 INTRODUCTION.....	1
1.1 Introduction.....	2
1.2 Current progress.....	3
1.2.1 Mathematical models of the electrolytic cell	3
1.2.2 Top heat transfer in smelting cells	5
1.2.3 Sidewalls heat transfer in smelting cells	7
1.2.4 Fluoride emissions from electrolytic cells	9
1.2.5 Heat and mass transport in potroom	10
1.3 Problematic and objectives	10
1.4 Overview.....	12
CHAPTER 2 HEAT TRANSFER IN UPPER PART OF ELECTROLYTIC CELLS: THERMAL CIRCUIT AND SENSITIVITY ANALYSIS.....	15
Abstract.....	16
2.1 Introduction.....	18
2.2 Description of the system	20
2.3 Thermal circuit representation	21
2.3.1 Conduction and convection sub-network.....	24
2.3.2 Radiation sub-network	28
2.4 Resistance of fin-like components with internal heat generation	29
2.5 Numerical implementation and validation.....	34
2.6 Effect of ventilation rate	37
2.7 Effect of heat transfer coefficients on different surfaces.....	40
2.8 Effect of the surface emissivity	44
2.9 Influence of hoods insulation.....	46
2.10 Influence of the potroom air temperature	48

2.11	Influence of anode height	50
2.12	Conclusions.....	52
CHAPTER 3 HEAT TRANSFER AND AIRFLOW ANALYSIS IN UPPER PART OF ELECTROLYTIC CELLS BASED ON CFD		55
	Abstract.....	56
3.1	Introduction.....	58
3.2	CFD Model	59
3.2.1	Domain.....	59
3.2.2	Governing equations and modeling options	62
3.2.3	Boundary conditions	66
3.3	Model verification	68
3.3.1	Verification of mesh requirements.....	68
3.3.2	Validation with literature	69
3.4	Comparison between CFD simulations and a thermal resistance circuit model.....	71
3.5	Correlations for average convection coefficients	75
3.6	Spatial variations of the local convection coefficients	79
3.7	Forced versus natural convection	81
3.8	Pressure drop-flow rate relationship.....	83
3.9	Conclusions.....	85
CHAPTER 4 REDUCED VENTILATION OF UPPER PART OF ALUMINUM SMELTING POT: POTENTIAL BENEFITS, DRAWBACKS, AND DESIGN MODIFICATIONS.....		87
	Abstract.....	88
4.1	Introduction.....	90
4.2	CFD Model	91
4.2.1	Simplifying Assumptions	91
4.2.2	Governing Equations	92
4.2.3	Turbulence Model	93
4.2.4	Numerical Modeling and Mesh	94
4.2.5	Boundary Conditions	95
4.3	Verification and Validation	96
4.4	Top Heat Loss in Current Pots under Normal and Reduced Ventilation Rates.....	98
4.5	Addition of Fins on Anode Assembly	100
4.6	Modification of Hood Gaps Geometry	102

4.7	Modifications on Anode Cover	105
4.8	Conclusions.....	106
CHAPTER 5 AIRFLOW AND THERMAL CONDITIONS IN ALUMINUM SMELTING POTROOMS UNDER DIFFERENT CONDITIONS		107
	Abstract.....	108
5.1	Introduction.....	110
5.2	Description of the ventilation in potrooms	112
5.3	CFD modeling	113
5.3.1	Description of the numerical domain.....	113
5.3.2	Governing equations	115
5.3.3	Boundary conditions	117
5.3.4	Mesh independence study	122
5.4	Model validation from measurements in potroom.....	123
5.5	Ventilation and thermal conditions in potroom under different pot ventilations	126
5.5.1	Outdoor condition scenarios	127
5.5.2	Effect of pot ventilation reduction on potroom ventilation	127
5.5.3	Effect of pot ventilation reduction on temperature distribution in potroom	129
5.6	Assessment of body heat stress under different pot ventilations	132
5.7	Conclusions.....	137
CHAPTER 6 ESTIMATION OF THE EFFICIENCY OF POT TIGHTNESS IN REDUCED POT DRAFT BASED ON CFD SIMULATIONS.....		139
	Abstract.....	140
6.1	Introduction.....	142
6.2	Description of pot ventilation principles	144
6.3	Numerical model	147
6.3.1	Computational domains and simplifying assumptions	147
6.3.2	Governing equations	148
6.3.3	Boundary conditions	151
6.3.4	Mesh independence study	153
6.4	Model validation.....	153
6.5	Pot tightness in various pot conditions	155
6.5.1	Effect of different pot drafts	155
6.5.2	Effect of the gap space between hoods	160

6.5.3	Effect of air flow pattern in potroom	162
6.5.4	Effect of the crust conditions (crust integrity and heat flux on it)	163
6.6	Improvement of pot tightness	164
6.6.1	Installation of fiber brushes	165
6.6.2	Covering of the lower half of the gaps between hoods.....	165
6.7	Conclusions.....	168
CHAPTER 7 CONCLUSIONS AND FUTURE WORK		169
7.1	Mechanism of heat transfer in the upper part of an aluminum smelting cell	170
7.2	The reduction of pot draft condition	171
7.2.1	Heat management in reduced pot draft	172
7.2.2	Heat stress of potroom in reduced pot draft.....	172
7.2.3	Pot tightness and emission control in reduced pot draft	173
7.2.4	Other “side” contributions of this thesis	173
7.3	Future work.....	174
REFERENCES.....		177
APPENDIX.....		185

TABLE LIST

Table 2.1	Correlations for average convection coefficients on four surfaces of the cavity, as a function of volumetric flow rate Q for one pot [Nm^3/s] (Zhao et al. 2013).....	24
Table 2.2	Best-fits for electrical resistivity of aluminum and steel.....	27
Table 2.3	Thermo-physical parameters considered in the calculations.....	36
Table 3.1	Boundary conditions used in the present study.....	67
Table 3.2	Thermal conductivity and Joule heating source term for aluminum and steel.....	68
Table 3.3	Comparison of the results of the present work with other results taken from literature.....	71
Table 3.4	Correlations for average convection coefficients on four surfaces of the cavity, as a function of volumetric flow rate Q for one pot [Nm^3/s] and the average and maximum relative error between correlations and CFD results.....	78
Table 4.1	Comparison of CFD results with two meshes, for two ventilation conditions (shaded lines are for reduced ventilation).....	97
Table 4.2	Convection and radiation heat transfer enhancement (in W) provided by different scenarios compared to case_1/2.....	104
Table 5.1	Pressure boundary conditions [Pa].....	119
Table 5.2	Imposed thermal boundary conditions.....	122
Table 5.3	Effect of the mesh on the parameters of interest.....	123
Table 5.4	Temperature difference between CFD results and measurements, in K	126

FIGURE LIST

Figure 2.1	Representation of the upper part of a typical electrolytic cell with its main components.....	21
Figure 2.2	Thermal circuit representation of Fig. 1, with: (b) convection and conduction sub-network, and (c) radiation sub-network.....	23
Figure 2.3	Example of a fin-like element and its thermal resistance representation	33
Figure 2.4	The variation of the off gas temperature and its heat content with the draft conditions Q (effluents volumetric flow rate for one pot in ADQ), $2.4\text{Nm}^3/\text{s}$ is the normal ventilation condition in ADQ.....	38
Figure 2.5	Effect of the pot ventilation rate Q on: a) the temperature of the components of the superstructure, and b) the heat transfer rate through these components.....	39
Figure 2.6	Effect on gas temperature of increasing convection coefficients on different surfaces on the gas temperature for: a) normal ventilation rate, and b) reduced ventilation rate (40% of normal draft). (c, h, r, ys represent anode cover, hood and superstructure, rod and yoke and stubs respectively)	42
Figure 2.7	Effect on heat transfer rates of increasing convection coefficients on different surfaces on the gas temperature for: a) normal ventilation rate, and b) reduced ventilation rate (40% of normal draft).....	43
Figure 2.8	Effect of the emissivity of hoods on: a) the temperature of different components, and b) the heat transfer rates through these components.....	45
Figure 2.9	Effect of the hoods insulation on: a) the temperature of different components, and b) the heat transfer rates through these components.....	47
Figure 2.10	Effect of the potroom air temperature on: a) the temperature of different components, and b) the heat transfer rates through these components.....	49
Figure 2.11	Effect of the height of anodes on: a) the temperature of different components, and b) the heat transfer rates through these components.....	51
Figure 3.1	The structure of an aluminum reduction cell, (a) complete view, and (b) simulated domain consisting in the top portion of the cell.....	61

Figure 3.2	y^+ distribution (a) on the surfaces of anode cover and anode assembly; (b) on the internal surfaces of hoods and superstructure.....70
Figure 3.3	Comparison between average temperatures obtained from the CFD model and from the thermal resistance circuit (TRC) model, as a function of the ventilation, for: (a) the exhaust gas (including Gadd's experiments); (b) the top surface of the anode cover; (c) the surfaces of hoods and superstructure; and (d) the base of aluminum rod.....73
Figure 3.4	Comparison between heat transfer rates obtained from the CFD model and from the thermal resistance circuit (TRC) model, as a function of the ventilation, for: (a) heat content in exhaust gas; (b) radiation heat transfer from the top surface of the anode cover; (c) radiation heat transfer on the surfaces of hoods and superstructure; and (d) radiation heat transfer from the surfaces of yoke and stubs (y,s).....75
Figure 3.5	Average convection coefficients (solid symbols) and correlations (red lines) with variable draft conditions, (a) on the top surface of anode cover, (b) on the surface of hoods and superstructure, (c) on the surface of rod, (d) on the surface of yoke and stubs.....77
Figure 3.6	(a) Local convection coefficient h_{cover} ($W/m^2 \cdot K$) on the top of anode cover in normal draft condition; (b) local convection coefficient h_{ys} ($W/m^2 \cdot K$) on the surface of the anode assembly in normal draft condition.....80
Figure 3.7	Average forced and mixed convection coefficients with variable draft conditions, (a) average convection coefficients on the top surface of anode cover, (b) average convection coefficients on the surface of hoods and superstructure, (c) average convection coefficients on the surface of rod, (d) average convection coefficients on the surface of yoke and stubs.....83
Figure 3.8	Inlet-to-outlet pressure drop (solid symbols) and correlation (red line) versus draft condition.....85
Figure 4.1	Schematic view of the domain of the CFD model.....93
Figure 4.2	Heat losses due to convection and radiation from different components in different ventilation conditions.....99
Figure 4.3	Schematic of fins addition on anode assembly (case a2).....101

Figure 4.4	The difference of heat transfer rate extracted from bath by the top of the cell between normal condition and simulated scenarios.....	101
Figure 4.5	Schematics of sealed hood gaps (case b1, left) and horizontal hood gaps (case b2, right).....	104
Figure 4.6	Schematic of more exposed stubs in the cavity (case c2).....	106
Figure 5.1	(a) A plan of the studied smelter and (b) simulated domain representing a slice of potroom.....	114
Figure 5.2	Positions where temperature measurements were performed.....	125
Figure 5.3	Air mass flow rate through different potroom openings under both normal and reduced pot ventilations.....	129
Figure 5.4	Air temperature profile in the middle plane of the sliced potroom under: (a) normal and (b) 50% reduced pot ventilations.....	131
Figure 5.5	Air temperature profile on a horizontal surface at height of 1.3 m above the catwalk floor under: (a) normal and (b) 50% reduced pot ventilations...	131
Figure 5.6	Temperature on hoods and superstructure under: (a) normal and (b) 50% reduced pot ventilations.....	132
Figure 5.7	Mean radiant temperature on a horizontal surface at a height of 1.3 m above the catwalk floor under (a) normal and (b) 50% reduced pot ventilations.....	132
Figure 5.8	Comparison of the estimated DLE in 3 scenarios with normal pot ventilation.....	135
Figure 5.9	Difference of DLE between normal and 50% reduced pot ventilations, in 3 scenarios.....	136
Figure 5.10	Vertical distribution of the DLE in scenario 1, under 50% reduced pot ventilation.....	137
Figure 6.1	Three CFD sub-models considered in this work: (a) potroom model; (b) sliced pot model; (c) a 3D slice of potroom.....	145
Figure 6.2	Schematic representation of the pressure difference distribution along the hoods.....	147

Figure 6.3	Comparison of flow patterns between smoke tests and CFD results, (a) airflow in smoke tests; (b) airflow streamlines in the <i>potroom model</i> ; (c) airflow streamlines in the <i>sliced pot model</i>	156
Figure 6.4	Flow pathlines starting from the hood gaps under different scenarios: (a) normal pot draft condition; (b) 50% reduced draft condition; (c) 50% reduced draft condition and one hood slid down.....	158
Figure 6.5	Static pressure profile at a cross-section 0.85 m away from the central-plan of the pot in the <i>sliced pot model</i> under different scenarios: (a) normal pot draft condition; (b) 50% reduced draft condition; (c) 50% reduced draft condition with the modification of coving of the lower half of hood gaps.	159
Figure 6.6	Estimated additional equivalent HF emissions in different scenarios of hood placement under both normal and 50% reduced draft conditions... ..	162
Figure 6.7	Static pressure on the pot shell due to the air flow in potroom, (a) normal draft condition; (b) 50% reduced draft condition.....	164
Figure 6.8	schematic representation illustrating the sealing of the lower half of hood gaps.....	166
Figure 6.9	Additional equivalent HF emissions from the pot when reducing the draft by half and sealing the lower half of the gaps between hoods, under different hood placement scenarios.....	167

NOMENCLATURE

A	surface area, m^2
Al	abbreviation of aluminum
A_f	free area or total area of the holes, m^2
A_p	area of the plate (solid and holes), m^2
a	constant of the best fit for electrical resistivity, $\Omega \cdot m$
b	constant of the best fit for electrical resistivity, $\Omega \cdot m/^\circ C$
C_{skin}	heat exchange on the skin by convection, W
C_d	discharge coefficient through opening or hole
C_e	expansion coefficient through opening
C_p	specific heat, $J/kg \cdot K$
C_{p_wind}	wind-induced pressure coefficient
C_{res}	respiratory heat loss by convection, W
D_h	hydraulic diameter of the opening on building wall, m
D_{max}	maximal water loss for human bodies, Wh/m^2
E_{bi}	emissive power of a blackbody from i^{th} surface, W/m^2
E_{res}	respiratory heat loss by evaporation, W
E_{req}	required heat exchange by evaporation of sweat for thermal equilibrium, W
F_{ij}	view factor from surface i to surface j
Gr	Grashof number
g	gravity, m/s^2
H	height, m
H_{ref}	reference height in calculating wind speed profile from ground
H_{met}	height of the meteorological tower, m
h	gas sensible enthalpy, J/kg
h_{conv}	convection coefficient, $W/m^2 \cdot K$
\bar{h}_{conv}	average convection heat transfer coefficient, $W/m^2 \cdot K$
h_{rad}	radiative coefficient, $W/m^2 \cdot K$
I	current in each rod, A
J_i	radiosity from i^{th} surface, W/m^2
k	thermal conductivity, $W/m \cdot K$

k	turbulent kinetic energy, m^2/s^2
L	length of a component in the direction of heat flux, m
M	metabolic heat generation, W
M_w	molecular weight of the gas, kg/mol
m	fin parameter in Eq. (2.17), m^{-1}
\dot{m}	mass flow rate, kg/s
n	second fin parameter in Eq. (2.17), K/m^2
P	perimeter of cross-section of a fin-like component, m
p	pressure, Pa
p'	“reduced pressure”, equal to pressure minus hydrostatic pressure, Pa
p_{wind}	wind induced pressure, Pa
Q_{max}	maximal heat storage, Wh/m^2
q	heat transfer rate, W
\dot{q}_{jh}	volumetric Joule heating, W/m^3
q''	total heat flux, W/m^2
q''_{rad}	radiative heat flux, W/m^2
R	universal gas constant, $\text{J}/\text{K}\cdot\text{mol}$
R_{skin}	heat exchange on the skin by radiation, W
Re	Reynolds number
RSI	R-factor, $\text{m}^2\cdot\text{K}/\text{W}$
R_i	i th equivalent thermal resistance in the circuit ($i=1-14$) in Fig. 2.2b, K/W
r_j	j th equivalent thermal resistance in the sub-circuit ($j=1-6$) in Fig. 2.3b, K/W
r_{req}	evaporative efficiency at required sweat rate
S_h	heat source term in energy equation, W/m^3
S_{req}	required sweat rate, W
T	temperature, K
t	plate thickness, m
T_{dp}	dew point of air, $^{\circ}\text{C}$
T_{sky}	sky temperature, K
U_{met}	mean wind speed measured at the tip of the weather station tower

U_{ref}	mean wind speed at an external reference position, m/s
u_i, u_j	time averaged velocity components, m/s
W	mechanical power and normally taken 0,
x	Cartesian coordinate, m
y^+	dimensionless wall distance

Greek symbols

α, δ	atmospheric boundary layer parameters and determined based on the classification of terrain category
η	fin system efficiency
θ	temperature difference ($T - T_{\text{gas}}$), K
ρ	density, kg/m ³
ρ_e	electrical resistivity, $\Omega \cdot \text{m}$
μ	dynamic viscosity, Pa·s
ε	radiation emissivity
ε_i	i^{th} surface emissivity
δ_{ij}	Kronecker delta

Subscripts

b	base of a fin-like component, boundary condition
cond	conduction
conv	convection
cover1	anode cover on crust layer
cover2	anode cover on carbon anode
d	discharge
e	expansion
eff	effective
gas	gases in the cavity under hood
i	internal
jh	Joule heating

L	tip of a fin-like component, boundary condition
max	maximum
mec	mechanical ventilation
met	metology
nat	natural ventilation
o	exterior of building
op	operation
<i>op</i>	operating pressure
rad	radiation
ref	reference
req	required
superhood	superstructure and hoods in the pot
t	turbulence

ACKNOWLEDGEMENTS

This thesis represents not only a summary of the results that I have achieved during the four-year Ph.D. program, it is also an evidence of a pleasant collaboration between an academic institute and an industrial enterprise, namely Université Laval and Alcoa. Without a close coordination between these partners, it would have been impossible to achieve the outcomes reported in this thesis. Based on this point, I will take this chance to express the deepest appreciation to the people who have made efforts in this project.

Professor Louis Gosselin has been a supervisor, colleague and friend, since I was recruited into his laboratory in 2010. His guidance has made this an amazing and rewarding journey. His patience and persistence have made a feeling that he always back up on me whenever I was in difficulties. His amity and generosity have helped me to be easily adapted to the new environment. During the four years, he spent much time to teach me, guide me and unselfishly convey his intelligence to me. Moreover, he also supported me not only academically and financially but also emotionally. Within his persistent helps, I have been able to work in a pleasant environment.

I would like to thank my co-supervisor, Professor Mario Fafard in Department of Civil Engineering and Water Engineering, who is also the director of the Aluminium Research Centre – REGAL and the NSERC/Alcoa chairholder. His involvement and coordination provided me some useful ideas and opportunities to attend in several international conferences. They enriched my knowledge and experiences and may encourage me pursuing higher level in this field. Special acknowledgements are given to the Alcoa's staff, Donald P. Zeigler and Jayson Tessier. Donald, as my industrial advisor, helped me a lot by providing ideas and comments from industrial perspective during the course of my program. His guidance transferred me to think of questions in the perspective of industry and engineering. Jayson is a friendly person who devoted much time in my project. He always tried his best to help me performing experiments and inquiring the information I asked for.

I will also take this chance to appreciate all of my great colleagues in the laboratory. I would like to thank Guillaume Gauvin, who is responsible for my connection with the industrial partner. Abdellah Ousegui gave me a lot of academic comments in numerical simulations. All of my Ph.D. fellows, François Mathieu-Potvin,

François Grégoire, Benoît Allen and Maxime Tye-Gingras (research assistant), contribute their knowledge and experiences in my project. Thank you to other graduate and undergraduate colleagues in the laboratory and to my friends accompanying me during the four years.

This thesis has been funded by several organizations. The Chinese Scholarship Council (CSC) is the most appreciated sponsor. Without its four-year financial support, it is impossible to finish the thesis. The Fonds de recherche du Québec – Nature et technologie (FQRNT) provided a partially financial support in the thesis. A part of the research presented in this thesis was also financed by the intermediary of the Aluminium Research Centre – REGAL and the NSERC research chaire – Advanced Modelling of Electrolytic Cells and Energy Efficiency (MACE3). It is also grateful to Alcoa for its active involvement in the project.

I will finish the acknowledgements with a thank you to my family, which is also my fundamentally energy source for pursuing the Ph.D. degree. Thank you to my grandparents who taught me and cultivated me during my childhood. My parents, they are continuously supporting me in both finance and emotion to pursue high education level and are encouraging me to achieve more grand successes. My wife, Cen, came here to accompany me and made my life more comfortable. Thank you for your comprehension and contributions. Without the persistent supports from my family, I could not have been writing the thesis at this moment.

FOREWORD

Chapter 1 is an introduction to the background and current research progress of the subject studied in this work. Chapters 2 to 6 present scientific articles, each covering a sub-subject associated with the main topic. A comprehensive summary of the results is presented in Chapter 7, and also includes ideas for future work. The literature review of each article has been kept in each of their respective chapter. All the papers included in this thesis are listed below, and a brief statement of the role of each author in preparing each article follows, as requested by the FESP.

Chapter 2

Zhao, R., Gosselin, L., Fafard, M., Ziegler, D.P., Heat transfer in upper part of electrolytic cells: thermal circuit and sensitivity analysis, Applied Thermal Engineering, 54, 212-225 (2013).

Chapter 3

Zhao, R., Gosselin, L., Ousegui, A., Fafard, M., Ziegler D.P., Heat transfer and airflow analysis in upper part of electrolytic cells based on CFD, Numerical Heat Transfer, A: Application, 64(4), 317-338 (2013).

Chapter 4

Zhao, R., Gosselin, L., Fafard, M., Ziegler, D.P., Reduced ventilation of upper part of aluminum smelting pot: potential benefits, drawbacks, and design modifications, TMS-Light Metals, San Antonio, U.S., March 3-7 2013.

Chapter 5

Zhao, R., Gosselin, L., Fafard, M., Tessier, J., Airflow and thermal conditions in aluminum smelting potrooms under reduced pot ventilation conditions, Building Services Engineering Research and Technology, under review (2014).

Chapter 6

Zhao, R., Gosselin, L., Fafard, M., Tessier, J., Ziegler, D.P., Efficiency of pot tightness in reduced pot draft based on CFD simulations, International Journal of Heat and Fluid Flow, under review (2014).

For the paper in Chapter 2, my role was to propose the core idea of the paper and to develop the thermal circuit network for calculating the heat flux in the upper section of

an aluminum smelting cell. I also developed a new expression for calculating the thermal resistance of a fin-like component with both convection and radiation with the environment. I wrote most of the paper. The second author (my supervisor) helped me to develop the model by presenting ideas and some derivations. He also contributed in the improvement of the writing and pictures. The third and fourth authors revised the paper and provided critical comments and suggestions from the industrial perspective.

For the paper in Chapter 3, I was involved in the development of the CFD model and the analysis of simulated results. I also proposed some ideas for the discussion based on the simulated results and wrote 80% of the text of the paper. The second author provided most important ideas in the analysis of the results and helped to edit the whole paper structure and to improve the writing. The third author guided me in both the general knowledge of CFD simulation and the detailed simulation procedure involved in the paper. The fourth and fifth authors were involved in the review of the paper and providing critical comments to improve it.

For the paper in chapter 4, I developed a CFD model to simulate the heat transfer in the upper part of aluminum smelting cell. In order to maintain the heat balance, I proposed and simulated several scenarios and designs of pot structure to estimate their efficiency on the enhancement of top heat loss. I was also in charge of the paper writing. The second author revised the paper and added 20% of text. The other authors were actively involved in the discussion and writing.

For the paper in Chapter 5, my role was to propose the topic and develop the required numerical model. I wrote 80% of the text and analyse the simulated results. The second author fully participated in the discussion and provided many critical questions. He also helped to improve the writing and added some new stuff. The third author performed the experiments for the validation of the numerical model, and provided an industrial point of view on the topic.

For the paper in Chapter 6, I suggested the main innovations of the paper and performed all numerical simulations. I also analysed the main results and wrote most of the paper. The second author revised the paper and added some ideas in the sections of validation and discussion. He also wrote 10% of the text. The other authors revised the paper and provided critical comments and suggestions from the industrial perspective.

During my study in Université Laval, I also published other papers related to the aluminum industry. Due to the volume of the thesis, they were not included in this document, but they listed here:

Zhao, R., Nowicki, C., Gosselin, L., Duchesne, C., Energy and exergy inventory in aluminum smelter from a thermal integration point-of-view, manuscript in preparation.

Zhao, R., Gosselin, L., Fafard, M., Investigation of pot tightness and fugitive emissions based on CFD simulation, ICSOBA 2014, Zhengzhou, China, Oct. 12-14.

Zhao, R., Gosselin, L., Natural ventilation of a tall industrial building: investigation on the impact of modeling assumptions, eSim 2014, IBPSA-Canada's biennial conference, Ottawa, May 7-10.

CHAPTER 1 INTRODUCTION

1.1 Introduction

Modern primary aluminum production is based on Hall-Héroult process. A schematic of a modern aluminum smelting cell is presented in Fig. 3.1a. The anode block is made from carbon and suspended in the electrolytic bath by an anode assembly. A carbon cathode is installed at the bottom of the pot cradle. Electrical current of high amperage circulates between the anode and the cathode through the electrolytic bath where alumina is periodically fed and dissolved. Electrochemical reactions that take place in the bath yield to the accumulation of a liquid aluminum layer on the cathode. The aluminum is siphoned out periodically. The carbon anode is consumed as deoxidizer, and CO₂ is continuously generated in the bath. Due to the effect of Joule heating, approximately half of the electrical energy is converted into heat. In a compact and very simplified way, the overall process is represented in the following way: $2\text{Al}_2\text{O}_3 + 3\text{C} + \text{electricity} \rightarrow 4\text{Al} + 3\text{CO}_2$. A layer of crust (a mixture of alumina and frozen electrolyte) is formed above the bath and serves as a thermal insulator and gas scrubber.

Although the Hall-Héroult process is over a century old, the energy efficiency of modern cells is still relatively low, with roughly half of the electrical energy that leaves the cells in the form of waste heat (Grjotheim and Kvande 1986). Since primary production of aluminum is a process that requires extensive amounts of electricity (approximately 13-15 MWh/ton of aluminum produced), heat losses represent a large amount of energy. With an increasing demand in energy (especially in emerging countries) and a relatively slow development of alternative energy resources, the energy has becoming a global concern and energy saving is attracting increasing attention, not only in the aluminum industry but for the society in general. The primary aluminum production, as a traditional energy-intensive industry, should pay more attention on improving its energy efficiency. One promising solution lays in the utilization of large amount of waste heat dissipated from aluminum smelters.

The heat sources in an aluminum smelter can be summarized in three major processes. The anode baking process is required to convert the raw anode into green anode, in which combustion of released volatiles and natural gas is used to heat the carbon anode. The combusted gases are exhausted out of the baking furnace at approximately 150 °C which indicates a moderate heat content in the gases. The

aluminum casting process also dissipates heat. The liquid aluminum at 920°C is casted and eventually cooled to the ambient temperature. Compared with the two other processes, the aluminum electrolysis is the most energy-intensive process and approximately 50% of the electricity input is dissipated out of smelting pots. How to efficiently optimize the waste heat recovery from the pots should be addressed before an efficient usage of the heat be implemented. Moreover, the changes for the optimization will inevitably influence the pot working conditions in other aspects, such as the heat balance, pot tightness and so on. To predict and address these issues is also the prerequisite for an advanced waste heat collection from the pots.

1.2 Current progress

Good initiatives of waste heat recovery in aluminum industry require a comprehensive understanding of the production processes, especially for the aluminum electrolysis. This is because any strategy for waste heat recovery will inevitably influence current working conditions, positively or negatively. How to achieve a good trade-off between maximizing collection of waste heat and minimizing influences on the production is a crucial question. To address this question, researchers or engineers need a good knowledge of aluminum reduction cells. Many investigations have been aimed at gaining a better understanding of the electrolysis process and the heat transfer in reduction cells based on either analytical calculations or experimental measurements. In the following sub-sections, research progresses in aluminum reduction cells are introduced in different aspects that are strongly relevant to our initiative of waste heat recovery.

1.2.1 Mathematical models of the electrolytic cell

To better understand the heat and mass transfer in electrolytic cells, many simplified and convenient mathematical models of the electrolytic cell are established based on mass and energy balances. A dynamic model for the enthalpy balance of a specific aluminum electrolytic cell was built and the combined effect of all process kinetics can be observed over time (Taylor et al. 1996). Then the model was applied to analyse the generic energy imbalance in a modern industrial electrolytic cell and to guide a better control on the cell

performance. Another mathematical model of the electrolytic cell based on the heat balance was proposed in the PhD thesis of Biedler (Biedler 2003). This model was also used to predict the cell performance and guide the cell control. Yurkov and Mann (2005) proposed a simple dynamic real-time model for aluminum reduction cell control system. This model is simply solved and can provide sufficient adequacy to the real object. Jessen (2008) developed a comprehensive mathematical model of an electrolytic cell based on the previous models and this model can be used to predict the cell performance in various operating conditions and aid to maintain high productivity, energy efficiency and minimize the overall cost of operation. More recently, a new model considering the reactions in the cell space under hoods was developed in the literature (Gusberti et al. 2012) and the modeling of mass and energy balance is extend to the hooded cell space and provided a more comprehensive understanding of the electrolytic cell. These mathematical models are easily adjusted to a specific electrolytic cell and can provide relatively accurate predictions of the pot conditions.

Computational fluid dynamics (CFD) simulation has been employed to simulate the fluid flow and heat transfer in electrolytic cells in the last two decades. The electrolytic cell is discretized into small control volumes, and the governing equations that express the mass, momentum and energy balances can be solved in each volume via the finite volume method. Another set of equations that describes the electromagnetic field is solved and coupled with the flow movement in electrolytic cell to consider the interaction between the electromagnetic field and the electrolytic bath. The integrated simulation is known as the Magnetohydrodynamic (MHD) simulation of electrolytic cell. A 3D numerical model was developed by coupling the commercial codes ANSYS and CFX via in-house programs and customization subroutines (Severo et al. 2005). An electromagnetic model was built using Finite Element Method and the MHD flows of electrolytic cell were simulated in both steady-state and transient. The transient bath-metal interface was studied for cell stability. Doheim et al. (2007) considered the effects of gas bubbles and electromagnetic forces on the flow pattern and cell performance by using numerical simulations. A recent work reviewed the progress of the simulation methods on the flow and MHD instabilities in aluminum smelting cells in terms of their benefits, limitations and effectiveness (Zhang et al. 2010). Due to a huge volume of

relevant papers, only a few are mentioned here to indicate the importance of numerical simulations (CFD, MHD) in modeling aluminum reduction cells.

1.2.2 Top heat transfer in smelting cells

Although the abovementioned models involve the heat transfer from the top and sidewall of electrolytic cells, it is worth to summarize the literature that is specifically focused on the top or sidewall heat losses. Top heat loss refers to the heat transfer through a series of resistances from the electrolytic bath to the cavity under pot hoods. Heat is mostly generated in bath and transferred to the bottom of the crust by radiation and convection. Radiation heat transfer dominates in the process because of the extremely high temperature in the bath. A value of $100 \text{ W/m}^2\cdot\text{K}$ was employed to indicate the overall heat transfer coefficient for the process with the bath temperature of 960°C in an 180kA cell simulation (Taylor et al. 1996). Taylor (2007) also proposed a thermal resistance model to describe the heat loss through the anode cover and anode assembly. The result indicated that the thermal resistance of the anode cover plays an important role in transferring the heat from the bath to the air in pot cavity. A stable crust layer with sufficient strength is necessary to maintain the integrity of the anode cover, and the cover with a proper thickness can prevent the anode from burning with the air. Tessier et al. (2008) found that the mixing and segregation of anode cover materials during cell operation can significantly change the anode cover composition, which leads to variations in the cover density and thermal resistance. The influence of particles size of anode cover materials on thermal conductivity was also reported in literature (Rye et al. 1995). The temperature dependence of the thermal conductivity of anode cover was investigated in cases with different particle size distributions in the work of (Shen 2006). More recently, Shen et al. (2008) performed measurements on the heat flux through anode cover in real plants. In the case of a loose alumina cover, the surface temperatures on anode cover varied from 160°C - 300°C and the heat flux is correlated with the local cover temperature and is increased from 1500 W/m^2 to 4000 W/m^2 . The surface temperatures of the crushed bath cover were in the range between 170°C - 260°C and the heat flux varied from 1500 W/m^2 - 3000 W/m^2 . The difference, the authors believed, was attributed to the different

material thermal conductivities in the two cases. The results indicated that the surface temperature and heat flux of the loose alumina cover are lower but have a stronger correlation between them than those of the loose crushed bath cover. Moreover, a correlation of the heat flux versus the cover thickness was also proposed in this work. A general tendency was found that the heat flux through anode cover is increased as the cover surface temperature increases (Eggen et al. 1992). The impact of moisture in alumina grains was studied in (Llavona 1988). The influence of the open holes in anode cover on the top heat loss was investigated in real plans in (Nagem et al. 2006; Gadd 2003). Cell fluoride emissions were increased with an increase of the collapsed anode cover, as reported in the literature (Nagem et al. 2005; Tarcy 2003; Dando and Tang 2006). It can be concluded that the thermal properties of anode cover has received much attention, and the variations in anode cover have a strong influence on the top heat losses.

Heat transfer through anode assembly was also investigated based on a simple 2D thermal resistance model in literature (Taylor et al. 2004). Relationship between anode cover thickness and the temperature of anode assembly is revealed by using this model. The results have illustrated that convective heat transfer dominates in normal condition while radiation should be considered in low draft condition because of extremely high surface temperature on anode assembly.

Heat loss in the pot cavity under hoods was studied in several papers. Experiments were performed to measure the exhaust gas temperature and the heat loss under different pot draft condition. For example, under normal condition, the heat loss from effluents can take up to 76% of the top heat loss in a 160 kA cell (Shen et al. 2008). In literature (Gadd 2003), a correlation of the exhaust gas temperature and the gas heat loss versus the draft condition was presented, and linear relation was found for both parameters but with opposite tendency. Nagem et al. (2006) used the exhaust gas temperature as an indicator to monitor the variation of the cell fluoride emissions in different operating conditions. Both of the two above papers also reported the variation of gas temperature in different hood openings and during anode changing. A comprehensive investigation on the top heat loss was found in most recent literature (Abbas et al. 2009), (Abbas 2010). The influence of various factors on the gas temperature and heat loss was

studied based on numerical simulations and some proposed modifications in pot structure aimed at enhancing the thermal quality of the exhaust heat.

More recently, waste heat recovery from the pot exhaust gas has received much attention. Sørhuus and Wedde (2009) developed a heat exchanger with a good trade-off between heat recovery and cost efficient cooling of pot gas. Promisingly stable heat exchange and minimum fouling deposits over longer test periods have been observed and encouraged manufacturer to continuously develop a commercial product. In 2010, they published their new tested results of a real heat exchanger in smelting cell plant (Sorhuus et al. 2010). A stable working of the heat exchanger provides heat directly to local heating system. The installation of this facility can not only further reduce the power consumption and total HF emission, but significant reduce the size of gas treatment center. Another work has reported to perform experiment to measure the potential heat recovery from pots, and a detailed analysis of fouling in heat exchanger was present (Fleer et al. 2010). Fanisalek et al. (2011) further studied a specific implementation of combining the waste heat recovery from pot exhaust gas with the water vaporization in desalination industry. Lorentsen et al. (2009) reported that Hydro in Norway has developed a new gas suction technology, which has a more efficient CO₂ capture from electrolytic cells, as well as reducing the total suction flow volume and fan power consumption.

1.2.3 Sidewalls heat transfer in smelting cells

Heat losses through sidewalls of smelting pots have received a lot of attention, in particular because it is very critical to maintain a frozen bath layer between the sidewalls and the liquid bath and metal, which is used to prevent the cell lining suffering from the aggressive environment in the bath (Grjotheim and Kvande 1986; Taylor 1984). A mathematic model was proposed to calculate a proper thickness of the frozen bath layer in smelting cells by solving a set of heat transfer equations (Haupin 1971). More recently, full 3D thermo-electric numerical models in high amperage cells were presented in the literature (Dupuis et al. 2004; Dupuis 2010). However, the values of heat transfer coefficients at the ledge surface are still not well determined. Severo and Gusberti (2009) have performed systematic and detailed numerical simulations to study the sensitivity of

the heat transfer coefficients between the ledge and the liquids (bath and metal) on different working conditions. Another numerical model, considering phase change in the cavity and bath regions, was presented in literature (Marois et al. 2009). A relatively simple mathematical model was presented to predict the variation of ledge thickness in the bath for different operating conditions in the literature (Kiss and Dassylva-Raymond 2008). A very high level of turbulence occurs in this region, which create a high heat transfer coefficient at the interface of bath and metal (Fraser et al. 1990). For example, $1000 \text{ W/m}^2\cdot\text{K}$ was adopted by Taylor to describe the heat transfer at the interface in simulation work (Taylor et al. 1996). In conclusion, the mechanism of heat transfer at the interface of ledge and liquid (bath and metal) is still an open question (Solheim 2011). The heat transfer coefficient in the bath can vary significantly according to different operating conditions.

The overall heat transfer coefficient from the sidewalls to ambient was measured in the range of $18\text{-}20 \text{ W/m}^2\cdot\text{K}$ for a 165 kA aluminum reduction cell (Eick and Vogelsang 1999). In reference (Haugland et al. 2003), theoretical calculations were performed to calculate the free convection and radiation heat transfer coefficients separately. The results indicate that the convection coefficient is insensitive to the sidewall surface temperature, and on the other hand, the radiation coefficient is increased significantly with the increasing surface temperature. The overall coefficient is varied from $15 \text{ W/m}^2\cdot\text{K}$ to $30 \text{ W/m}^2\cdot\text{K}$ when the surface temperature is increased from 150°C to 350°C with the ambient temperature of 20°C . Recently, researchers and engineers studied to achieve a better cooling on the sidewall by installing a series of heat exchanger modules (Namboothiri et al. 2009). The goal of this implementation is to add a more active sidewall cooling control which can remove more waste heat from the sidewall when a load creeping occurs in the pot. This application, called power modulation, is particularly beneficial for industries because it allows the pot to increase the productivity during night when the electricity price is usually lowest. However, there is still no systematic studies on the sidewall heat loss in the perspective of waste heat recovery.

1.2.4 Fluoride emissions from electrolytic cells

One of the environmental issues in the aluminum industry is the emissions of hazardous gases (mainly consisting of gaseous and particulate fluorides) produced in the electrolysis process as by-products. In modern electrolytic cells, a large volume of air is suctioned into the hooded pot space and dilutes the process gases. A collecting duct is installed above the pot superstructure and conducts the mixture of air and process gases into a gas treatment center. However, 100% hooding efficiency is barely guaranteed in real pot operation because pot hoods are periodically removed for operations, such as anode change, tapping of aluminum and so on. As a result, the vacuum in the hooded pot space is diminished and pot gases can escape from the upper openings on pot shell. Many efforts were devoted to enhancing pot tightness in such situations.

Fugitive emissions may occur in the pot superstructure all the time, even though the main source of emission comes from the gas leakage during pot operations. Since the control of hazardous gases is of great importance for the employees' health in the potroom and for environmental reasons, an intensive research has been done to study the fugitive emissions of pots. The study of fugitive emissions was mainly based on experimental measurements and qualitative analysis. The early efforts were mainly devoted to monitoring the HF concentration in the pot off gas under different pot conditions and during various pot operations (Tarcy 2003; Slaugenhaupt et al. 2003; Dando and Tang 2005; Dando and Tang 2006). More recently, HF concentration was measured in the pot cavity to determine where HF is released from and to develop correlations between the various sources of water and the resulting HF emissions (Osen et al. 2011; Sommerseth et al. 2011). Although literature is abundant in this field, fewer works are available on the gas leakage into the potroom from the pot gaps. Dando and Tang (2005; 2006) reported the transient measurement of the HF concentration profile in the area just above pot hoods in different pot conditions. It was found that the thermal buoyancy from crust holes and the leakage of the pneumatic system of the alumina feeding system are the two main reasons explaining the HF release from pots when the hoods are into place. In addition to experiments, models were developed to calculate the pot draft and to investigate pot hooding efficiency (Dernedde 1990; Karlsen et al. 1998). These models consider the flow infiltration through pot gaps due to natural and

mechanical ventilations in the pot, but they are too simple to provide accurate results. The literature review indicates that there are few studies of fugitive emissions via numerical simulations, e.g., CFD simulations.

1.2.5 Heat and mass transport in potroom

In aluminum smelting plants, hundreds of electrolytic cells are lined up and hosted by a potroom with an extreme long length. Natural ventilation is normally employed in the potroom to remove the waste heat dissipated from cells. A proper design of the potroom is crucial to achieve an adequate cooling of the room space. Meanwhile, the potroom ventilation plays a role in diluting the hazardous gases in potroom, because current cells are not 100% tightness during the operation and an amount of fluoride materials is emitted into the potroom. To control the fluoride under certain regulatory limits is also an important parameter of potroom design. A relatively early study on the potroom ventilation was made by Dupuis (2001) where a 3D potroom model is developed in the CFX-4 commercial code and the turbulence can be properly simulated. A computational fluid dynamics (CFD) model was developed to aid the design of potrooms in the Fjarðaál smelter (Berkoe et al. 2005). The flow in both the potrooms and the atmosphere surrounding the smelter is simulated and the design is verified based on the temperature and HF concentration. A more delicate CFD model was proposed to study the potroom ventilation by coupling with an innovative approach for the calculation of cell emission rates (Vershenya et al. 2011). The potroom design is also verified based on the air temperature and HF concentration in potroom. More recently, a new work consisting of building several CFD models of varying complexities is introduced to study the potroom ventilation in different working conditions (Menet et al. 2014). Another novel model, based on purely analytic calculation, provided a convenient tool to calculate the ventilation rate in potroom (Dernedde 2004).

1.3 **Problematic and objectives**

The literature review illustrated abundant research resources in the field of aluminum reduction cells. However, few papers were found to focus on the waste heat recovery

from cells. Although many analytical models were developed to describe the mass and heat transfer in electrolytic cells, there were few models that can perform a systematic analysis on the heat transfer from the standpoint of waste heat recovery. Since the working condition of electrolytic cells is very sensitive to the heat transfer from pot sidewalls, the focus of the present work will be on the top of the cell. It requires a simple but comprehensive method to model the heat transfer by conduction, convection and radiation. Meanwhile the model is capable of performing sensitivity analysis on some parameters of interest (e.g. the temperature and thermal content of pot exhaust gas).

By accounting for the different paths followed by the heat flux in the top of electrolytic cells, the pot exhaust gas is the most efficient access to the dissipated waste heat. Provided a reduction in the ventilated rate of the exhaust gas, thermal quality of the heat in the exhaust gas can be further enhanced. Recuperating heat from pots is not a new idea, as explained in the literature section. However, most of the findings are focused on collecting the flue heat in current working conditions, where the gas temperature is relatively low ($\sim 130^{\circ}\text{C}$ in summer and $\sim 90^{\circ}\text{C}$ in winter) for advanced applications, such as power generation and heating a distant location. A few publications refereed to the reduction of pot draft condition in order to get higher flue temperature and concentration of CO_2 . However, a systematic analysis based on the practical viewpoint was not found in literature.

In fact, there are at least three engineering problems that need to be addressed before a successful application of pot draft reduction. First, current heat balance should be maintained in the pot. A reduction of pot draft will sacrifice the capability of carrying away the top waste heat by the exhaust gas. More heat will be either accumulated in the bath or dissipated from the pot sidewalls. Neither of the ways is desirable for controlling the cell performance. Modifications should be done in the pot geometry or material properties to facilitate a better heat dissipation from the top of cell. Meanwhile it is expected that an additional portion of the heat will escape into the potroom, where the influence on temperature and flow pattern should be verified in a reduced pot draft condition. The last and most important aspect is how to deal with the fugitive emissions (i.e. hazardous materials, mostly consisting of gaseous and particulate fluoride, can leave from the hooded pot cavity into the potroom) under a reduced pot draft condition. A

reduction in gas suction inevitably creates a low vacuum in the hooded pot cavity, which can bring in a risk of emitting more gases into potroom.

Since the study of fugitive emissions is of great importance in the pot design, a design tool is required when doing any modifications. Experiments are a good choice but they are very expensive and time-consuming. In a conceptual design stage, it is impossible to build a prototype for real experiments. Moreover, the experiment can only provide the information on limited measured points. Numerical simulation has become a popular tool for the initial design in almost all industrial fields. A CFD model can provide a detailed flow tracking in and out of the pot and it is also easy to change the model geometry to represent different pot designs. Some of the publications presented the CFD simulation of hazardous gas transport in potroom (e.g. HF). Others mentioned in-house models to predict fugitive emissions. The CFD study of pot fugitive emissions in the coupling area (i.e. the modeling domain focused on the areas both in the hooded pot cavity and its surrounding potroom environment) is scarce and it requires a suitable model in this field.

Overall, the objectives of this thesis can be summarized as follows:

- To develop a simple mathematical model for analyzing the heat recovery potential from the exhaust gases of electrolytic cells
- To provide a systematical analysis of the feasibility of pot draft reduction, including the heat management in the cell and the potroom, the fluid flow in pot and potroom, and pot tightness for emission control
- To develop a CFD model that can simulate the fugitive emissions from the hooded pot cavity to the potroom
- To achieve a better understanding of the heat transfer and air flow patterns in pot and potroom.

1.4 Overview

In this section, a brief introduction is given for each of the following chapters. The introductions from chapter 3 to chapter 8 demonstrate the innovations or contributions of each article in this field.

In Chapter 2, an advanced thermal circuit model is developed to calculate the heat transfer in the top section of an aluminum reduction cell. One sub-network considers conduction and convection and the other one, radiation. They are coupled by substituting the calculated irradiation into the conduction equation as a source term. All major parts in the top section are considered and the parameters can easily be changed to perform a sensitivity analysis. A systematic analysis of the pot flue temperature and its heat content with respect to some pot parameters is performed and it is proved that the pot draft condition is the most influencing factor on the pot flue temperature. This conclusion led us to think about how to reduce the pot draft condition in order to increase the thermal quality of waste heat in the pot flue.

In Chapter 3, a CFD model is developed to study the heat transfer in the top section of an aluminum reduction cell. The simulated results are compared with those calculated from the thermal circuit model, and good agreement is obtained between them. By using the CFD model, the heat transfer coefficients on the main surfaces under the hooded pot cavity are studied and the results provide detailed information of heat transfer in the pot cavity. The relative importance of natural convection and forced convection in the pot cavity is revealed by analysis, for different draft rates. A good understanding of the heat transfer mechanisms in the top part of the cell is achieved.

In Chapter 4, the CFD model of top section of the cell is further developed to represent different modified pot designs. The purpose of the modifications is to maintain current top heat loss under a reduced pot draft condition, because the carried heat in the pot exhaust gas is also reduced with the draft reduction. A reduced pot draft can significantly increase the pot flue temperature, and at the same, save large amount of electricity for the ventilation system. It is found that the heat loss by radiation is also as important as that by convection in the hooded pot cavity, because the exposed yoke and stubs possess high surface temperatures and can emit a large amount of heat to the hoods and superstructure. The efficiencies of different scenarios are estimated and it is illustrated that the top heat loss can be enhanced to current level in 50% reduced pot draft.

In Chapter 5, a 3D potroom sliced model is presented to study the air flow and heat transfer patterns in potroom. The model is used to assess the thermal comfort in the potroom under different pot draft conditions and outdoor conditions (wind and ambient

temperature). The influences of outdoor wind and pot-induced buoyancy force on the potroom ventilation are illustrated in the simulations. The results have indicated that reducing pot draft condition increases the heat stress very little in the potroom.

In Chapter 6, the pot tightness is investigated in a smelting cell with reduced draft, down to half of the current level. Several CFD models with different simulation length scales are created in order to iteratively define proper boundary conditions around the leaking area. A systematic analysis of the pot tightness is presented by considering various factors, e.g., pot draft, hood placement. The results have shown that current pot structure, even within ideal operating conditions, fails to maintain 100% hooding efficiency under a 50% reduced pot draft. Two design modifications are proposed and verified. An efficient sealing is observed when covering the lower half of the gaps between hoods.

**CHAPTER 2 HEAT TRANSFER IN UPPER PART OF ELECTROLYTIC
CELLS: THERMAL CIRCUIT AND SENSITIVITY ANALYSIS**

Abstract

A model based on a thermal circuit representation was developed to study the heat transfer mechanisms in the top section of an aluminum smelting pot. In view of waste heat recovery applications, the sensitivity of the off-gas temperature and of the heat content in the gas with respect to several parameters was investigated. It was found that the draft condition was the most influential parameter. Additionally, the convection coefficients on the anode cover, and on the yoke and stubs proved to have a stronger influence on exhaust gas temperature, compared with the heat transfer coefficients on the hoods and rod. The results indicate that it is conceptually possible to increase both the gas temperature and the heat content, while maintaining at the same time the current operating conditions of the cell. Variations of the potroom temperature, hood insulation and anode height were also considered and affected significantly the gas temperature.

Résumé

Un modèle de type circuit thermique a été développé pour étudier les mécanismes de transfert thermique par le dessus de la cuve d'électrolyse. En vue de récupérer les rejets de chaleur, la sensibilité de la température des gaz d'échappement et de la quantité de chaleur qu'ils contiennent a été étudiée par rapport à plusieurs paramètres. Il a été trouvé que le taux de ventilation des cuves était le paramètre le plus influent. De plus, les coefficients de convection sur la couverture anodique, sur la barre transversale (*yoke*), sur les rondins ont aussi une grande influence sur la température des gaz, comparés aux coefficients de convection sur les capots et les tiges anodiques. Les résultats indiquent qu'il est conceptuellement possible d'augmenter à la fois la température et le contenu thermique, tout en maintenant en même temps les conditions d'opérations actuelles de la cuve. Les impacts de la température de la salle des cuves, de l'isolation des capots et de la dimension des anodes ont aussi été considérés et affectent significativement la température des gaz.

2.1 Introduction

Today's dominant technology of aluminum production is based on the Hall-Héroult process. Electrical current circulates between a carbon anode and a cathode through an electrolytic bath in which alumina is dissolved. Thermo-chemical reactions that take place in the pot yield to the accumulation of an aluminum layer in the bottom of the cell which can be taken out of the cell periodically. The carbon anode is consumed during the process and consequently, CO₂ is released. In a compact and very simplistic way, one can write the overall process as: $2\text{Al}_2\text{O}_3 + 3\text{C} + \text{electricity} \rightarrow 4\text{Al} + 3\text{CO}_2$.

Although the Hall-Héroult process was patented in 1886, the energy efficiency of modern pots is still relatively low, with roughly half of the input energy leaving the pots in the form of waste heat. Since primary production of aluminum is a process that requires extensive amounts of electricity (approximately 13-15 MWh/ton of aluminum produced), heat losses represent large amounts of energy. Over the years, intensive research thus aimed at gaining a better understanding of how heat is lost through the different components of the pots (Grjotheim and Kvande 1986; Taylor et al. 1996; Rye et al. 1995).

Heat losses through sidewalls of smelting pots have received a lot of attention, in particular because they influence directly the thickness of the frozen electrolyte layer that forms on the internal surface of the refractory bricks and which is required to preserve the pot integrity (Grjotheim and Kvande 1986). Recently, sidewall heat exchangers have also been developed in view of controlling pot heat balance under power modulation and eventually using the recovered heat loss from sidewalls (Namboothiri et al. 2009).

Heat loss from the top of smelting pots (including the energy carried away by the effluents) is also important since it account for more than half of the total waste heat of smelting cells. Heat is transferred from the bath through the anodes and the anode cover (porous layer above the bath and anodes), and finally evacuated into the gas under hoods (Taylor et al. 2004). In the analysis of top heat losses, most attention has been devoted to the influence of the anode cover. Taylor (2007) proposed a simplified thermal circuit model describing the heat losses through the crust and anode cover. The result indicated that the thermal resistance of the anode cover plays an important role in transferring the heat from the bath to the air under hoods. Tessier et al. (2008) found that the mixing and

segregation of anode cover materials during cell operation can significantly change the uniformity of the anode cover composition, which leads to variations in the cover density and thermal resistance. This phenomenon has also been observed in (Hatem et al. 1988). The influence of particle size of anode cover materials on thermal conductivity was also reported in Rye's research (Rye et al. 1995). More recently, Shen et al. (2008) performed measurements of the heat flux through different anode covers. The results indicated that the surface temperature and heat flux of the loose alumina cover are lower than those of the loose crushed bath cover. Moreover, a correlation of the heat flux versus the cover thickness was proposed in that work.

The studies regarding top heat loss associated with the effluents are scarcer in open literature. Gadd et al. (2000) had reported the measurements of the duct gas temperature and gas flow heat content in various process operations. Nagem et al. (2006) further studied the influence of the collapsed holes in the crust on the temperature of the effluent. Additionally, Taylor et al. (2004) created a simple 2D model to study the heat loss from the anode assembly, and demonstrated that convective heat transfer dominates radiative heat transfer under normal ventilation condition. Measurements have shown that the heat exhausted by the effluents represents 76% of the top heat loss (Shen et al. 2008). A simplified analytical model was presented by Karlsen et al. (1998) to estimate the cell tightness and gas collection efficiency in the cavity under hoods. One of the most comprehensive studies of top heat losses was presented by Abbas (2010). Based on CFD simulations and thermal circuits, different parameters of the pot were studied to find their influence on the top heat loss, and some geometrical modifications were proposed in view of waste heat recovery. In literature (Zhao et al. 2013), a detailed CFD analysis of the upper domain of the pot is proposed, in order to determine heat transfer coefficients on the main components under different ventilation rates.

As can be seen from the above review of open literature on the topic of heat loss from pot upper structure, the main focus so far has been on studying the physical and thermal properties of one specific component of the pot at a time. In the present paper, we propose a thermal circuit model describing the overall heat losses through the upper structure of a pot, from the free surface of bath to the ambient in potroom. Thermal circuits, thanks to their easiness to use and speed to solve, are thoroughly used to study

heat transfer management and control in a wide variety of complex systems such as electronic devices (Luo et al. 2008), buildings (Zueco and Campo 2006) (Dussault et al. 2012), magnets (Kolondzovski et al. 2009), heat drains (Chataigner et al. 2009), etc., in which case they are often coupled to more advanced computational tools such as CFD. The main objective of this work is to provide more insights on the thermal interactions in the pots and to provide simple and convenient tools to facilitate the thermal management of the superstructure, in particular in view of future waste heat recovery applications or design modifications. For the sake of illustration, the study was based on actual pot design and operation at the Alcoa Deschambault smelter (ADQ), in Canada.

2.2 Description of the system

A schematic representation of the system considered in the present study is shown in Fig. 2.1. The system consists of the upper part of a typical electrolytic cell used for aluminum production. Anodes are partly immersed in an electrolytic bath which is maintained at an approximate temperature of 955°C. A layer of crushed bath and fines is deposited above the bath surface and on the anodes. This isolating layer is called anode cover. Each anode assembly is composed of steel stubs and a yoke connected to an aluminum rod. The purpose of the anode assemblies is to hold the anodes in place and to conduct the electrical current into the pot. Hoods are installed above the cell in order to diminish heat losses to the ambient and to prevent the release of effluents into the potroom environment.

As the reduction takes place, the anode is consumed and CO₂ is released into the space under the hoods, mainly through the feedholes (locations where alumina is added to the bath). A duct network collects the effluents of the pots by creating a negative pressure inside of the cavity. Thanks to small gaps on the hoods, air flow goes inside the cavity and dilutes the CO₂ and other hazardous gases. In other words, the cavity is ventilated with the ambient air of the potroom. Current ventilation rates are quite large, e.g., a few Nm³/s of air per cell (the N stands for normal or standard conditions, i.e. at 1 atm and 300

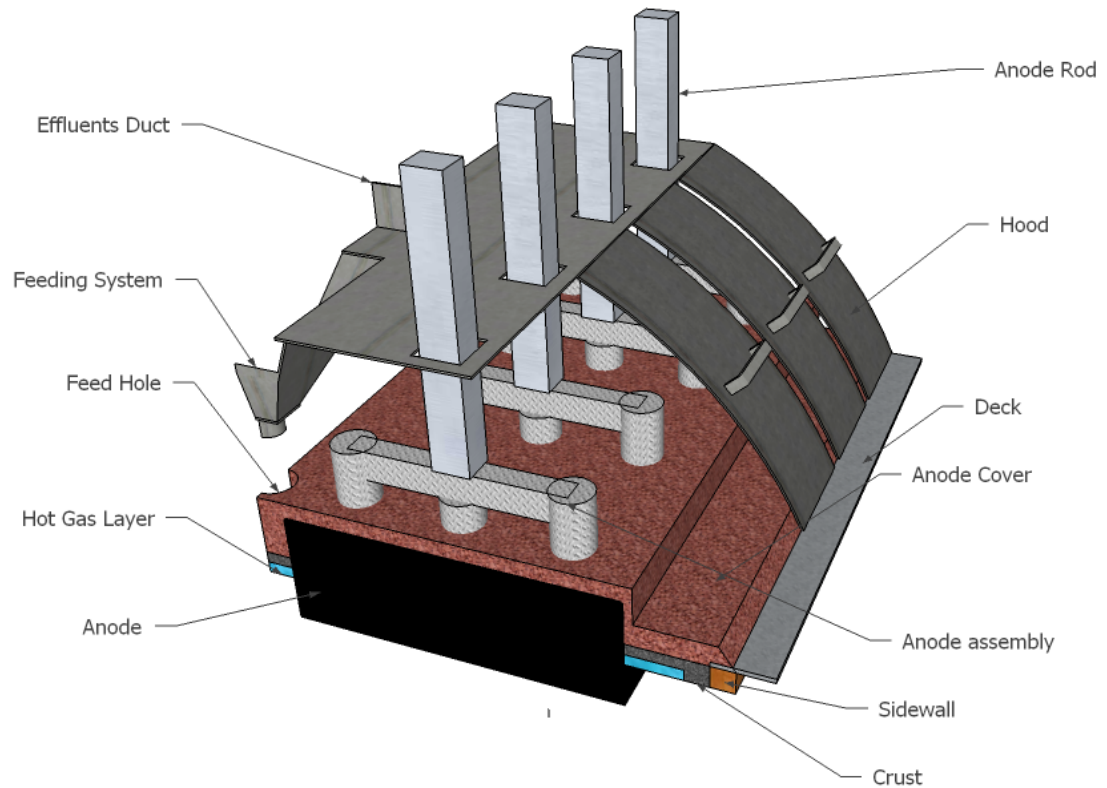


Figure 2.1 Representation of the upper part of a typical electrolytic cell with its main components.

K). Said differently, typical cell ventilation dilutes CO_2 down to concentration around 1%. Roughly 15-20% of the electrical energy sent to the pots is eventually released as heat via the effluents in the collecting duct network. Just to provide an order of magnitude of what that represents, for a plant like Alcoa's Deschambault (ADQ) smelter in Canada (~260,000 tons of aluminum/year), the energy lost in the cell effluents can represent as much as 650 GWh/year of thermal energy.

Our study aims at developing a better understanding of heat transfer mechanisms involved in Fig. 2.1, and to study different possible scenarios in particular in the perspective of waste heat recovery from effluents.

2.3 Thermal circuit representation

In order to model in a convenient way the system presented above (Fig. 2.1), a thermal circuit was built to account for the main heat transfer mechanisms involved in the system.

The circuit is shown in Fig. 2.2. Several temperature nodes are chosen to connect resistances. Their positions are indicated in Fig. 2.2a. Given the driving temperature difference between the bath and the potroom air (see Fig. 2.2b), the network allows determining how and where heat is lost via the upper part of the cell. This model consists of two coupled sub-networks which are shown separately in Fig. 2.2 to facilitate the reading: Fig. 2.2b represents the conduction and convection sub-network, and Fig. 2.2c, the radiation sub-network.

The construction of the network model relies on the following assumptions: (i) The system operates at steady-state (no thermal mass); (ii) The heat flow is 1D in the parts modeled. According to (Taylor et al. 1996), the isotherms are parallel in most regions of the cell lining and approximately 90% of the bath heat loss is conducted in 1D, e.g., through the crust, sidewalls, anode and cell bottom; (iii) Most material properties are assumed to be temperature independent (except for the electrical resistivity). Variations of electrical resistivity with temperature and the internal Joule heating were accounted for in fin-like elements (see Section 2.4); (iv) Due to symmetry, only one anode and its surrounding domain is represented in the model. In reality, small spatial variations of conditions in the pot exist (for example, the exhaust duct system or the anode replacement procedure could introduce a non-uniform pressure distribution in the pot); (v) The heat loss due to the collapsed holes in anode cover is not considered in this model.

Each node of Fig. 2.2b represents a local average temperature on a specific surface area of the system, and nodes are connected with thermal resistances representing the proper heat transfer mechanism between these nodes. In practice, the bath temperature is maintained around 955°C by the pot control system. The potroom air temperature fluctuates seasonally with exterior conditions, and is normally in the range from -10 to 35°C for the Alcoa's Deschambault smelter in Canada (ADQ). Temperature as high as 50°C were also reported in literature (Abbas et al. 2009).

Note that similar networks were proposed in open literature (Abbas 2010). Among the improvements and differences of the present model are: (i) No temperature inputs other than the bath and potroom air are required; (ii) Joule heating in anode and anode assembly is included; (iii) The complete 1D temperature distribution (from the bath to the

top) can be obtained from the model (see Section 2.4); (iv) New correlations have been developed and used for the heat transfer coefficient on different surfaces (Zhao et al. 2013), see Table 2.1.

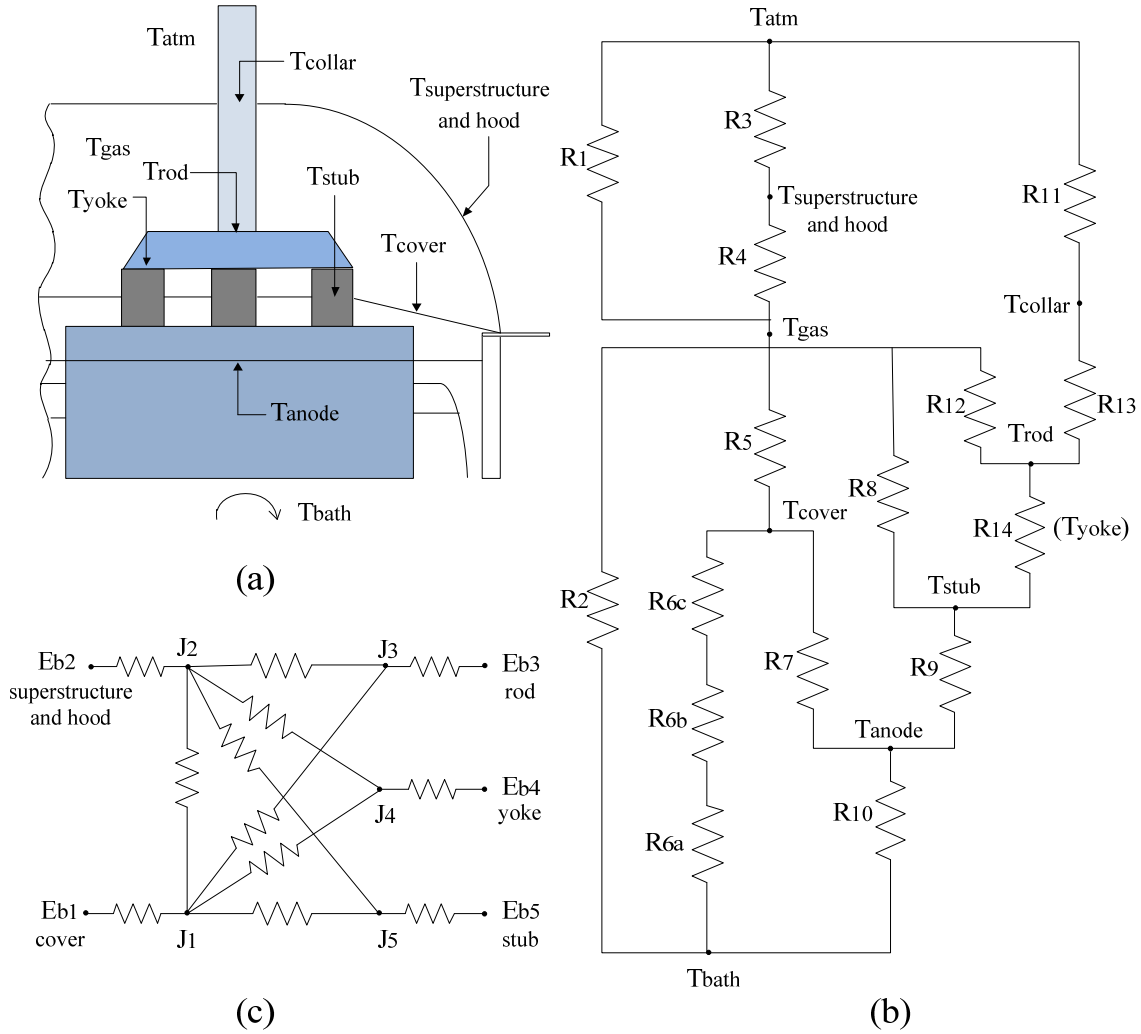


Figure 2.2 Thermal circuit representation of Fig. 2.1, with: (b) convection and conduction sub-network, and (c) radiation sub-network.

Table 2.1 Correlations for average convection coefficients on four surfaces of the cavity, as a function of volumetric flow rate Q for one pot [Nm^3/s] (Zhao et al. 2013).

Surface	Correlation
Anode cover	$\bar{h}_c = 5.32 + 1.79Q$
Hoods, superstructure	$\bar{h}_h = 3.87 + 2.28Q$
Rod	$\bar{h}_r = 2.33 + 1.89Q$
Yoke and stubs	$\bar{h}_{ys} = 6.28 + 1.73Q$

2.3.1 Conduction and convection sub-network

Heat can escape from bath to potroom through three different pathways in the conduction and convection sub-network. First, the hot gases (mainly CO_2) released from the bath to the space under the hoods carry thermal energy, and the corresponding thermal resistance between T_{bath} and T_{gas} (T_{gas} is the temperature of gases in the cavity under the hood) is

$$R_2 = \frac{1}{\dot{m}_{\text{CO}_2} c_{p,\text{CO}_2}} \quad (2.1)$$

This “ventilation” resistance comes from the fact that performing an energy balance in the space under the hood, the difference between the energy provided to the control volume by the CO_2 released at T_{bath} and that removed from the control volume by the CO_2 leaving the cavity at temperature T_{gas} is $\dot{m}_{\text{CO}_2} c_{p,\text{CO}_2} (T_{\text{bath}} - T_{\text{gas}})$.

In the second pathway, heat is transmitted from the bath through the crust and anode cover, and is eventually dissipated in the gas flow under the hoods. An overall heat transfer coefficient of $100 \text{ W/m}^2\cdot\text{K}$ was considered between the bath and the surface of the crust facing the bath (Taylor et al. 1996) (resistance R_{6a}). As mentioned above, heat conduction in the anode, crust, cover and stubs immersed in cover is considered as a one-dimensional problem. The conduction thermal resistance of the components without Joule heating is thus of the form

$$R_{\text{cond}} = \frac{L}{kA} \quad (2.2)$$

where L is the thickness of a component, k , its thermal conductivity, and A , its cross-sectional surface area. Eq. (2.2) was used to calculate resistances R_{6b} (crust), R_{6c} (anode cover), and R_7 (cover above anode).

A particular attention should be paid to the thermal resistance of the anode, which can generate a large amount of heat due to Joule heating. In this work, we assumed an average electrical resistivity for the anode to calculate the heat generation. This choice is justified because although the electrical resistivity of the carbon (the major material of anode) possesses a linear temperature-dependence (data provided by ADQ), it is only reduced by less than 20% in the studied temperature range while the resistivity of steel and aluminum can vary much more significantly. Also, our focus is on the structure above the anode cover, and thus the detailed information below the cover is not required. Therefore, the effect of Joule heating in the anode can be treated as a constant heat generation term in a one-dimensional conduction equation:

$$k \frac{d^2 T}{dx^2} + \dot{q}_{jh} = 0 \quad (2.3)$$

where the volumetric Joule heating term is $\dot{q}_{jh} = I^2 R / V = I^2 \rho / A^2$. The temperature distribution in the anode is thus

$$T(x) = T_{bath} + (T_{anode} - T_{bath}) \frac{x}{H} + \frac{\dot{q}_{jh} x}{2k} (H - x) \quad (2.4)$$

where $H = 0.3$ m is the anode height. We can easily calculate the heat flux at the top of the anode ($x = H$) by taking the derivative of Eq. (2.4) with respect to x , and evaluating the result at $x = H$:

$$\frac{q_{anode}}{A_{anode}} = -k \left. \frac{dT}{dx} \right|_{x=H} = \frac{k(T_{bath} - T_{anode})}{H} + \frac{\dot{q}_{jh} H}{2} \quad (2.5)$$

Note that the value of H used here is slightly smaller than the actual height of the anode. This value was chosen because the real contact area between the anode and the bath includes not only the bottom surface but also the portion of side surfaces of the anode immersed in the bath. Heat will thus be transferred from the bath to the anode by a surface larger than that of the bottom of the anode, i.e. the thermal resistance of the anode block is reduced due to 3D effects. Since a 1D heat transfer model is used here in the

anode block, this reduction of anode thermal resistance was accounted for by using an H value smaller than that of the real block. The equivalent thermal resistance is thus

$$R_{10} = \frac{1}{\frac{k_{\text{anode}} A_{\text{anode}}}{H} + \frac{I^2 \rho_{\text{anode}} H}{2A_{\text{anode}} (T_{\text{bath}} - T_{\text{anode}})}} \quad (2.6)$$

Alternatively, it would have been possible to include the heat generation as local heat input at the corresponding temperature nodes of the circuit, but the formulation of Eq. (2.6) was retained here.

Included in the thermal circuit of Fig. 2.2b is also the part of the stubs that is embedded in the anode cover rather than exposed to air. This is represented by R_9 , which is determined by ignoring the heat exchange between the stubs and the cover, considering the high thermal conductivity of steel compared to that of the anode cover material. Therefore, only the conduction and internal heat generation are considered in stubs. However, differently than for the anode, the temperature dependence of the electrical resistivity of steel was accounted for here. A first-order polynomial was found to be adequate to approximate the variations of the resistivity with temperature in the studied range. Two best-fits were developed for aluminum and steel based on data provided by manufacturers, see Table 2.2 The correlation is introduced in the Joule heating term. Then, the conduction equation, Eq. (2.3), can be solved with the appropriate boundary conditions: $T(0) = T_{\text{anode}}$ and $T(L) = T_{\text{stub}}$. The resulting temperature profile is:

$$T(x) = \left(T_{\text{anode}} + \frac{n}{m^2} \right) \cos(mx) + \frac{T_{\text{stub}} + \frac{n}{m^2} - \left(T_{\text{anode}} + \frac{n}{m^2} \right) \cos(mL)}{\sin(mL)} \sin(mx) - \frac{n}{m^2} \quad (2.7)$$

with

$$m^2 = \frac{bI^2}{kA^2} \quad n = \frac{aI^2}{kA^2} \quad (2.8)$$

From the temperature distribution of Eq. (2.7), the heat flux going through the stubs is calculated from Fourier's law, in such a way that the equivalent thermal resistance reads as

$$R_9 = \frac{T_{\text{anode}} - T_{\text{stub}}}{q_9} \quad (2.9)$$

It should be noticed that we treated the three stubs as a single cylinder with a cross-section area A corresponding to three times the area of one stub. The other components with Joule heating (i.e., rod, yoke and stubs exposing to the airflow in cavity) are different because they lose heat by radiation and convection via their outer surfaces. Therefore, a particular resistance representation for these fin-like elements was developed and is presented below in Section 2.4.

Table 2.2 Best-fits for electrical resistivity of aluminum and steel.

$\rho(T) = a + bT$	$a \text{ } (\Omega \cdot \text{m})$	$b \text{ } (\Omega \cdot \text{m}/^\circ\text{C})$	Fitting temperature range, $T \text{ } (^\circ\text{C})$
Aluminum	3.048×10^{-8}	1.09×10^{-10}	0-300
Steel	1.88×10^{-8}	6.21×10^{-10}	200-450

Above the anode cover, gases in the cavity are in movement, and therefore a convection condition applies. All convection resistances are of the form $1/hA$: R_{6a} (bath-to-cover), R_5 (cover-to-gas), R_4 (hood and superstructure-to-gas), and R_3 (outer hoods surface-to-potroom). The method used here to determine the convection coefficients as a function of the ventilation rate consists in performing CFD simulations for a given geometry. The detailed CFD model is presented in literature (Zhao et al. 2013), and due to space limitation, it will not be described here. The relevant results for the present paper achieved from the CFD analysis is reported in Table 2.1. CFD simulations have the advantage of providing detailed information (i.e., velocity, pressure, temperature distributions), but at the cost of heavy computational times. However, once CFD results are available, they can be included in network models such as the one described here for further investigations.

Finally, the third pathway by which heat escapes from the bath to the top is through the anode as discussed above. A portion of the heat then continues its way in the anode cover above the anodes (R_7), and is eventually released in the gases under the hood (R_5). Another portion of the heat is released via the steel stubs and the anode assembly. The heat loss from the anode assembly into the gases under the hoods and into the potroom is shown in Fig. 2.2b, and relies on expressions developed below in Section 2.4

for fin-like elements with internal heat generation (resistances R_8 , R_9 , R_{11} , R_{12} , R_{13} , and R_{14}).

The rest of the thermal circuit corresponds to the heat gained by the air flow in the cavity under the hood (ventilation), R_1 , which is calculated as in Eq. (2.1). Also accounted for is the heat that is transferred through the hoods and superstructure into the potroom (R_3). A convection coefficient of $10 \text{ W/m}^2\cdot\text{K}$ was applied on the outer surface of the hoods which represents a typical value for natural convection conditions (Abbas 2010).

2.3.2 Radiation sub-network

The radiation sub-network is illustrated in Fig. 2.2c. In this model, some components with relatively small surface area were neglected, including the feed hole, the gaps between hoods and the gas outlet. In addition, the air with low CO_2 concentration (typically $\sim 1\text{-}1.5\%$) in the space under the hoods can be regarded as a non-participating medium, and thus only surface-to-surface radiation needs to be considered. The alumina feeding system is simplified as a part of the superstructure. Thus, in the end, five surfaces were included in the sub-network: (i) anode cover, (ii) hoods and superstructure, (iii) rod, (iv) yoke and (v) three stubs. As can be seen in Fig. 2.2c, the radiative interactions between the rod, yoke and stubs were neglected, because of their small areas for radiation heat exchange. Also, due to the geometrical symmetry and periodicity of the anode disposition (i.e., anodes are aligned in two columns in the pot), the heat loss from a sub-section containing only one anode to the surrounding sections by convection and radiation is compensated by heat influx from the others. Accordingly, we assume that the radiation heat exchanges involved in each section containing one anode can be considered as those in an isolated system.

To solve the radiation sub-network, it is required to calculate the view factors for each possible pair of surfaces. Since the heat loss from one unit (i.e., a sub-domain with only one anode) to neighbors is compensated by the surrounding units heat loss based on the symmetrical structure, we can use a closed network to calculate the radiation heat exchange among all involved surfaces. When calculating the view factor for each pair of

surfaces, we assumed that the rod and assembly is surrounded by the anode cover and the hoods and superstructure, both of which can be viewed as infinite surfaces. Thus, the view factor from rod, yoke or stubs to anode cover or hoods and superstructure can be approximately assumed to 0.5. For example, for the view factor from the rod to the anode cover, $F_{\text{rod-cover}} \approx 0.5$, and then $F_{\text{cover-rod}}$ is calculated by reciprocity (Modest 2013)

$$F_{\text{cover-rod}} = \frac{A_{\text{rod}} F_{\text{rod-cover}}}{A_{\text{cover}}} \quad (2.10)$$

where A is the area of the corresponding surface. This strategy was also applied to the remaining components. Surfaces are assumed to be gray and diffuse. A network representation of radiative exchanges between surfaces was built (Fig. 2.2c). Energy balance was performed at each J-node. Note that this network is not a thermal circuit as the one in Fig. 2.2b. For example, nodes represent radiative fluxes rather than temperature. Radiative resistances between two J-nodes i and j are of the form $(A_i F_{ij})^{-1}$, whereas radiative resistances between E_i and J_i nodes assume the form $(1-\epsilon_i)/(A_i \epsilon_i)$. The corresponding radiative network was solved in the form of a matrix system, the unknowns of which were the radiosities J_i at all involved surfaces, see Refs. (Modest 2013; Bergman et al. 2011).

2.4 Resistance of fin-like components with internal heat generation

The anode assembly above the anode cover has a geometrical similarity with pin fins (Bergman et al. 2011). Three different cross-sections are observed in the anode assembly, i.e. that of the rod, the yoke, and the three exposed stubs. The straightforward expression of thermal resistance for a pin fin is not valid here, because it is developed by considering only conduction in the fin and convection at the surface of the fin. The heat transfer in the anode assembly, however, also involves significant radiation losses from the surface of the fin-like element, and Joule heating inside the fin-like element. The thermal resistance for such fin-like components is derived in the present section. In order to do so, an energy balance is performed below.

Applying the conservation of energy law to the fin differential element in Fig. 2.3a, we obtained

$$q_x + dq_{jh} = q_{x+dx} + dq_{conv} + dq_{rad} \quad (2.11)$$

where q_x and q_{x+dx} are the conduction heat transfer rate at position x and $x+dx$ respectively, dq_{jh} is the heat generated by Joule heating within the differential element, and finally dq_{conv} and dq_{rad} are the convection and radiation heat losses from the exposed surface of the differential element. From Fourier's law, the heat transported by conduction is simply

$$q_x = -kA \left. \frac{dT}{dx} \right|_x \quad (2.12)$$

where A is the cross-sectional area. Here, we assumed k to be constant, because in the range of temperatures under investigation and for the materials considered, variations of k were found to be below 20% based on data from manufacturers.

The Joule heating term in Eq. (2.11) can be evaluated by:

$$dq_{jh} = I^2 \frac{\rho(T)dx}{A} \quad (2.13)$$

where I is the electric current through the anode assembly and $\rho(T)$ is the temperature-dependent electrical resistivity.

Based on Newton's law of cooling, the convection heat losses at the surface of the infinitesimal control volume of Fig. 2.3a is expressed as

$$dq_{conv} = h_{conv} dA_s (T - T_{gas}) \quad (2.14)$$

where h_{conv} is the convection coefficient at the surface, and dA_s is the surface area of the control volume exposed to convection. T and T_{gas} represent the temperature of the differential element and the temperature of gases in the core of the cavity, respectively. The heat transfer coefficient could be estimated based on correlations between the Nusselt number and other dimensionless numbers (e.g., Reynolds, Rayleigh, Prandtl) for a specified flow geometry and flow regime. For example, as a first approximation, the fin-like elements considered here could be approximated as cylinders in cross-flows, but it should be clear that the fluid flow is actually more complex than that. Therefore, in this work, we employed CFD simulations to obtain specific correlations for the average convection coefficients. The detailed method to calculate the coefficients is discussed in (Zhao et al. 2013).

As for the radiation losses by the surface of the fin-like elements, it was linearized through the use of an average linearized coefficient, h_{rad} . Applying the conservation of energy principle, one can calculate this coefficient as

$$h_{\text{rad}} = \frac{q_{\text{rad}}}{P \int_0^L [T(x) - T_{\text{gas}}] dx} \quad (2.15)$$

where q_{rad} is the total radiation heat transfer rate at the surface of the component, which is taken from the results of the radiation heat transfer network. P is the perimeter of the cross-section and L , the length of the fin-like element. The temperature $T(x)$ in Eq. (2.15) is the temperature along the fin-like element, and will be derived below (Eq. (2.20)). Since the calculation of h_{rad} depends on the fin temperature, and since the fin temperature depends on h_{rad} , an iterative procedure needs to be implemented. The integral in Eq. (2.15) was performed numerically in the present work. This choice was based on the fact that the temperature along the fin-like elements is likely to vary substantially, resulting in significantly different local heat losses along the fin. Fin like elements were divided into small slices and the heat losses for each slice was deduced based on the fin local temperature. Then, the total losses were calculated by summing the losses of each slice. This method also applies to the calculation of convection heat transfer rates on surfaces of fin-like elements such as R_{12} .

Note that it would have been possible to implement a simpler model in which the calculation of radiation exchanges by fin-like element surfaces would have relied on an average temperature (e.g., arithmetic average of the base and tip temperatures) rather than on a numerical discretization. This simplified method was tested by comparing resulting temperatures with the results of the above-mentioned model. After simulations, differences of 10 to 15°C were found for the temperature of anode assembly components (i.e., T_{stub} , T_{yoke} , and T_{rod}). Therefore, depending on the precision required, the simplified or the integral approach could be used. For achieving the results presented in this work, only the integral method was used though.

Once h_{rad} is known, the radiation heat transfer rate of the differential element can be expressed as

$$dq_{\text{rad}} = h_{\text{rad}} dA_s (T - T_{\text{gas}}) \quad (2.16)$$

Combining Eqs. (2.11)-(2.16), and introducing $\theta = T - T_{\text{gas}}$, one can obtain the following governing equation for fin-like elements with both radiative and convective heat transfer at their boundary, and with Joule heating:

$$\frac{d^2\theta}{dx^2} - m^2\theta + n = 0 \quad (2.17)$$

with

$$m^2 = \left[\frac{(h_{\text{conv}} + h_{\text{rad}})P}{kA} - \frac{bI^2}{kA^2} \right] \quad n = \frac{aI^2}{kA^2} + \frac{bI^2T_{\text{gas}}}{kA^2} \quad (2.18)$$

The solution of the fin equation is of the form

$$\theta = C_1 e^{mx} + C_2 e^{-mx} + C_3 \quad (2.19)$$

The two boundary conditions that apply are: $\theta(0) = \theta_b$ and $\theta(L) = \theta_L$. These conditions are used to determine the constants C_1 and C_2 . C_3 is obtained by simply inserting Eq. (2.19) into Eq. (2.17) (i.e., $C_3 = n/m^2$). The temperature profile is calculated as

$$\theta(x) = \frac{\left(\theta_L - \frac{n}{m^2} \right) \sinh mx + \left(\theta_b - \frac{n}{m^2} \right) \sinh m(L-x)}{\sinh mL} \quad (2.20)$$

Knowing the temperature profile $\theta(x)$ from Eq. (2.20), the heat transfer rate at the base (q_b) and at the tip (q_l) of the fin-like element can be calculated from Fourier's law, Eq. (2.12).

Furthermore, the total heat generated by Joule heating, q_{jh} , is calculated by integrating Eq. (2.13) from $x = 0$ to $x = L$ with the temperature profile as calculated previously.

Finally, the heat transfer rate lost by convection and radiation is

$$q_{\text{am}} = q_b + q_{jh} - q_L \quad (2.21)$$

The thermal circuit representation of the fin-like element treated in this section is shown in Fig. 2.3a. A resistance from the base of the fin to the gas is used to account for the heat

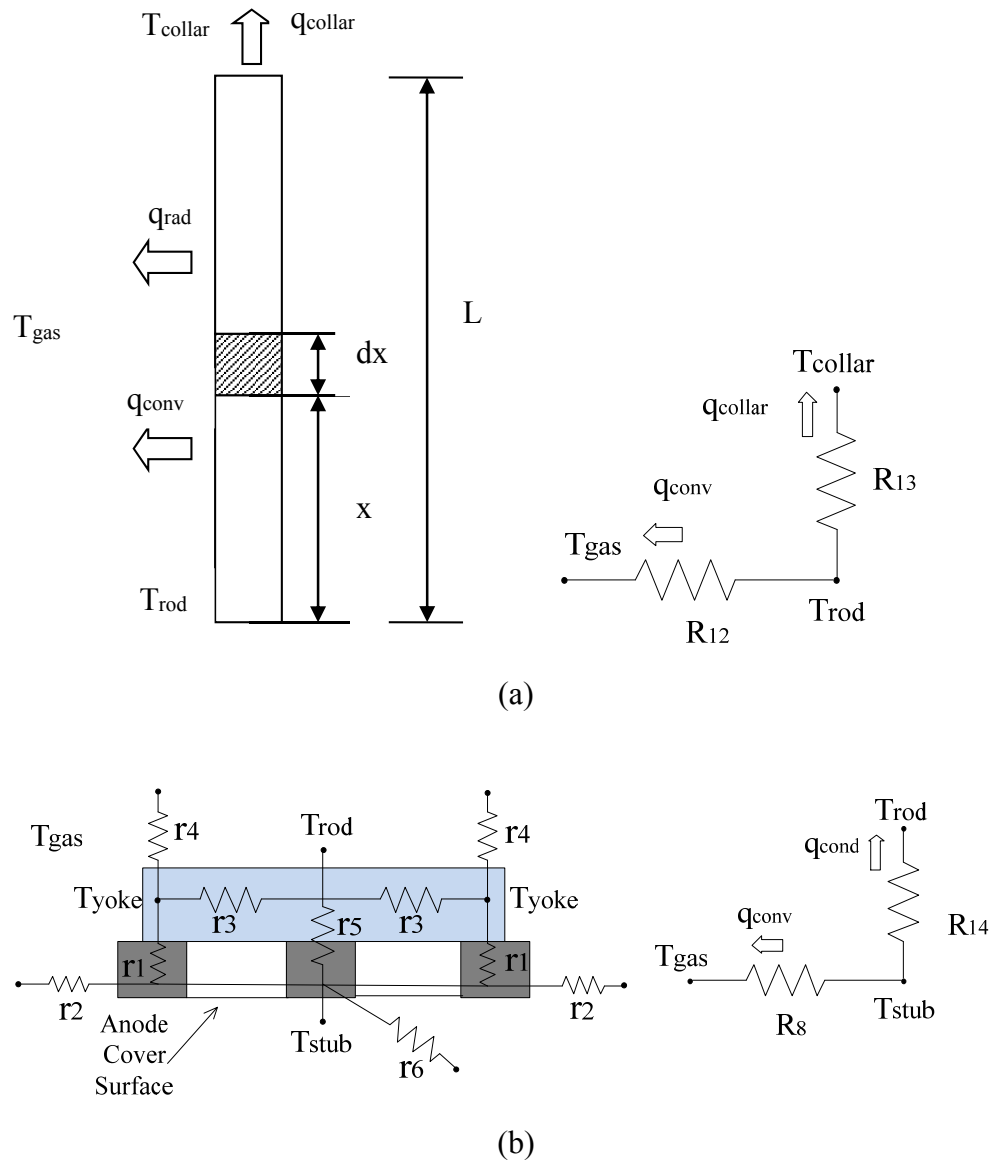


Figure 2.3 Example of a fin-like element and its thermal resistance representation.

losses by the surface of the fin-like element, and a second resistance connects the base of the fin to its tip in order to calculate the heat that leaves the tip of the fin by conduction. These resistances are calculated by dividing the heat transfer rates by the adequate driving temperature difference. For example, the equivalent thermal resistance to calculate the heat transfer by conduction in the rod at the collar is labeled R_{13} in Figs. 2.2 and 2.3, and R_{12} is the resistance used to calculate the convection heat loss from the rod to the air in the cavity. For calculating R_{11} , which is used to calculate the heat losses by

the part of the rod that extends outside of the pot, Eq. (2.17) can also be used by assuming a prescribed temperature tip condition ($T_{\text{tip}}=T_{\text{atm}}$) corresponding to the upmost tip of the rod and an effective heat transfer coefficient (h_{eff}) representing the combination of convection and radiation coefficients. Detailed expressions are summarized in appendix.

Note that in the thermal circuit in Fig. 2.2, resistances R_8 (stub-to-gas resistance) and R_{14} (stub-yoke-rod resistance) are actually a combination of resistances, representing the overall convection and conduction resistances of the joint structure shown in Fig. 2.3b. Heat coming from the anode is first conducted into the three stubs, then converges to the center of the yoke, and finally travels into the rod. Along the surface of these components, heat is lost by convection and radiation. Only the conductive (r_1, r_3, r_5) and convective (r_2, r_4, r_6) resistances are shown in Fig. 2.3b, the radiative heat transfer having already been considered in the radiation sub-network. The three stubs of the anode assembly were treated as three parallel fin-like elements and the above yoke was divided as two horizontal fin-like elements. For each element, the equivalent resistances were determined by using the aforementioned analysis. The network of Fig. 2.3b (left) is then simplified by combining resistances in series and in parallel until it becomes as the one on the right side of Fig. 2.3b. Detailed expressions are also summarized in appendix.

2.5 Numerical implementation and validation

The thermal circuit described above was solved in Matlab. An energy balance was performed at all temperature nodes of the network (i.e., 7 nodes). The resulting set of equations was written in a matrix form. Due to non-linearity (e.g., properties that depend on temperature, radiation, etc.), an iterative solution procedure needed to be implemented. Starting from an initial guess for the temperature at each node, the matrix components were computed. Then, the matrix system was solved. The matrix components were updated based on the new values of temperature, and so on. The procedure is repeated until convergence. Convergence was declared when the change at each node temperature was smaller than 0.01 K compared to the values of the previous iteration. Note that under-relaxation was required to achieve convergence. Typically, a simulation took 1 minute with an under-relaxation factor of 0.01.

For the calculations presented in this work, the geometrical features of the system considered were that representative of the electrolytic cells at ADQ. The parameters in normal operating conditions were taken either from ADQ or from literature, see Table 2.3. A particular challenge consisted in determining the values of the heat transfer coefficient on different components of the system. The flow pattern under the hood is complex and it is hazardous to use correlations for flat plates with parallel flow or for cylinders in cross-flow since this is far from the actual heat transfer and flow configuration. Here, CFD simulations were used to obtain accurate convection coefficients (Zhao et al. 2013).

The resulting program was validated thoroughly in different ways. First, the exhaust gas temperature for different ventilation rates was compared to that of experimental measurements (Gadd et al. 2000). A conversion of the draft condition should be performed in order to achieve the same ventilation rate per anode. A good agreement between our results and (Gadd et al. 2000) was found. At high ventilation rate, our resulting exhaust temperature deviates from their results by less than 5°C while the difference is about 10°C in low ventilation rate (<40% normal condition).

In addition, several specific parameters were compared with the data available in literature. For example, experiments (Taylor 2007; Eggen et al. 1992) have demonstrated that the heat transfer coefficient on the anode cover is in the range from 9 W/m²·K to 14 W/m²·K. In our model, this parameter is 13.1 W/m²·K in normal condition. The heat flux through the anode cover of the mixed crushed bath and alumina reported in Shen et al. work (Shen et al. 2008) is in the range from 1700 W/m² to 2700 W/m². Here, we obtained a value of 2123 W/m². Another coarse validation is based on the “rule of thumb” that the total top heat loss is about 25% of the total energy input. Since the total voltage drop in the pot is about 4 V and the current imposed in one aluminum bar is 8750 A, the top heat loss should be of the order of magnitude of 8750 W. Our modeled result is 8196 W. Therefore, the model is considered to capture adequately the heat transfer mechanisms in the system considered.

Table 2.3 Thermo-physical parameters considered in the calculations.

Parameter	Value	Source
Current in each rod (A), I	8750	From ADQ
Normal draft condition per pot (Nm^3/s), Q_N	2.4	From ADQ
Emissivity of hoods, superstructure, rod, yoke and stubs	0.8	Oxidized rough metal surface, from (Green et al. 2008)
Emissivity of anode cover	0.4	Measurement from (Rye, Thonstad, and Liu 1995)
Bath temperature ($^{\circ}\text{C}$), T_{bath}	955	From ADQ
Ambient temperature ($^{\circ}\text{C}$), T_{atm}	30	From ADQ
Hot gas source for each anode (kg/s), \dot{m}_{CO_2}	0.0012	From ADQ, based on 1.3% molar concentration of hot gas in effluents
Specific heat of CO_2 at 955°C ($\text{J/kg}\cdot\text{K}$), C_{p,CO_2}	1200	Adopted from (Bergman et al. 2011)
Specific heat of air at 120°C ($\text{J/kg}\cdot\text{K}$), $C_{p,\text{air}}$	1013	Adopted from (Bergman et al. 2011)
Thermal conductivity ($\text{W/m}\cdot\text{K}$)		From ADQ
Anode, k_{anode}	5.35	From (Shen, Hyland, and Welch 2008)
Steel (in the cavity), k_{st1}	44	
Steel (in anode cover), k_{st2}	38	
Aluminum, k_{al}	220	
Anode cover, k_{cover}	0.5	
Crust, k_{crust}	1	
		From (Abbas 2010)
Electrical resistivity of carbon ($\Omega\cdot\text{m}$), ρ_{anode}	4.1×10^{-5}	From ADQ
Effective heat transfer coef. ($\text{W/m}^2\cdot\text{K}$) on the external surface of hoods and superstructure, h_{eff}	10	From (Abbas 2010)
Effective heat transfer coef. ($\text{W/m}^2\cdot\text{K}$) from bath	100	From (Taylor et al. 1996)

surface to crust, $h_{\text{bath-crust}}$		
---	--	--

2.6 Effect of ventilation rate

From a waste heat recovery perspective, it is beneficial to increase the effluent temperature as high as possible since the grade of the energy (or the exergy (Nowicki et al. 2012)) is directly related to the hot source temperature (in this case, the exhaust gas temperature). One way to increase the exhaust gas temperature is to reduce the ventilation rate of the cavity under the hood. This could be achieved by diminishing the pressure difference imposed by the fan of the gas collecting duct network, or by diminishing the size of the gaps between hoods. In the present study, we focused only on the first option. Another reason that could encourage one to reduce the ventilation rate is that it would increase the CO_2 concentration at the outlet of the pots, which would facilitate the implementation of carbon capture systems (David and Herzog 2000; Alie et al. 2005). The thermal circuit model was used to study how the temperature in the system and the heat transfer rates in the different components were affected by a change of the ventilation rate. Results are shown in Figs. 2.4 and 2.5. A typical normal draft condition is illustrated by the vertical line.

The temperature of the effluents increases when ventilation rate is reduced. This was also shown previously in (Gadd et al. 2000). For example, we note in Fig. 2.4 a significant gas temperature increase of approximately 100°C when the ventilation rate is reduced to 20% of the normal draft condition. However, an extremely low draft condition in current pot structure will lead to a low negative pressure in the space under the hoods, which might result in gas leakage in the potroom. Moreover, this can also cause overheating of other components (i.e., we observe a significant temperature increase of the other components in Fig. 2.5a) and thus lead to problems in practical operations.

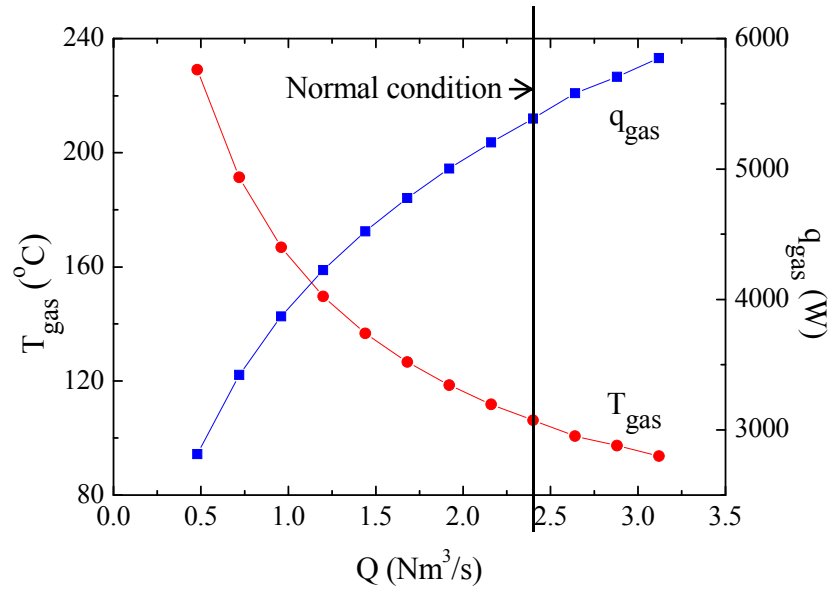
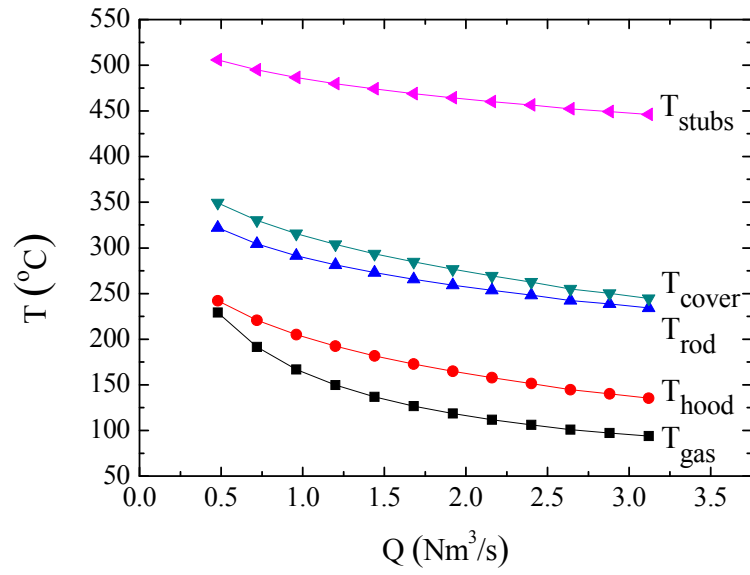


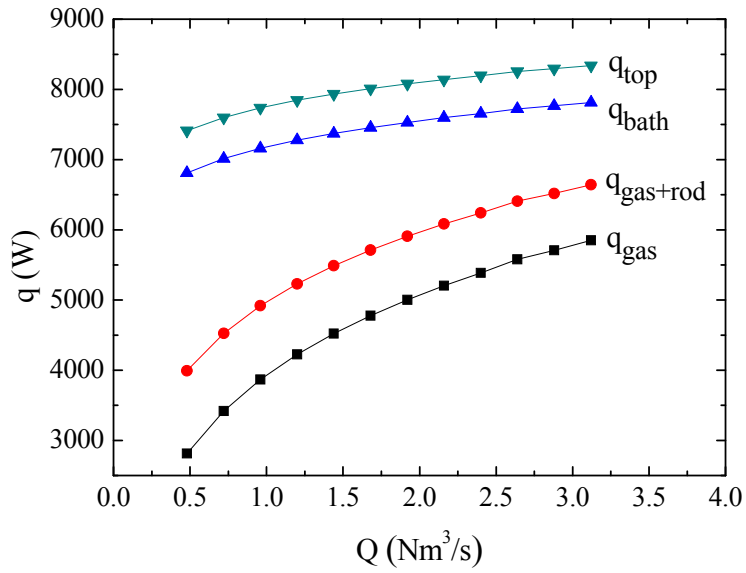
Figure 2.4 The variation of the off gas temperature and its heat content with the draft conditions Q (effluents volumetric flow rate for one pot in ADQ), 2.4 Nm^3/s is the normal ventilation condition in ADQ.

In Fig. 2.5b, we show the heat transfer losses from the effluents, from the rods and from the hoods. The total top heat loss q_{top} (i.e., summation of the three contributions mentioned previously) is relatively insensitive to the ventilation rate. However, the way in which this heat loss is distributed between the three contributions changes with the ventilation rate. The heat content of the exhaust gas is reduced drastically when the ventilation is decreased, which means that more heat will be dissipated to the ambient potroom from the hoods and the rods. This is undesirable in view of heat recovery applications. Therefore, when investigating changes of ventilation rates, there is a clear tradeoff to be made between the temperature level of the waste heat and the amount of heat available in the effluents.

It could also be noted in Fig. 2.5b that the heat lost by the rod (the discrepancy between the curves of $q_{\text{gas+rod}}$ and q_{gas}) is almost independent of the draft condition. Also shown in Fig. 2.5b is the total heat removed from the bath (including the heat generated in anode) through the top section of the pot. Its value is always smaller than the total heat loss from the superstructure. The difference between the two curves represents the energy



(a)



(b)

Figure 2.5 Effect of the pot ventilation rate Q on: a) the temperature of the components of the superstructure, and b) the heat transfer rate through these components.

dissipated in the cavity by Joule heating in the anode assemblies. This difference is also relatively independent of the ventilation conditions. Nevertheless, the heat extracted from the bath could be reduced by almost 1 kW per anode as the draft condition goes down to low levels. This over-insulating effect in top heat loss could influence the global thermal balance in a pot and disturb the working conditions in the bath, since the frozen electrolyte layer (protecting the pot ledge from suffering harsh conditions in bath) on sidewall is very sensitive to the heat flux through it and the sidewall heat flux is directly influenced by the top heat loss. Careful pot redesign or change of pot operation should be considered to prevent thermal imbalance when trying to reduce the ventilation.

2.7 Effect of heat transfer coefficients on different surfaces

As described in the previous section, in view of waste heat recovery applications, the ideal situation would be to reduce the draft in order to increase the effluent temperature, and at the same time, try to increase the heat content of the effluent and maintain the heat removed from the bath. In order to meet these conditions, one should try increasing the heat removal from the components in the cavity, including from the bath. This means increasing the effective heat transfer coefficients while reducing at the same time the ventilation rate in the cavity. This could be achieved, for example, by changes of geometry of the gaps and hoods, by the addition of fins (for example, the effective heat transfer coefficient would be $h\eta A_f/A$ where η is the fin system efficiency and A_f , its surface area, while A is the unfined surface), etc.

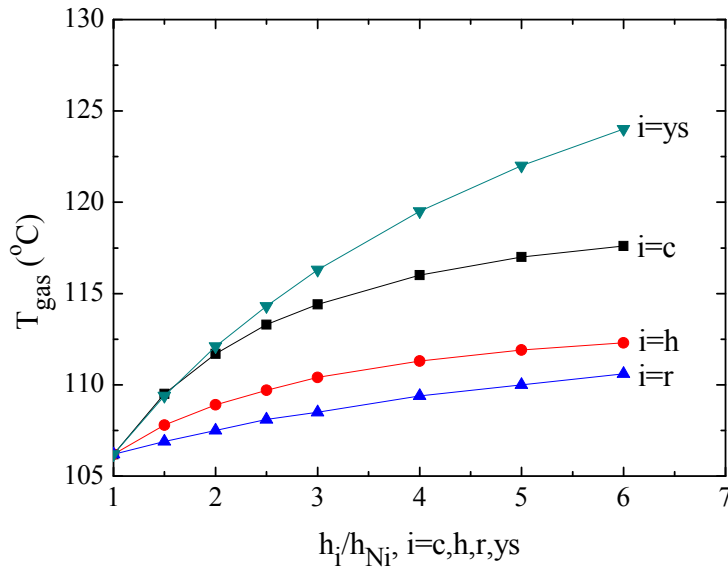
When the mass flow rate of the exhaust gas is reduced, the effective thermal resistance from the bath to the ambient is increased and the heat flux is reduced. Since heat is transferred into the gas under the hoods by convection, the convective resistance can be diminished by enhancing the convective heat transfer coefficient on the contact surface to counterbalance the effect of the reduced mass flow rate. As discussed above, four surfaces with relatively large area are considered in the network, including the top surface of the anode cover, the surfaces of yoke, stubs and rod and the internal surface of the hoods and superstructure. The sensitivity of the gas temperature and heat transfer rates to the variation of the convective coefficient on each of these surfaces should be tested to find the most influencing factor.

In this conceptual investigation, we performed the calculations by varying only one heat transfer coefficient at a time. For example, the value of the heat transfer coefficient on the anode cover was changed gradually from normal condition to higher values, and simulations with the present model were performed for each different value of h_{cover} . Then, the same procedure is repeated for the other heat transfer coefficients. The results are reported in Fig. 2.6 for normal ventilation rate ($2.4 \text{ Nm}^3/\text{s}$) and a reduced ventilation rate condition corresponding to 40% of the normal rate ($0.96 \text{ Nm}^3/\text{s}$). The x-axis reports the convection coefficient ratio (actual over normal), while the y-axis shows the temperature of the effluents.

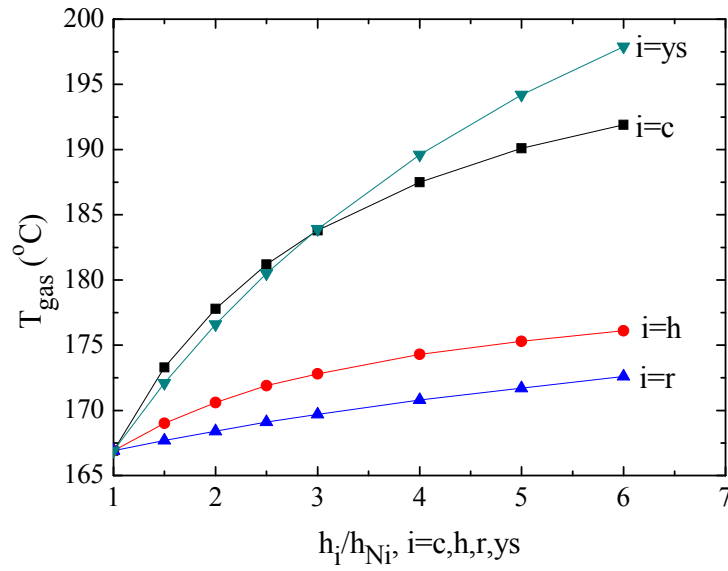
It can be found that the increase of heat transfer coefficients on anode cover, and yoke and stubs has a stronger influence on the gas temperature, compared to those on rod and hoods. This could be explained by the fact that the anode cover has a relatively high temperature and a large contact area with the gas under the hoods, and the yoke and stubs, although they have small areas, exhibit high temperatures. On the other hand, the temperature difference between the gas under the hoods, and the rod and hoods is relatively small, so an increase of the heat transfer coefficients on these surfaces has a relatively small impact on the gas temperature.

Reported in Fig. 2.7 are the heat transfer rates in different components while varying the convection coefficient on the two most influential surfaces (anode cover, yoke and stubs). This work was performed for normal ventilation condition, Fig. 2.7a, and reduced draft, Fig. 2.7b. Heat transfer rates increase with the increase of convection coefficients. The convection coefficient on the yoke and stubs seems to be slightly more influential than that on the anode cover.

An interesting feature of Fig. 2.7b is that the heat transfer rate from the bath under a reduced ventilation rate can reach a value close to that under normal ventilation condition due to the increase of convective coefficients. This means that it would be theoretically possible to maintain the heat balance of the pot under reduced ventilation conditions, and at the same time increase the effluents temperature. This would require increasing the convection coefficient on the anode cover and on the stubs and yoke.



(a)



(b)

Figure 2.6 Effect on gas temperature of increasing convection coefficients on different surfaces on the gas temperature for: a) normal ventilation rate, and b) reduced ventilation rate (40% of normal draft). (c, h, r, ys represent anode cover, hood and superstructure, rod and yoke and stubs respectively)

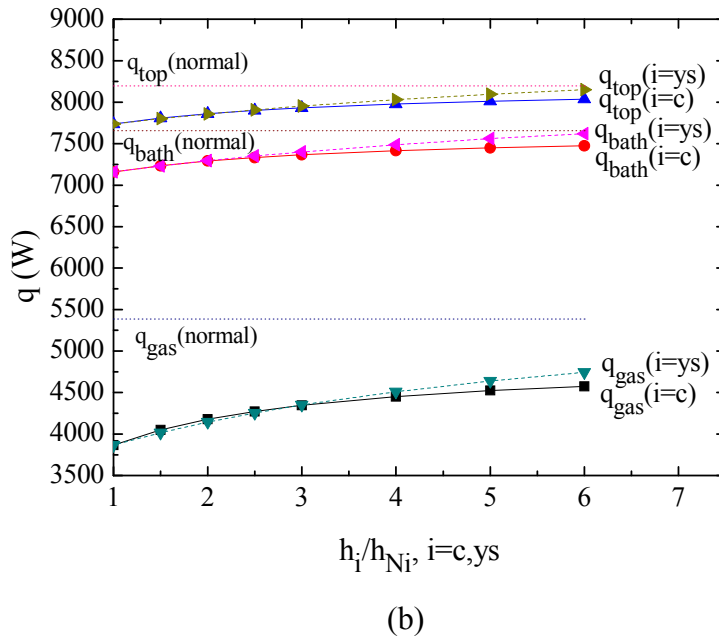
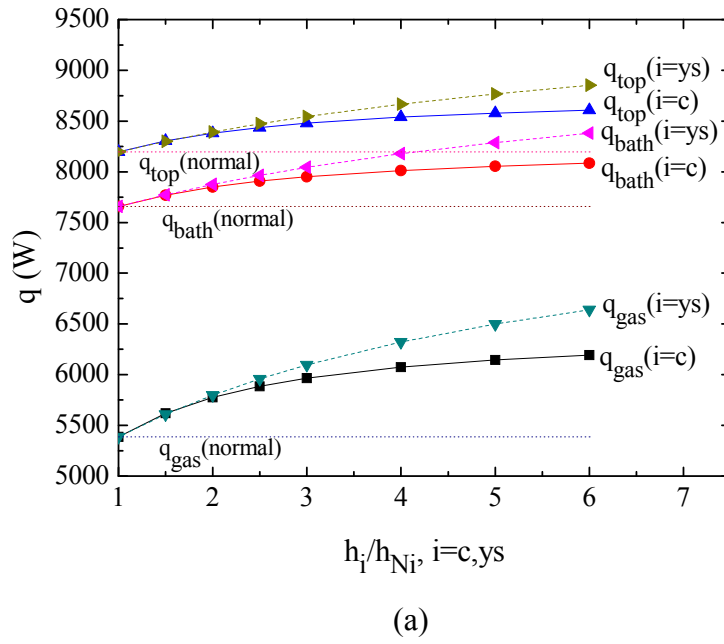
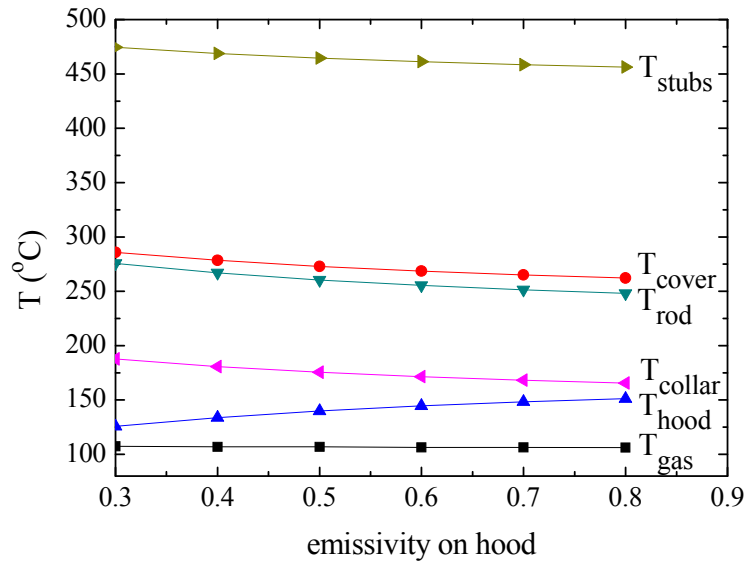


Figure 2.7 Effect on heat transfer rates of increasing convection coefficients on different surfaces on the gas temperature for: a) normal ventilation rate, and b) reduced ventilation rate (40% of normal draft).

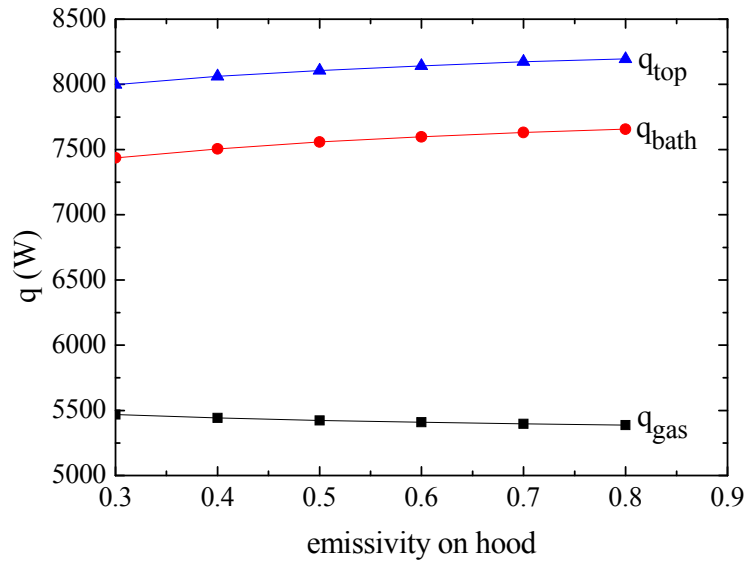
2.8 Effect of the surface emissivity

Another way to modify the heat transfer balance within the superstructure is by changing the emissivity of the internal surfaces of the hoods. As for the anode cover, it appears difficult, if at all possible, to modify its surface emissivity in a simple way. The other surfaces have a small surface area (surface of the yoke, stubs, and rod) and changing their emissivity will not affect significantly the gas temperature. Simulations with different values for the emissivity of the internal surface of hoods were performed in normal condition and results are reported in Fig. 2.8. The temperature of most superstructure components is only changed slightly by the value of emissivity (Fig. 2.8a). In particular, the gas temperature is almost insensitive to the emissivity value. The only temperature that changes significantly is in fact that of the hoods, which increases with the emissivity.

In Fig. 2.8b, we show that the corresponding heat transfer rate transported by the effluent decreases slightly when the emissivity increases, but the change is very small (less than 2%). On the other hand, the heat dissipated in the potroom increases with the emissivity since more heat is absorbed by the inner hood surfaces.



(a)



(b)

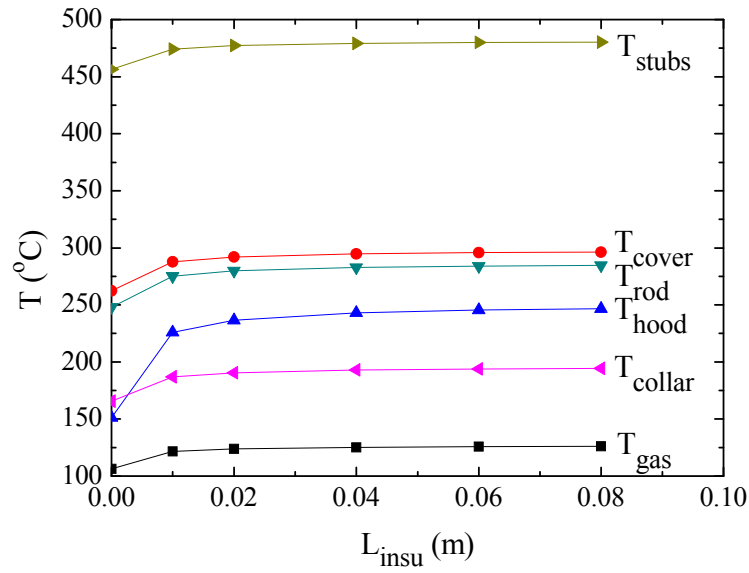
Figure 2.8 Effect of the emissivity of hoods on: a) the temperature of different components, and b) the heat transfer rates through these components.

2.9 Influence of hoods insulation

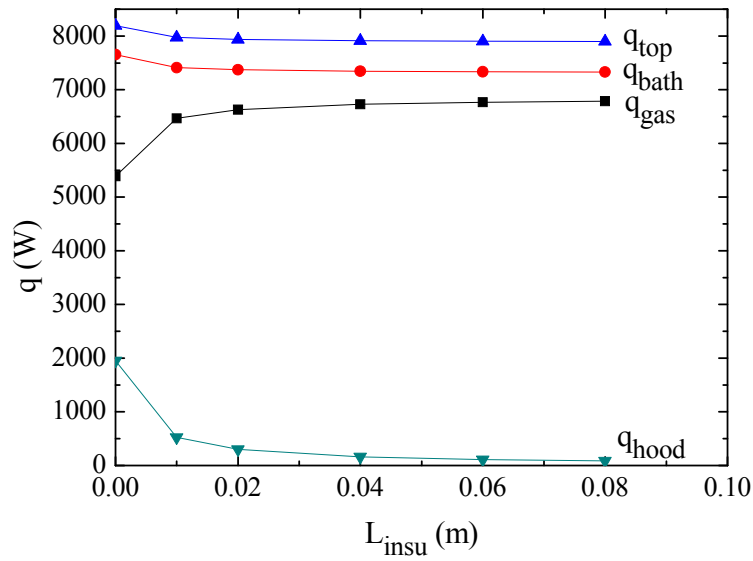
As seen in previous section (e.g., see Fig. 2.5b), we observe that the heat loss from the hoods to the atmosphere accounts for a considerable part of the total top heat loss (approximately 30% under high ventilation rate and 60% under low ventilation rate). Enhancing the insulating quality of hoods is another approach to enhance the quality of the exhaust gas in the cavity (i.e., to increase its temperature) since this will tend to keep the heat inside of the pot. Here, we considered that an insulating layer of thickness varying between 0 and 0.1 m with a thermal conductivity of 0.02 W/m·K was installed on the hoods. This corresponds to an RSI factor between 0 (no insulation) and 5 (maximal insulation). For each insulation level, the thermal circuit was used to calculate temperatures and heat transfer rates. The main results are shown in Fig. 2.9.

Compared to the reference case (no insulation), there is a significant temperature increase for all components when a 0.01 m (RSI = 0.5) insulating layer is added on the hoods. For example, the temperature of the hoods surface inside of the pots increases by 90°C. The gas temperature increases by approximately 20°C compared with the situation with no insulating, which is significant from a heat recovery perspective. However, continuing to add more insulation provides only marginal gas temperature increase. In other words, above an RSI of 0.5, the temperature of the components inside the top part of the smelter do not change much when more insulation is added.

Figure 2.9b shows that the top heat loss by the exhaust gas increases by 1.5 kW when adding the insulating layer. More importantly, the installation of the insulating layer appears to have a very limited influence on the total top heat loss and on the bath heat loss (approximately 300 W), which is desirable for maintaining the current operating conditions. The insulation mainly acts in such a way that a large amount of heat is absorbed by the exhaust gas rather than escaping from the hoods. Therefore an insulating layer does play a positive role in increasing the gas temperature and the gas heat content. Nevertheless, as observed in Fig. 2.9a, a layer thicker than 0.01 or 0.02 m (RSI = 0.5-1) does not provide additional benefits.



(a)

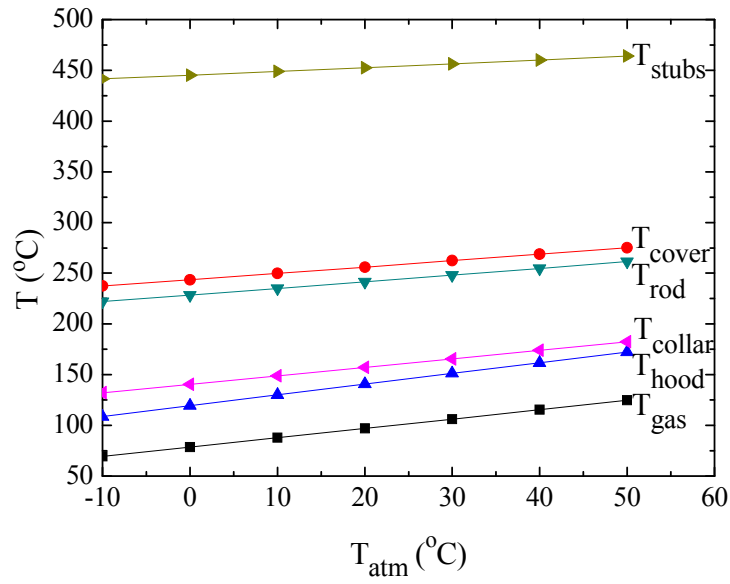


(b)

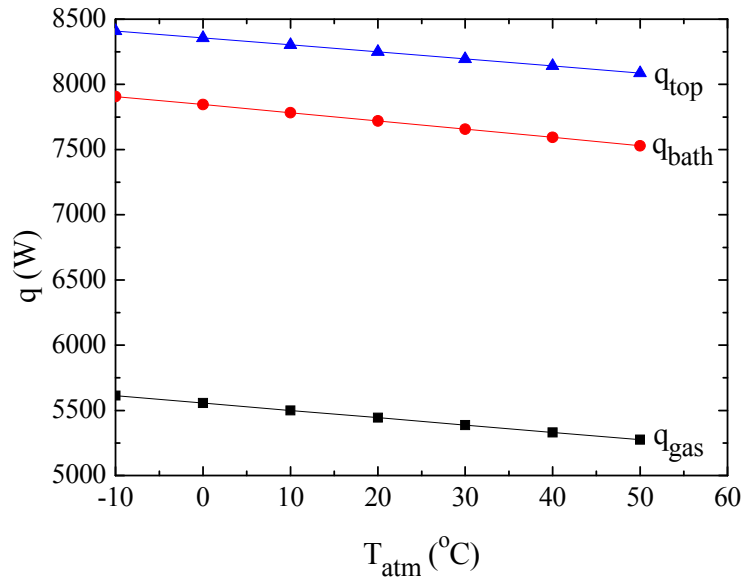
Figure 2.9 Effect of the hoods insulation on: a) the temperature of different components, and b) the heat transfer rates through these components.

2.10 Influence of the potroom air temperature

The temperature of the air in the potroom can vary significantly as a function of the seasons. The envelope of the building in which pots are installed is typically very loose and provides little isolation. Therefore, the temperature of air inside the potroom is affected considerably by outdoor conditions. Typical values in potrooms can range from -10°C to 50°C . Therefore, the sensitivity of the results to the potroom air temperature was tested with the model. The temperature and heat transfer rates of different upper pot components are shown in Fig. 2.10. The increase of temperature of all components with that of the air in the potroom is quasi linear, see Fig. 2.10a. The impact of the potroom temperature is quite important. For example, the gas temperature can be reduced from 125°C to 70°C simply due to seasonal weather changes (i.e., summer vs winter). From a waste heat recovery perspective, this has a strong impact since the technology that would be implemented to recover the waste heat would need to work over an extended range of temperature. Fig. 2.10b shows the corresponding heat transfer rates. When the potroom air gets cooler, all heat transfer rates increase nearly linearly (approximately 5 W per variation of 1°C). This means that the heat content of the effluents is actually larger when it is cold in the potroom. This is due to the fact that more heat is removed from the bath by the cold air inflow in such a case.



(a)



(b)

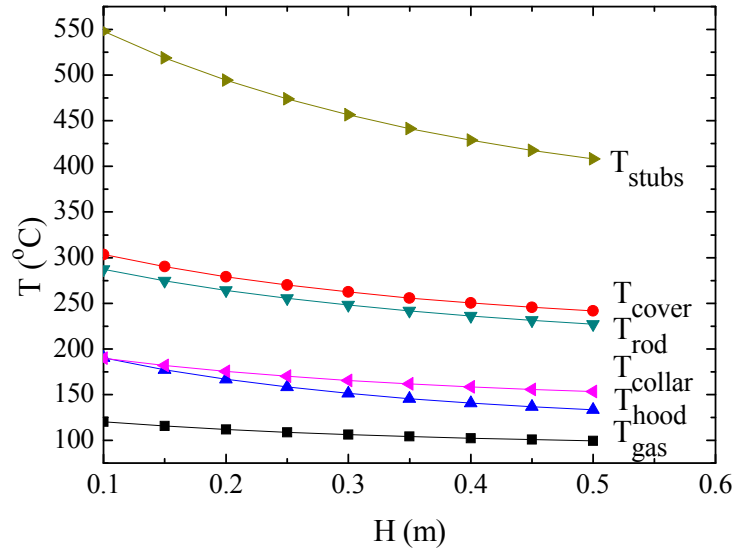
Figure 2.10 Effect of the potroom air temperature on: a) the temperature of different components, and b) the heat transfer rates through these components.

2.11 Influence of anode height

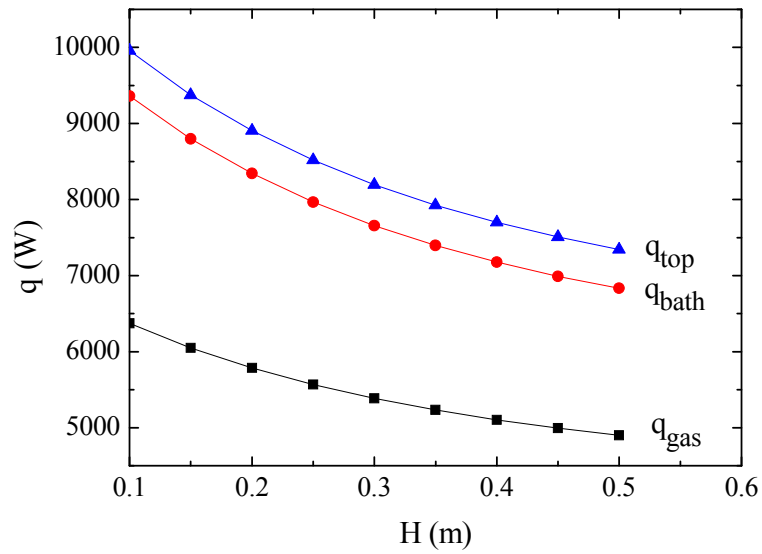
Another potentially important transient effect is the consumption of the anodes, although this happens on a completely different timescale than the seasonal air temperature changes. As an anode is consumed, the control system adapts the position of the anode assembly so as to keep the distance between the bottom of the anode and the aluminum layer constant. Anodes are replaced approximately every two weeks. Therefore, we investigated how the height H of the anode affected the results provided by the model, see Fig. 2.11. Newly installed anodes correspond to the largest H -values, while anodes that are about to be replaced have the smallest H .

The value of H proved to have a significant impact on the temperature of most components, in particular elements closer to the anode (i.e., stubs). Thinner anode provides less insulation from the bath and thus tends to warm up the upper part of the cell. The gas temperature changes from 100 to 120°C due to the change of H caused by anode consumption. The warming of the upper cell due to anode consumption also shows in Fig. 2.11b which reports the heat transfer rates versus H . The heat content of the exhaust gas increases from 5 kW to 6.5 kW from a fresh anode to a consumed one. The total heat loss from the bath also changes drastically, from 7.5 kW to 10 kW.

Although these variations of T and q are quite important from a waste heat recovery perspective, one pot contains many anodes with different levels of consumption in such a way that the temperature at the outlet of a pot upper duct is an average over the range of possible anode heights. Since the present model only considered steady-state, it can be used with an average anode height to determine the average features in an entire pot, or alternatively, used with a specific anode height to determine what happens locally around that anode in the pot. To fully address the transient nature of an entire pot, one would need to consider all the anodes that are in practice at different stage of consumption in the pots.



(a)



(b)

Figure 2.11 Effect of the height of anodes on: a) the temperature of different components, and b) the heat transfer rates through these components.

2.12 Conclusions

This chapter had two main objectives: (i) describe the enhanced thermal circuit that was developed to model heat transfer mechanisms in the upper part of an electrolytic cell, and (ii) perform a sensitivity analysis of temperatures and heat transfer rates with respect to the main design and operation parameters.

As for the first objective, the main outcomes are:

- An enhanced and complete thermal circuit representing the upper part of a pot is documented here. The circuit solves quickly, and can determine temperatures and heat transfer rates in each component.
- We developed an original formulation to account for fin-like elements with internal heat generation in thermal circuit model.
- New correlations are used to determine the convective heat transfer coefficients on the surfaces of interest.

By using the model, we were able to address the second objective. The following observations could be made:

- The mass flow rate of the pot exhaust gas has the most influence on the exhaust temperature and heat content.
- Convection heat transfer is more influential on the top surface of anode cover and on the surface of the yoke and stubs, rather than those of aluminum rod and hoods and superstructure. Further modifications of pot ventilation design should be focused on these efficient areas in the perspective of waste heat recovery.
- Additional insulation on the hoods could increase the exhaust gas temperature and heat content. An RSI of 0.5 appears to be an optimal choice of an insulating level.
- The influence of changing the emissivity of internal hoods and superstructure surfaces provides only a marginal contribution in enhancing the thermal quality of the gas.
- Both the potroom temperature and the anode height significantly affect the heat transfer in the upper structure of the pot. When designing any modifications in the pot, their influences should be carefully taken into account.

Further work should be done to complete the thermal circuit by including a more detailed representation of the superstructure and of the rest of the pot, possibly with thermal

capacitances to account for transient dynamics. Furthermore, an entire pot could be modeled with anodes at different level of consumption. It would also be interesting to verify that the increase of temperature of the joint between the anode rod and yoke under the different scenarios is below the maximal acceptable temperature, which is of importance to maintain the joint strength.

CHAPTER 3 HEAT TRANSFER AND AIRFLOW ANALYSIS IN UPPER PART OF ELECTROLYTIC CELLS BASED ON CFD

Abstract

A CFD model of the top part of an electrolytic cell used in the primary aluminum industry is presented. The model is used to determine average heat transfer coefficients on the main surfaces, under different ventilation rates. Correlations have been developed for the heat transfer coefficient and pressure drop versus pot draft condition. Non-uniformity of the heat transfer coefficient is studied. Finally, the relative importance of natural convection versus forced convection is revealed by the analysis. The knowledge developed in this paper is useful for the heat transfer design and analysis of electrolytic cells, which is crucial in this industry.

Résumé

Un modèle de type CFD du dessus d'une cuve d'électrolyse utilisée pour la production primaire d'aluminium est présenté. Le modèle est utilisé pour déterminer les coefficients de transfert thermique sur les principales surfaces, sous différentes conditions de ventilation. Des corrélations ont été développées pour le coefficient de convection et la perte de charge en fonction du taux de ventilation de la cuve. La non-uniformité du coefficient de convection est étudiée. Finalement, l'importance relative de la convection naturelle versus la convection forcée est révélée par l'analyse. La connaissance développée dans cet article est utile pour le design thermique et l'analyse des cuves d'électrolyse.

3.1 Introduction

The Hall-Héroult process is very intense energetically, and typically electricity accounts for 40% of the total cost in the aluminum production process. Although this technology has been developed one century ago and tremendous efforts have been deployed to enhance performance of smelters, the energy efficiency in modern pots is still relatively low, with about half of the energy input eventually dissipating into the atmosphere in the form of waste heat. Therefore, increasing the overall energy efficiency of smelters still offers promising opportunities of significant economical and environmental outcomes (Nowicki and Gosselin 2012). For example, Nowicki et al. (2012) showed that the exergy (useful work potential) of the exhaust gases from the cells is 0.65 MWh per ton of aluminum produced, and that it is even larger for the heat losses from the different pot surfaces.

Over the years, many investigations have been performed to develop a better understanding of the Hall-Héroult process and to optimize the pot design and operation. With the continuous improvement of computational resources, numerical simulation has become an attractive method to achieve these objectives. Most of the heat transfer studies related to aluminum smelting cells found in open literature have focused on the bath, metal pad, and sidewalls. In particular, the pot domain below the anode cover has received a lot of attention, with the development of several thermal numerical models, often coupled with magnetic, electrical or mechanical numerical models, (e.g., Bruggeman and Danka 1990; Dupuis 1998; Shcherbinin et al. 2003; Dupuis et al. 2004; Severo and Gusberti 2009; Yu et al. 2004; Fortin et al. 2012). These studies helped to improve the operation, control and design of smelting pots.

Despite the rich literature available on numerical models for solving thermo-electrical, thermo-mechanical, and magneto-hydrodynamic problems in aluminum smelters, relatively few numerical models were published to study the top heat loss in the section above the anode cover. Karlsen et al. (1998) proposed a simplified model to estimate the pot gas collection efficiency in the top cavity under hoods based on different draft conditions and pot tightness. A simple thermal circuit model (Taylor et al. 2004) was presented to study the impact of the anode thickness on the temperature of the anode assembly, which interacts with the cross-flow air under the hoods. Recently, Abbas et al.

(2009) presented an investigation of the relationship between fugitive emissions, hood tightness, top heat loss and cell draft based on CFD simulations. A comprehensive description was reported in the reference (Abbas 2010).

In addition to the studies related to the interior of the pots, CFD simulations were also employed to study the impact of the airflow in the potroom (room where electrolytic cells are lined up) on the heat losses of smelters. Based on a commercial code and Hydro Aluminum's model SMASH, the influence of potroom temperature and ventilation on a cell shell temperature, heat balance and side ledge thickness was investigated by Haugland et al. (2003). Tomasino et al. (2004) used different models to determine the heat transfer from the pot to the atmosphere. Maarschalkerwaard (2010) proposed a strategy relying on CFD simulations to optimize the ventilation of potroom by considering the heat dissipation, HF concentration, and the spreading of the hazardous dust.

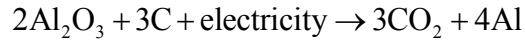
As shown in the above-mentioned literature review, there is currently a lack of data regarding the heat losses from the upper part of smelting pots. One of the purposes of the present paper is to develop correlations that could be used to estimate convection coefficients on different surfaces of the top section of the pot. Since the convective heat transfer coefficients are sensitive to the flow field and geometry of the contact surface, a CFD model was built based on a real scale cell from Alcoa's Deschambault plant (ADQ) located in Canada. Based on a series of CFD simulations, correlations of convective coefficients as a function of cell ventilation were established on the surfaces of anode cover, anode assembly, and hoods. Furthermore, the CFD results are used in order to analyse the details of the heat transfer and fluid flow within the upper part of the electrolytic cell.

3.2 CFD Model

3.2.1 Domain

Primary aluminum is produced in electrolytic cells by the Hall-Héroult process, see Fig. 3.1a. In this process, a cryolitic bath is sandwiched between a carbon anode and a cathode. Alumina (Al_2O_3) is dissolved in the bath. When an electrical current passes

between the electrodes, electrochemical reactions take place, which can be summarized in the following simplified and compact overall reaction:

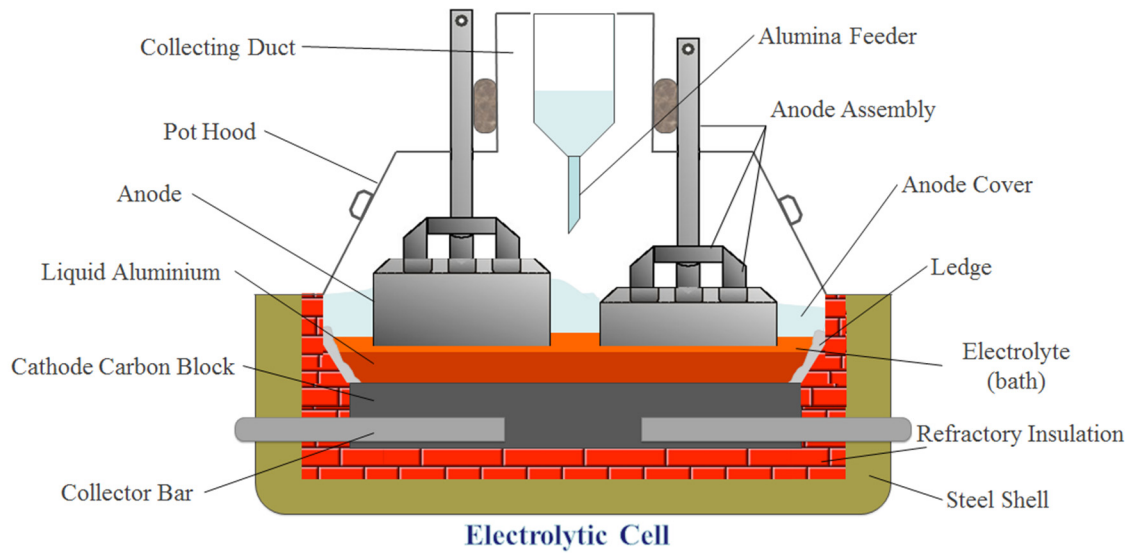


In this reaction, the carbon comes from the anodes: they are literally consumed by the process, and thus need to be replaced regularly. A typical cell contains a few dozens of anodes. The liquid aluminum that is produced accumulates at the bottom of the cell, below the bath. The anode and bath are covered with a porous material layer called anode cover. Each anode block is held by an anode assembly (stubs, yoke and bar) in which the current is passing. The space above the cell is insulated from the potroom environment by hoods. Hoods limit heat losses and prevent hazardous emissions into the potroom. A negative pressure is maintained in the space under the hoods in such a way that potroom air infiltrates by the gaps between hoods. The CO₂ produced in the above-mentioned reaction rises from the bath through the anode cover, and is released in the space under the hood. It is significantly diluted by the infiltration (to concentration around 1%), and is then transported by the collecting duct system to the gas treatment center.

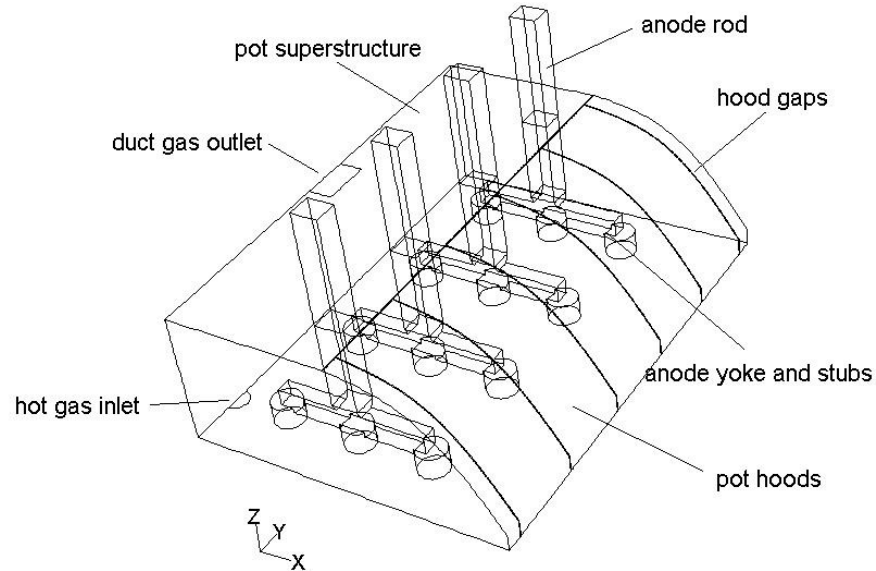
The domain of the CFD model is the section above the anode cover in electrolytic cells, and is shown in Fig. 3.1b. In agreement with the objectives of this work, the following simplifying assumptions are invoked to simplify the simulated geometry and reduce the computational burden:

(i) A typical 350 kA aluminum reduction cell is considered here. It contains 40 anodes, divided in two parallel rows. The effluents are collected in a duct through 5 openings located equidistantly on the top of the cavity under hoods. In this work, we assumed a symmetry plane between the two rows of anodes. Because all anodes in a pot are not necessarily equally consumed, a certain degree of thermal asymmetry could be expected in real pots. Furthermore, we assumed that the flow pattern is periodic in the direction of the anode row, i.e. that the flow in the domain under each opening on the top of the superstructure is similar. This allows us to simulate only one tenth of a pot. In other words, the simulated domain contains only four anode assemblies, the cavity under the hoods and the surfaces surrounding it, as shown in Fig. 3.1b. In real pots, the negative pressure at each opening can vary slightly, resulting in a net flow in the direction of the

anode row. However, this effect is assumed to be small and the air flow and heat transfer in the portion of cavity simulated is expected to be representative of actual conditions.



(a)



(b)

Figure 3.1 The structure of an aluminum reduction cell, (a) complete view, and (b) simulated domain consisting in the top portion of the cell.

(ii) The bottom surface of the simulated domain is the top surface of the anode cover, i.e. the anode cover, anodic blocks and electrolytic bath are not simulated. The inclusion of these components would significantly increase the complexity of the model and the computational cost while they have less influence on the flow and heat in the simulated domain. Open holes due to the collapse of crust were not considered in current simulation. We imposed a uniform heat flux on the anode cover surface which will not affect significantly the results, since the objective here is mainly to determine the convection coefficients.

(iii) The feeding system is omitted in the simulated domain in order to simplify the generation of the domain and mesh.

(iv) The infiltration of air in the cavity under the hood comes from gaps between hoods and at the connection between the hoods and superstructure. No open hoods are simulated.

3.2.2 Governing equations and modeling options

The governing equations for the present problems are those expressing conservation of mass, momentum in each direction and energy, along with a turbulence model. Incompressible flow and steady-state conditions are considered. Pressure work and kinetic energy terms are neglected in energy equation since the gas is treated as an incompressible flow. No species diffusion is involved in the problem. Therefore, the continuity equation (conservation of mass) reads as:

$$\frac{\partial(\rho u_i)}{\partial x_i} = 0 \quad (3.1)$$

The conservation of momentum equations are (written in a Cartesian tensor form):

$$\frac{\partial(\rho u_i u_j)}{\partial x_i} = -\frac{\partial p}{\partial x_i} + \frac{\partial}{\partial x_j} \left(\mu_{\text{eff}} \left(\frac{\partial u_i}{\partial x_j} + \frac{\partial u_j}{\partial x_i} \right) - \frac{2}{3} \rho \delta_{ij} k \right) + \rho \vec{g} \quad (3.2)$$

Finally, the conservation of energy equation is:

$$\frac{\partial(\rho u_i h)}{\partial x_i} = \frac{\partial}{\partial x_i} \left(k_{\text{eff}} \frac{\partial T}{\partial x_i} \right) + S_h \quad (3.3)$$

where the sensible enthalpy of the gas h is defined as $h = \int_{T_{ref}}^T C_p dT$. C_p is the temperature-dependent heat specific of air. The Reynolds stresses term due to the turbulence is modeled based on the Boussinesq eddy viscosity assumption. Therefore, μ_{eff} is the effective viscosity ($\mu + \mu_t$, where μ_t is the turbulent viscosity, defined according to the turbulence model that is used), k is the turbulent kinetic energy and $\delta_{ij} = 0$ ($i \neq j$) or 1 ($i = j$). k_{eff} is the effective thermal conductivity ($k + k_t$, where k_t is the turbulent thermal conductivity, defined according to the turbulence model being used). S_h includes the volumetric heat source due to the Joule heating effect in solids. Viscous heating is ignored in the simulation. Note that in the solids, only the energy equation is solved, and without the advective terms. The volumetric heat generation (Joule heating) is assumed to be uniform in the solids and was calculated based on the typical current and resistivity in each part of the anode assembly.

The air properties (i.e., specific heat, thermal conductivity, and viscosity) are functions of temperature (polynomial fittings based on data published in (Bergman et al. 2011)). The air density was determined based on the “incompressible-ideal-gas” model of the CFD software used (Fluent 2012), and was calculated by:

$$\rho = \frac{p_{op}}{\frac{R}{M_w} T} \quad (3.4)$$

where R is the universal gas constant, M_w , the molecular weight of the gas, and p_{op} , the defined operating pressure. Under this approach, the density depends only on the operating pressure, and not on the local relative pressure field. In this form, the local density field depends on the local temperature field, and thus buoyancy forces can be considered in the momentum equations.

To account for turbulence, each variable was expressed as the summation of a time-average variable plus a fluctuating component, and then the conservation equations were averaged over time. A turbulence model is required to close the model. Generally speaking, two approaches are available to simulate the region close to the walls of the domain. One approach relies on semi-empirical formulas called “wall functions”, while the other calculates the detailed flow in the wall region. The first method is popular in industrial applications because it uses a wall function to calculate the near wall flow

feature and thus tremendously reduces the computational time. However, despite of its advantages, the wall function method appears weakly adequate to describe the near wall region with low Reynolds number flows, since the empirical formulas were established from experiments with high Reynolds number flows (typical turbulent flows). The airflow in the present study is relatively weak and does not have a high Reynolds number. Moreover, when reducing the pot draft condition, buoyancy will significantly influence the flow feature in the cavity. Therefore, it was decided to compare the two approaches (see Section 3.3), and the explicit calculation of flow feature close to the walls proved to be better than the use of wall functions.

A proper choice of turbulence model is required to achieve an adequate trade-off between accuracy and computational time. The airflow pattern in the cavity under the hoods shares many similarities with the induced airflow in enclosed environments (e.g., jet flow and impingement on a wall, recirculation and buoyancy-driven flow). In the last years, the k - ϵ family of turbulence models has been very popular for indoor environment and jet flow simulations, which share several similarities with the present problem. In particular, the renormalization group (RNG) k - ϵ model was found to be reliable and accurate for a wide variety of applications (e.g., Chen 1995; Isman et al. 2008; Sharif and Mothe 2009). Recently, the SST (shear stress transport) k - ω model has attracted more attention for solving flow problems similar to the present one. This model was developed by Menter (1994) to model separation flows around solid obstructions, and it can blend the robust and accurate formulation of the k - ω model in the near-wall region with the k - ϵ model in the far field through blending functions. Stamou et al. (2008) used the SST k - ω model in their CFD model to evaluate the thermal comfort conditions in the indoor stadium of the Galatsi Arena. Hofmann et al. (2007) simulated steady and pulsating impinging jets by using 13 widely used turbulence models, and the SST k - ω turbulence model with the transitional flow option captured properly the heat transfer and flow field patterns in the entire domain compared to experimental results. Recently, Hussain and Oosthuizen (2012a) developed a CFD model with the SST k - ω turbulence model to simulate the buoyancy-driven natural ventilation in a simple atrium building. A comprehensive review on the validation of turbulence models was reported in literature (Zhai et al. 2007; Zhang et al. 2007). They compared CFD simulations to experimental

results, and the best agreement was achieved with the RNG k- ϵ or the SST k- ω models. In cases with strong buoyancy forces and high-Reynolds number jet flow (as in the present problem), the SST k- ω model provided better results. Based on the literature survey we decided to use this mode as the turbulence model in present problem. The SST k- ω model adopts a high Reynolds number turbulence model (the standard k- ϵ model), except in the region near the walls where a low Reynolds number model (the k- ω model) is used. The wall-adjacent mesh recommended for applying this model is to create either a coarse ($y^+ \geq 30$) or refined ($y^+ \approx 1$) mesh in the near wall areas. However, a refined mesh is necessary if it is intended to resolve the viscosity-affected region. The detailed algorithm of the SST k- ω model will not be repeated here for the sake of conciseness, and is available in (Fluent 2012).

As for radiation heat transfer, since the gas in the cavity is essentially air, the gas is treated as a non-participating medium. The way in which radiation heat transfer between surfaces was considered is described in Section 3.2.3.

A commercial CFD software, ANSYS FLUENT 12.0/12.1, was used for solving the set of equations. The governing equations are discretized based on the finite volume formulation. Default criteria were used to declare that the convergence of a simulation was achieved (Fluent 2012). In order to reach convergence, different strategies were employed, such as starting simulations with smaller imposed pressure drop, reaching convergence, and continuing to increase gradually the pressure drop until the desired values be reached. In the end, the mass and energy imbalances (the ratio of the difference between the inflow and outflow to the total inflow) can be reduced to less than 10^{-6} and 10^{-2} , respectively. The mesh is created in GAMBIT 2.4 and consisted in prism control volumes in the boundary layer, and Tet/Hybrid control volumes in the core of the domain. As described later, mesh independence was thoroughly tested. A typical mesh contained over 2 million control volumes, considering that the mesh is refined enough to catch the main feature of the turbulent flow in the pot. Approximately 10 hours were required for performing one simulation using 4 cores of 2.67GHz.

3.2.3 Boundary conditions

This sub-section presents all the boundary conditions that were used in this study. The pressure at all gaps was set to the atmospheric pressure while that at the outlet was an adjustable negative pressure. The total ventilation rate can thus be varied by changing the driving inlet-to-outlet pressure difference. To simulate the release of CO₂ from the bath in the cavity under the hood, a small region that correspond to the feed hole on anode cover was considered from which hot gases (CO₂) are released at 700°C with a mass flow rate of 0.0048 kg/s for our simulated domain (based on 1.3% molar concentration of hot gas in effluents). Since the specific heat of CO₂ is very close to air and no species consideration is involved in the current simulations, we replaced the CO₂ properties with that of air for simplifying the model. The turbulence intensity was set at 1% at all inlets and outlet considering the low turbulent flow in the cavity. Turbulence length scale was defined as 7×10^{-4} m at the gap inlets, considering that the width of gaps is about 0.01 m, as recommended in (Fluent 2012). Hydraulic diameter was used to define the turbulence parameters at the exit outlet and hot gas inlet (Fluent 2012). Impermeability and no-slip flow are assumed on all solid surfaces. For all vertical surfaces facing other anode assemblies, symmetry was imposed.

According to the geometrical simplifications presented above, the thermal boundary condition on the bottom surface (i.e., top surface of anode cover) is represented by a uniform heat flux of 2000 W/m². This value is the average heat flux through the anode cover of a mix of crushed bath and alumina obtained from practical measurements in literature (Shen et al. 2008). The temperature at the small surfaces that correspond to the bottom of the stubs was fixed at 450°C based on Abbas's thesis (Abbas 2010). For the external surfaces of hoods and superstructure, the effective heat transfer coefficient for convection and radiation is fixed to 10 W/m²·K, which is typical for natural convection dominated heat transfer (Abbas 2010). The ambient potroom temperature in this work is set to 30°C and a heat flux of 800 W/m² is imposed on the top tip of anode rod. All boundary conditions used in the present study are presented in Table 3.1.

Table 3.1 Boundary conditions used in the present study.

Boundary Conditions	Values	Complements
q_{cover}	2000 W/m ²	Uniform heat flux into the domain
T_{am}	30°C	Ambient temperature
\bar{h}_{eff}	10 W/m ² ·K	Effective heat transfer coefficient from the external surface of the superstructure to the ambient
ΔP	5Pa-60Pa	Inlet-to-outlet pressure difference
$q''_{\text{tip of rod}}$	800 W/m ²	Approximate value, no significant effect
Radiative emissivity		
Anode cover	0.4	Measurements from (Rye et al. 1995) Oxidized rough metal surface, from (Perry et al. 1984)
Superstructure (internal)	0.8	
Rod	0.8	
Yoke and stubs	0.8	

The thermal conductivity and electrical resistivity of aluminum and steel are temperature dependent. Since the electrical field was not simulated in the CFD model, constant heat sources were defined to represent the joule heating in different components. Table 3.2 provides the detailed information.

Only surface-to-surface radiation heat exchange is involved in the CFD model because we ignored the effect of medium participated radiation. Discrete Ordinates (DO) Radiation Model (Fluent 2012) was chosen to simulate the radiation heat transfer between the surfaces of the cavity. The advantage of the DO model over other ways to consider surface-to-surface radiation heat transfer implemented in ANSYS FLUENT 12.0/12.1 is that it can be run in parallel. The surface emissivity of pot components is indicated in Table 3.1 and all surfaces corresponding to inlets and outlets are treated as blackbodies.

Table 3.2 Thermal conductivity and Joule heating source term for aluminum and steel.

Materials	Thermal conductivity (W/m·K) as a function of temperature, T (in °C)	Heat source due to Joule heating (W/m ³)
Aluminum	$202+0.168T-7.2 \times 10^{-5}T^2$	7500 (rod)
Steel	$50.82+9.6 \times 10^{-3}T-9.79 \times 10^{-5}T^2+6.28 \times 10^{-8}T^3$	16000 (yoke) 8300 (center stub) 4600 (side stubs)

3.3 Model verification

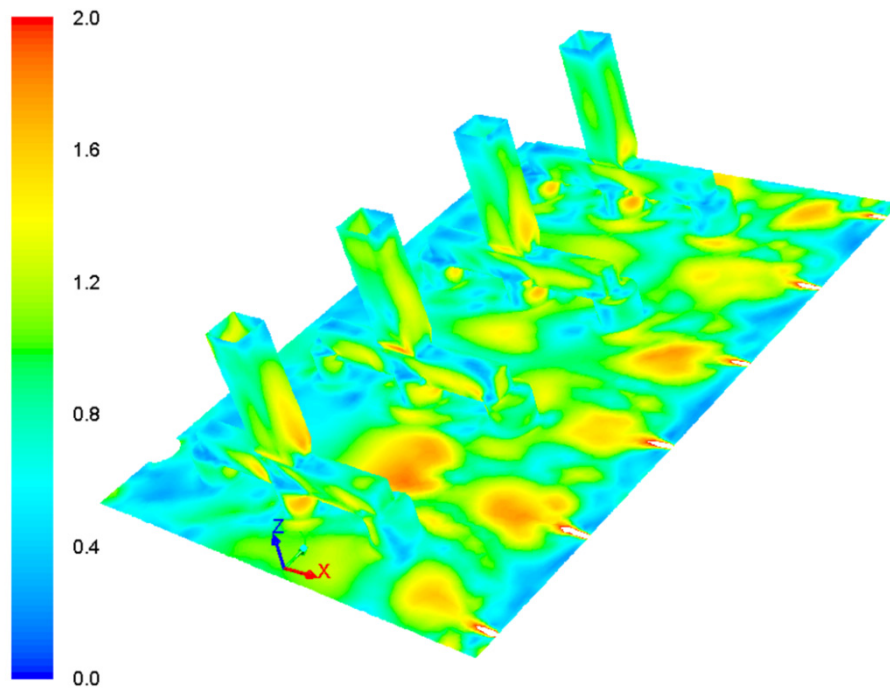
3.3.1 Verification of mesh requirements

The mesh used in this model was extensively tested to ensure mesh independence and to respect the turbulence model requirements of the near wall mesh in terms of y^+ . Three families of meshes were generated. For mesh #1, wall functions were used and therefore, the mesh includes only bulk control volumes with an initial maximal side length of 0.05 m, grown based on a surface mesh. The mesh near the gap and anode assembly was more refined than near the cover, hoods and superstructure. A boundary layer mesh is created in the regions near all walls in meshes #2 and #3 (near wall meshes). Mesh #2 adopts the same parameters as mesh #1 to build the mesh in the core of the cavity, while mesh #3 has a higher mesh density in the core with a maximal side length of the control volumes of 0.03 m. Normal draft condition and low draft condition (30% of normal condition) were tested. We defined the temperature and mass flow rate through the exit outlet as the monitoring parameters to compare among different meshes. After simulation, the value of y^+ on all surfaces was verified. The mesh was adapted until the value of y^+ is equal to ~ 1 in most area (Fig. 3.2) for meshes #2 and #3, i.e. until the mesh requirement of the SST $k-\omega$ model is well satisfied. It was found that the results did not change significantly when more than 6 layers of cells with a thickness of 0.8 mm were used for the boundary layer mesh. Therefore, only 6 layers were used in the final mesh. In normal draft condition, the relative difference of the exhaust gas temperature and mass flow rate at the outlet are less than 2% (i.e., $\sim 2^\circ\text{C}$ for temperature) between mesh #1 and mesh #2. In a

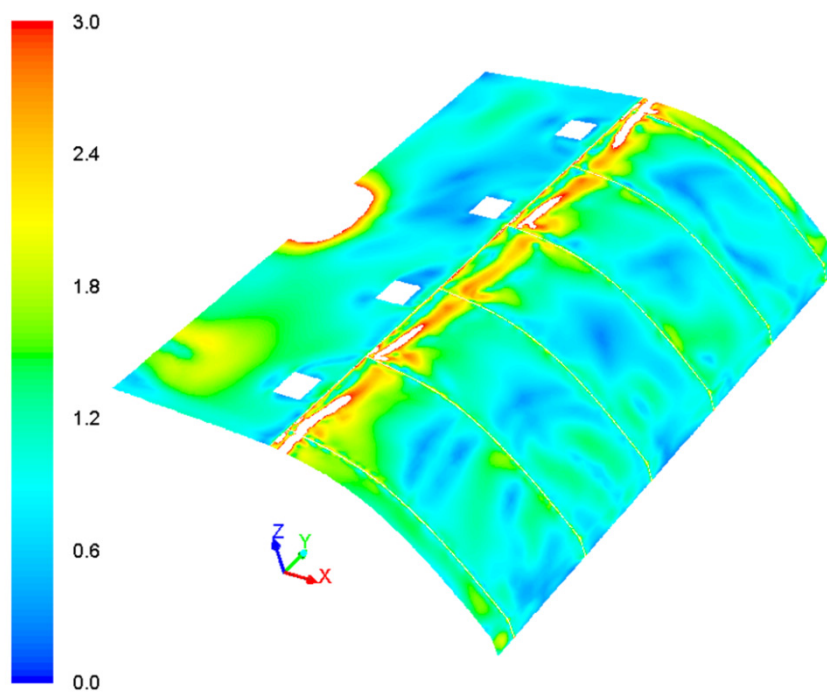
low ventilation rate, however, the relative difference reaches to 5% for temperature (i.e., ~9-10°C) and 6% for the mass flow rate. Between meshes #2 and #3, these values are less than 1% (i.e., 0.1°C in normal condition and 2°C in low draft condition) and 2% respectively for temperature and mass flow rate. In conclusion, the wall function mesh (mesh #1) is valid to predict the near wall flow feature under a normal ventilation rate, but it did not provide precise results with a low ventilation rate where the flow is significantly influenced by buoyancy forces. Therefore, the final retained mesh was mesh #2, and included around 2 million control volumes with typical side lengths of the control volumes ranging from 0.01 to 0.05 m.

3.3.2 Validation with literature

The simulation results can be compared with heat transfer measurements available in literature. Several types of smelting pots are used in the primary aluminum industry, and this constitutes a difficulty that should be taken into account when comparing results and measurements from different sources. Gadd et al. (2003) performed a series of measurements on the exhaust gas temperature versus the ventilation rate in aluminum reduction cells. We performed CFD simulations with variable draft conditions to compare with their data. The ambient temperature surrounding the cells has a direct influence on the final exhaust gas temperature. Here, we chose 30°C as the ambient temperature which is consistent with the ambient temperature during Gadd's measurements. Furthermore, a conversion should be made to achieve an equivalent ventilation rate per anode in both cases. For example, the normal draft condition in our case is 2.4 Nm³/s (Nm³=normal cubic meter) for 40 anodes in one pot while for Gadd's work, the normal condition was 1.44 Nm³/s for 24 anodes in one pot. Fig. 3.3a presents the CFD results and the measurements adapted from Gadd's work. Note that the draft condition indicated in Fig. 3.3a is the ventilation rate for one pot of 40 anodes and the simulated ventilation rate was calculated based on the air density at 273 K. A good agreement was found between present results and those of Gadd, and the maximal difference is about 10°C at half of the normal draft condition.



(a)



(b)

Figure 3.2 y^+ distribution (a) on the surfaces of anode cover and anode assembly; (b) on the internal surfaces of hoods and superstructure.

The temperature of different pot components was also compared with measurements and other simulations available in literature. Table 3.3 provides the range of the spatial distribution of the temperature of different components under normal conditions in our simulations and in data from other works. The comparison shows that the results are similar. Finally, the heat transfer coefficient on the top surface of anode cover was measured in some papers, ranging from 9 to 14 W/m²·K (Eggen et al. 1992) (Taylor 2007). The simulated coefficient is 13 W/m²·K under normal condition, which is in the above-mentioned range. Based on all the above verifications, the numerical model proves to be able to capture the important heat transfer and fluid flow features in the cavity.

Table 3.3 Comparison of the results of the present work with other results taken from literature.

Component	Results from current work	Data from literature	Comment
Anode cover (top surface)	180-310°C	175-320°C (Shen et al. 2008)	Mixture of crushed bath and alumina
Anode stubs and yoke	240-450°C	143-459°C (Abbas et al. 2009)	Measures from the stubs to the rod
Anode rod	180-240°C		
Hoods	120-165°C	100-146°C (Abbas et al. 2009)	

3.4 Comparison between CFD simulations and a thermal resistance circuit model

The heat transfer results of the CFD model described above were compared to the results provided by a home-made thermal resistance circuit (TRC) model that has been developed and validated in our lab to estimate the heat transfer rate in the upper section of a typical smelting pot, from the upper surface of the bath to the ambient in the

potroom. The TRC model is a convenient tool to facilitate the thermal management or the predesign of the upper part of smelting pots. Although the TRC model does not provide as detailed information as the CFD model, it has the practical advantage to run much faster (a few minutes, compared to several hours for the CFD model). The main reasons for comparing the CFD and TRC results are to evaluate their degree of coherence, and to assess their respective limits, advantages and drawbacks. Moreover, this serves as an additional way to verify the validity of the present model.

Before presenting the comparison, a short description of the TRC model is firstly presented. In the TRC model, the main surfaces are represented by nodes for which the average temperatures must be determined. Two coupled sub-networks have been built, one with the conductive and convective thermal resistances between the nodes, the other sub-network representing the radiative heat exchange between the different surfaces. Joule heating in the anode assembly was taken into account. The thermal circuit described above was solved in Matlab. An energy balance was performed at all temperature nodes of the network. The resulting set of equations was written in a matrix form. Bath and potroom temperatures were imposed (boundary conditions). Due to non-linear physics (e.g., properties that depend on temperature, radiation), an iterative solution procedure needed to be implemented. Starting from an initial guess for the temperature at each node, the matrix components were computed. Then, the matrix system was solved. The matrix components were updated based on the new values of temperature, and so on. The procedure is repeated until temperature convergence. Given the driving temperature difference between the bath and the potroom air, the network allows determining how and where heat is lost via the upper part of the cell

The CFD simulation results were compared with those obtained from the TRC model, as shown in Figs. 3.3 and 3.4. The exhaust gas temperature from both methods was compared under different ventilation conditions in Fig. 3.3a. The agreement could be qualified of very good, with just a few degrees of difference. Average surface temperatures were also compared (Fig. 3.3b, 3.3c, and 3.3d). The difference in surface temperature between the two models is very small in most draft conditions and the maximal difference is less than 10°C. This maximal temperature discrepancy is achieved

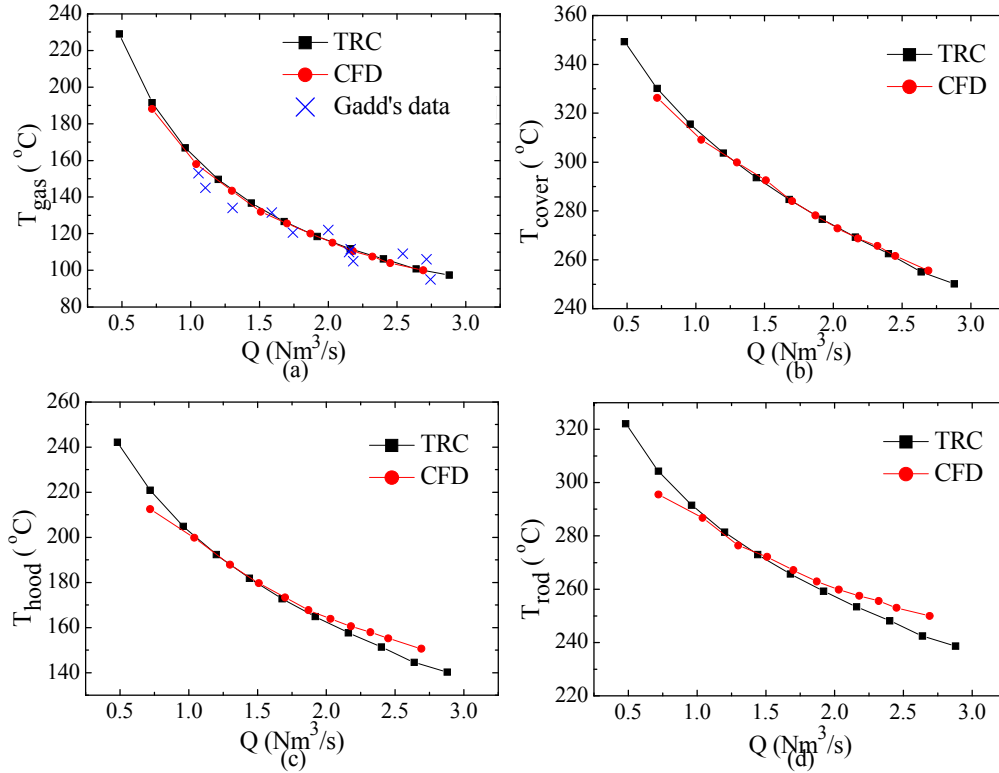


Figure 3.3 Comparison between average temperatures obtained from the CFD model and from the thermal resistance circuit (TRC) model, as a function of the ventilation, for: (a) the exhaust gas (including Gadd's experiments); (b) the top surface of the anode cover; (c) the surfaces of hoods and superstructure; and (d) the base of aluminum rod.

at the base of the aluminum rod under normal and higher draft conditions in Fig. 3.3d. This discrepancy is likely caused by the simplifications of the anode assembly to 1D component in the TRC model. The TRC tends to underestimate the rod temperature compared to the CFD model. However, the influence of this discrepancy on the overall heat transfer in the system is weak.

Reported in Fig. 3.4a is the heat content in the exhaust gas. Results from both models are coherent and the maximal difference is just of the order of 250 W (relative difference of 5%). Besides, the radiation heat transfer rates on surfaces as achieved by the two models were compared in Figs. 3.4b, 3.4c and 3.4d. A good agreement was found on the top surface of anode cover in Fig. 3.4b (maximal difference of ~100 W and relative

difference of 10%). On the surface of the superstructure and hoods, Fig. 3.4c, a similar trend is found with both models, but discrepancies become more important as the ventilation rate goes down (around 10% of discrepancy). The relatively large error is due to the geometrical simplification of the surfaces in the TRC model for calculating radiation. In reality, there is a large non-uniformity of surface temperature on the hoods and superstructure. CFD has shown its capacity of predicting the temperature spatial variation while it is obviously not the advantage of the TRC model. This non-uniform temperature distribution will result in an error in calculating the energy irradiated from the surface. Fig. 3.4d shows the radiative heat transfer rate from the surfaces of yoke and stubs, where high temperatures prevail. Both models provide heat transfer rates of the same order of magnitude (around 2 kW). Nevertheless the radiative heat transfer rate was almost the same in CFD simulations for all draft conditions, whereas it increases with the reduction of ventilation rate in TRC calculations. The difference in terms of trends is due to the approximate boundary condition defined at the bottom of the three stubs in the CFD model. As mentioned previously, a fixed temperature of 450°C on the bottom of the stubs was assumed in the CFD model, which might not represent well the stub temperature under low ventilation level. For example, it was shown that this temperature increases up to 500°C at low draft condition (based on the calculation of TRC model). The fact that the yoke and stubs temperature is smaller in the CFD model will tend to underestimate radiative heat transfer from these components. This problem could be solved in future work by extending the computational domain of the CFD model to the bath itself where a constant operating temperature can be assumed at all time.

In conclusion, the TRC temperature predictions are quite coherent with the CFD simulations in most areas of the top section of an aluminum smelting pot. Considering the most interesting parameters, i.e. the exhaust gas temperature and the heat content in the gas, TRC calculations can provide a good agreement with CFD simulations. It is worth to mention that the convection heat transfer coefficients in the TRC were based on the CFD simulations (see next section). Therefore, knowing that this aspect was consistent between the two models, it is worth to verify that the rest of the two modeling approaches provide coherent (i.e., similar) results. As exemplified below, the CFD model provides a

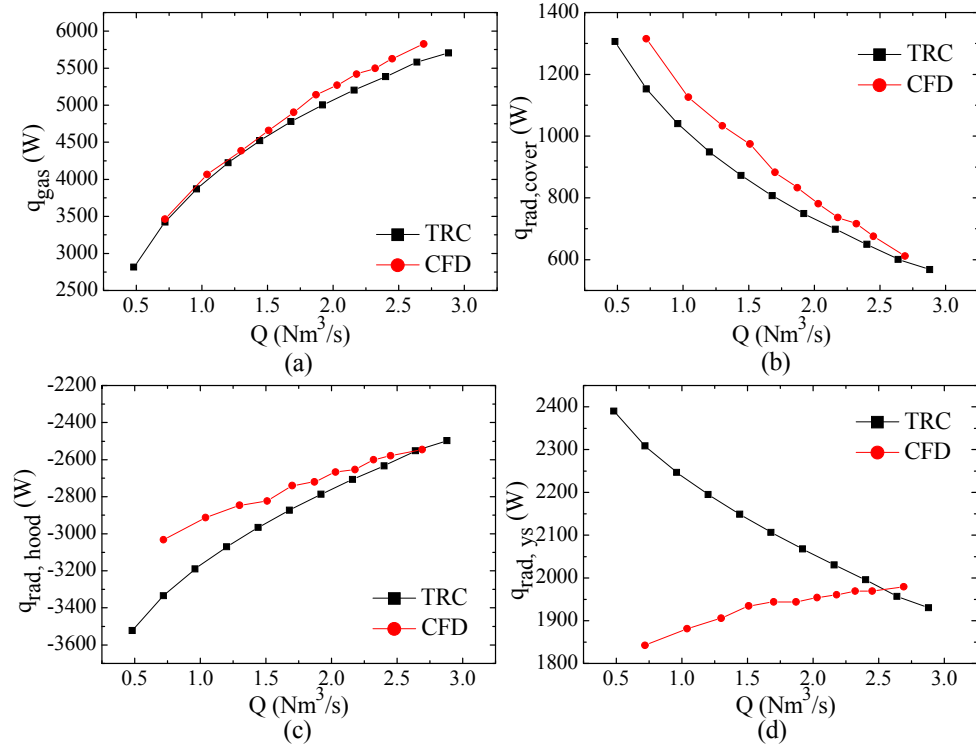


Figure 3.4 Comparison between heat transfer rates obtained from the CFD model and from the thermal resistance circuit (TRC) model, as a function of the ventilation, for: (a) heat content in exhaust gas; (b) radiation heat transfer from the top surface of the anode cover; (c) radiation heat transfer on the surfaces of hoods and superstructure; and (d) radiation heat transfer from the surfaces of yoke and stubs (y,s).

much more detailed information. However, the TRC model is much simpler and can provide acceptable results in terms of precision. It is not necessary to run CFD simulations, since from the moment one knows appropriate correlations to determine heat transfer coefficients (or at least, their orders of magnitude), the correlations can be used straightforwardly in the TRC model.

3.5 Correlations for average convection coefficients

One of the objectives of the present work is to develop correlations for the convection coefficients within the upper part of a smelter. These correlations could be used in place of correlations for flow on flat plates or around cylinders which do not represent well the

present geometry. In particular, we envisioned the use of these correlations in simplified models such as the thermal resistance network mentioned in section 3.4. In this thermal network, four expressions of average convective coefficients are required between the air under the hoods and the surfaces of (i) anode cover, (ii) hoods, (iii) anode rod, and (iv) anode yoke and stubs. The correlations between the average convection coefficient and the total air mass flow rate are established for all these four surfaces. These parameters are dependent of the draft condition and to some extent, of the geometry of the cavity. We used the area-weight average integral method to calculate the average convection heat transfer coefficient, expressed as

$$\bar{h}_{\text{conv}} = \frac{1}{A} \sum_{i=1}^n \left(\frac{q'' - q''_{\text{rad}}}{T_i - T_g} A_i \right) \quad (3.5)$$

where q'' and q''_{rad} are the total and radiative heat flux going through the i^{th} wall cell, A , the area of the surface, and A_i , the area of the i^{th} wall cell. T_i and T_g are the i^{th} wall cell temperature and the average temperature of the gas in the cavity, respectively. The convection heat transfer rate can be obtained by subtracting the radiation heat transfer rate from the total heat transfer rate on the surface considered. The surface temperature is available directly from the simulation results. Based on the principle of energy conservation, an average air temperature in the cavity is calculated as

$$T_g = \frac{\sum_{i=1}^n C_{p,i} \rho_i V_i (T_i - T_{\text{am}})}{\sum_{i=1}^n C_{p,i} \rho_i V_i} + T_{\text{am}} \quad (3.6)$$

where the summation is over all n control volumes. T_{am} is the ambient temperature, $C_{p,i}$, ρ_i , and V_i are the specific heat, density and volume of the i^{th} control volume.

The coefficients \bar{h}_{conv} on the four surfaces of interest under different draft conditions are presented in Fig. 3.5 (a-d). The flow rate on the x-axis represents the volumetric air flow rate for one pot of 40 anodes, although the simulated domain is only associated with a portion of the cell containing 4 anodes. The four curves show a nearly linear trend with the increasing mass flow rate except for the convection coefficients on the hoods surface at low mass flow rates. The nearly linear relationship between the surface convective coefficients and the mass flow rate can be, to some extent, explained

by some conventional correlations established. For example, for a turbulent flow over a flat plate, the Nusselt number (i.e., the heat transfer coefficient) is proportional to the Reynolds number (i.e., to the velocity) to power 0.8 (Bergman et al. 2011). When the range of Reynolds number under investigation is not too large (as in the present study), the function actually appears nearly linear. The same comment can be made for a turbulent cross flow around an infinite cylinder, for which the Nusselt number is proportional to the Reynolds number to power 0.7 or 0.8, depending on the correlation chosen (Bergman et al. 2011). Another interesting phenomenon found in Fig. 3.5 is that the values of all convection coefficients assume similar values, from 7 W/m²·K to 11 W/m²·K, except for that on anode rod. When the draft increases, all convective coefficients are increased with nearly the same rate.

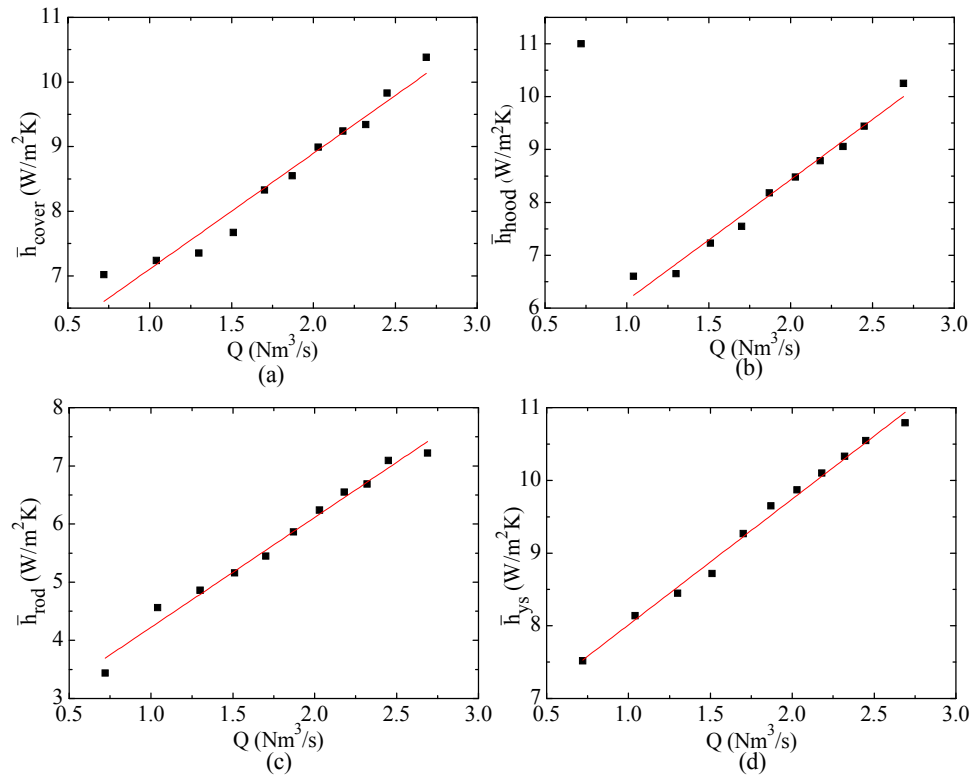


Figure 3.5 Average convection coefficients (solid symbols) and correlations (red lines) with variable draft conditions, (a) on the top surface of anode cover, (b) on the surface of hoods and superstructure, (c) on the surface of rod, (d) on the surface of yoke and stubs.

Four correlations of the average convective coefficient versus the mass flow rate were thus established for all the considered surfaces, assuming a linear relationship between the convective coefficient and the ventilation rate, see Table 3.4. The average error between the data points and the correlations are very small, between 0.8 and 2% depending on the surface considered. These correlations could be effectively applied in the pot draft condition from 1.0 to 2.8 Nm³/s, based on the results in Fig. 3.5.

In Fig. 3.5b (hoods), we found one outsider point at low mass flow rate that seriously deviates from the trend of the other points. This is because in such low draft conditions, the average temperature of the gas in the cavity is increased close to that of the hood. The average effluents temperature at the outlet is about 188°C while the average hood temperature is around 195°C. When checking the local convection coefficient on hoods, some areas displayed a large value (1600 W/m²·K). This unreasonable convection coefficient indicates that the local wall temperature is very close to the average gas temperature. In this case (i.e., $T_{\text{cell}} \rightarrow T_g$), when using Eq. (3.5) to calculate the local convection coefficient, the calculation of \bar{h} involves the division of a small number ($q'' - q''_{\text{rad}}$) by a very small driving temperature difference. Thus, the calculation of \bar{h} will be strongly affected by the numerical error since it involved very small convection heat transfer rates and temperature difference. Therefore, the value of \bar{h}

Table 3.4 Correlations for average convection coefficients on four surfaces of the cavity, as a function of volumetric flow rate Q for one pot [Nm³/s] and the average and maximum relative error between correlations and CFD results.

Surface	Correlations	Average error, %	Max. error, %
Anode cover	$\bar{h}_c = 5.32 + 1.79Q$	2	6.2
Hoods, superstructure	$\bar{h}_h = 3.87 + 2.28Q$	1.7	5.7
Rod	$\bar{h}_r = 2.33 + 1.89Q$	1.7	6.7
Yoke and stubs	$\bar{h}_{ys} = 6.28 + 1.73Q$	0.8	1.9

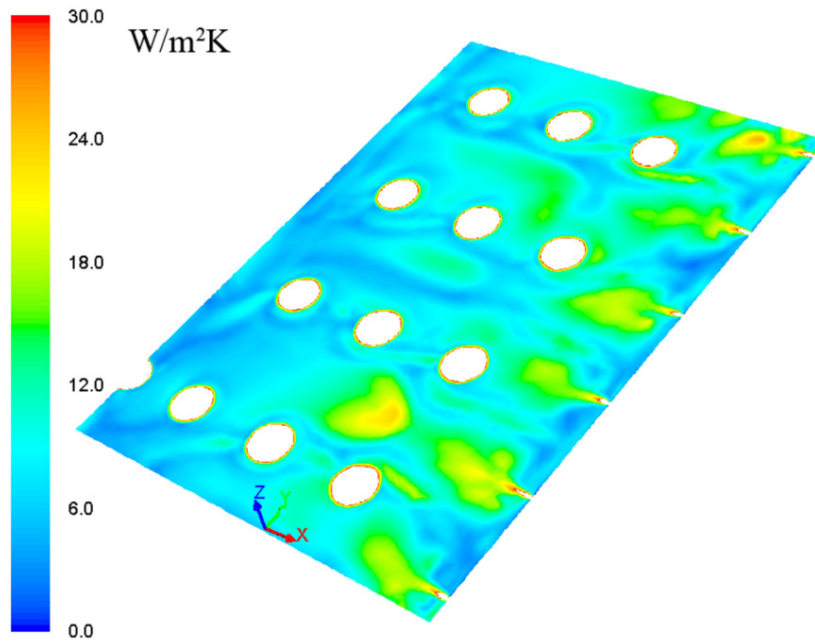
for the abnormal point in Fig. 3.5b was disregarded in developing the correlation for the hood surface in Table 3.4. In any case, it is worth to mention that the exact value of \bar{h} on the hood under these conditions has little effect on the energy balance since the driving temperature difference is almost zero, and so is the convective heat transfer rate.

In general, larger relative errors (~6-7%) between the correlation and the data point were observed at low draft conditions for all surfaces. This phenomenon indicates that the linear correlation will fail to predict the convection coefficient at a very low ventilation rate (<30% of normal draft condition), where buoyancy effect becomes dominant. However, extremely low ventilation rates are not investigated in present work since they would involve serious engineering problems, i.e. hazardous gas leakage due to small vacuum in cavity, significant reduction of the top heat loss and over-heating problem in pot components.

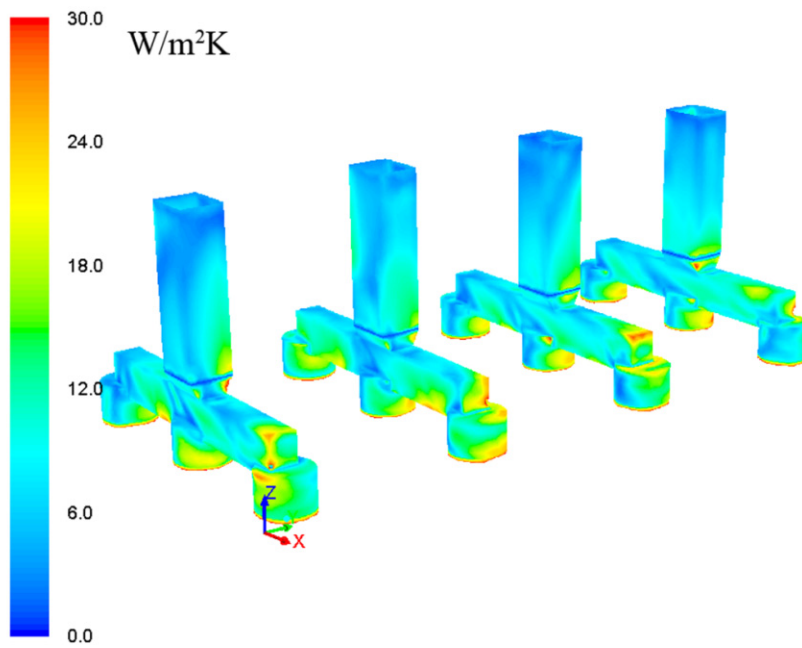
3.6 Spatial variations of the local convection coefficients

Although average convection coefficients are reported in Table 3.4 and Fig. 3.5 for the surfaces of interest, it should be noted that the convection coefficient is actually non-uniform on these surfaces. In order to achieve a better thermal management of the pots, it is instructive to have a deeper insight into how the local convection coefficient varies with position. In the present section, more information on the local convection coefficient on the anode cover and on the anode assembly is presented. The reason for focussing on these two surfaces is that the calculation of TRC model has demonstrated that the heat transfer coefficient on these two components had the greatest influence on the exhaust gas temperature and heat content.

Figure 3.6a shows the convection coefficient distribution, under normal draft conditions, on the top of anode cover, which ranges from 2 W/m²·K to 28 W/m²·K. The average value reported in the previous section is 13 W/m²·K. The areas with large heat transfer coefficients are located close to the fresh air inlets (i.e., hood gaps), extending up to the first stub of each yoke (side-channel, i.e. region on the anode cover between the hood and the anode assembly). In these areas, the convection coefficient is twice as large



(a)



(b)

Figure 3.6 (a) Local convection coefficient h_{cover} ($\text{W}/\text{m}^2\cdot\text{K}$) on the top of anode cover in normal draft condition; (b) local convection coefficient h_{ys} ($\text{W}/\text{m}^2\cdot\text{K}$) on the surface of the anode assembly in normal draft condition.

as the average value on the anode cover. The gaps between hoods create jets of cold air into the cavity. An intense heat exchange occurs in the side-channels of the smelter because of the relatively high velocity of the jet and of a large temperature difference between the cold air and the anode cover surface. Then, the anode assemblies act as obstacles to the flow, and reduce flow velocity along with momentum diffusion. The smallest values of the local convective coefficient were found in the internal channel (the middle area of the pots) and in the vicinity of the bottom edge of the hoods.

Another important surface is that of the anode assembly, which is shown in Fig. 3.6b. The range of local convection coefficient is similar to that observed on the anode cover, with values up to $30 \text{ W/m}^2\cdot\text{K}$ (the same scale as in Fig. 3.6a is used in Fig. 3.6b for the sake of comparison). It is seen that the convection coefficient is generally higher on yoke and stubs than on rods. The most efficient convective areas are all located at the surfaces that face the upstream flow.

3.7 Forced versus natural convection

When modeling a system such as the one considered in the present study, one of the initial questions that arises is which of natural or forced convection dominates. As described in the previous section, it was decided to include buoyancy forces in the model. Nevertheless, we wanted to quantify the importance of these forces on the overall heat transfer in the cavity. Developing this understanding is important in order to eventually propose design modifications either to enhance or block heat transfer in the top section of electrolytic cells.

In engineering applications, one often compares the role of natural and forced convection by looking at the ratio of the Grashof number to the square of the Reynolds number, Gr/Re^2 , which is sometimes called the Richardson number. When the ratio is much smaller than 1, natural convection is negligible. Unfortunately, such an approach proved to be hardly feasible here since the fluid flow and heat transfer patterns are quite complex, and far from that a parallel flow over a flat plate. Therefore, it was decided to evaluate the influence of natural convection by performing additional simulations in which the gravitational force would be disregarded (i.e., in the sole presence of forced convection), and then to compare the results with that achieved in the presence of gravity.

Using the same procedure as previously, we calculated the average convection coefficients on all studied surfaces, and reported them in Fig. 3.7 (a-d).

First, we note that the convection coefficients are typically smaller when gravity forces are disregarded. This means that buoyancy forces work to enhance the heat transfer coefficient. For example, the anode cover temperature is much larger than that of the air in the cavity, and thus, the cover is a “hot surface facing up”, which will boost the heat transfer coefficient when gravity forces are accounted for (Jacobs 1987). A similar observation can be made for the other surfaces, except for the hood. Since the hood is a “warm surface facing down”, the flow pattern generated by buoyancy forces is weak since the density pattern is more stable.

When the mass flow rate is reduced, the role of natural convection becomes more important. This is caused by reduced jet flows (i.e., low value of Re) from the gaps between hoods in these conditions, and also by the fact that the temperature of all surfaces will go up which will tend to promote buoyancy forces. In Fig. 3.7(a-d), the discrepancy between purely forced and mixed convection coefficients is increased as the pot draft condition is reduced and the forced convection coefficients on the surfaces of anode cover and yoke and stubs only have approximately half of the value of the mixed convection coefficients under low draft conditions. This means that natural convection accounts for roughly half of the convective heat transfer on these surfaces in low draft conditions, but nevertheless forced convection cannot be neglected. In other words, the low draft condition is truly a mixed convection situation.

On the other hand, under normal and high ventilation rate, the role of buoyancy forces is weaker. The difference in heat transfer coefficients (under normal ventilation) with and without gravity forces is relatively small, less than 5% for the hoods and rods, less than 10% for the yoke and stubs, and less than 20% for the anode cover surface.

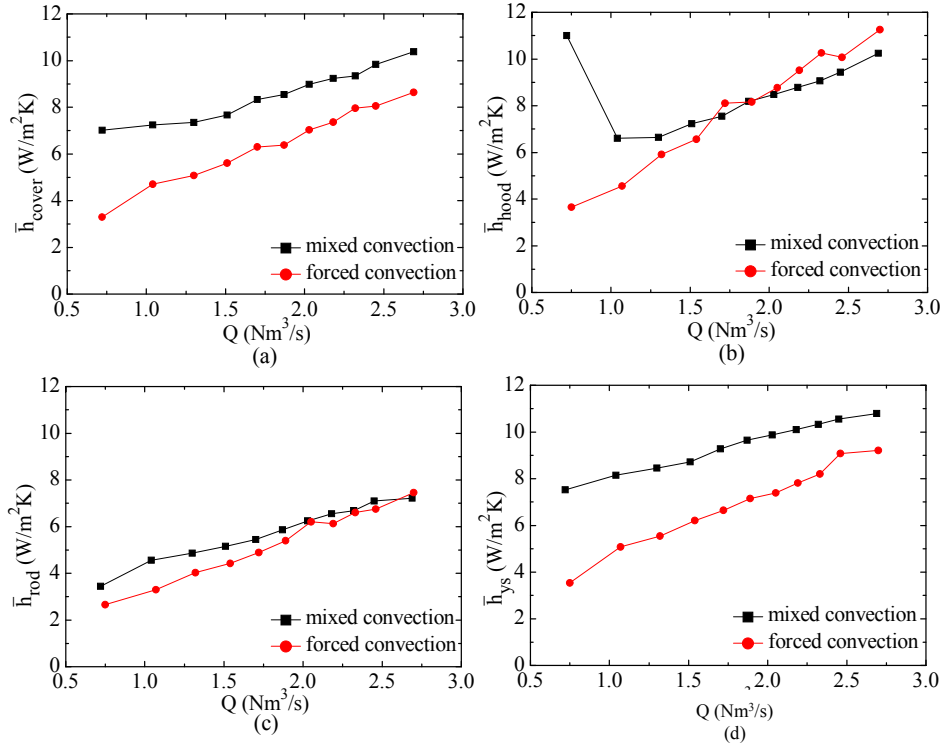


Figure 3.7 Average forced and mixed convection coefficients with variable draft conditions, (a) average convection coefficients on the top surface of anode cover, (b) average convection coefficients on the surface of hoods and superstructure, (c) average convection coefficients on the surface of rod, (d) average convection coefficients on the surface of yoke and stubs.

3.8 Pressure drop-flow rate relationship

The pressure drop in the cavity is another important result of the CFD simulations. In industry, engineers are interested in the negative pressure within the cavity at all time during production. This negative pressure is required to keep a certain level of vacuum in the cavity to prevent hazardous gases from leaking out of the pot. Furthermore, the pressure drop caused by the pots influences the fan power and duct network required to collect the effluents from the cells. One possible way to enhance the quality of the effluents from a waste heat recovery perspective is to reduce the ventilation rate of the pot. This can also result in significant reduction of the fan power requirement. For example, a 50% reduction on the ventilation rate could reduce the requirement of fan power to approximately 1/8th of the normal level (since $W \sim Q^3$). In fact, fan power can

represent a few percents (~2-4%) of the total electricity input to a primary aluminum smelter. Therefore, it is useful to develop more knowledge on the pressure drop-flow rate relationship of electrolytic cells.

The pressure drop is affected by many factors, e.g., the pot tightness, the pot structure, the ventilation rate and the operations of anode change and aluminum tapping. Few reports are available in open literature on this topic. In this work, the pot geometry was fixed, and only the mass flow rate (or equivalently the overall pressure drop) was changed. Fig. 3.8 reports the inlet-to-outlet pressure drop in the cavity as a function of the flow rate. As mentioned previously, in the present simulations the inlet-to-outlet pressure drop was fixed (boundary conditions), and the flow rate was calculated based on the simulation results. The pressure drop versus flow rate relation is almost parabolic for the range of parameters investigated. A proper correlation is proposed as:

$$\Delta p = 8.41Q^2 \quad (3.7)$$

where Δp (in Pa) is the inlet-to-outlet pressure drop, and Q (in Nm^3/s), the volumetric flow rate for one pot. The average relative error between the correlation and the data points is 3.4%. The maximal deviation between the data points and the correlation is 14% and occurs at the lowest simulated flow rate condition.

From Fig. 3.8, we found that cutting the current ventilation rate by 2 (i.e. going from 2.4 to 1.2 Nm^3/s) yields a significant reduction of the pressure drop. The gap-to-outlet pressure drop reduces from 45 to 15 Pa. Further reduction in the draft changes only slightly the negative pressure in the cavity. In practice, there is a minimal level of vacuum that is required in order to prevent fugitive emissions into the potroom. For example, Karlson et al. (1998) reported that a minimal vacuum of 3.9 Pa is required between the internal vicinity of gaps and the potroom. According to this suggested threshold, the ventilation rate can only be reduced to approximately 60% of the normal draft (i.e., to 1.4 Nm^3/s). Below this value, exfiltrations into the potroom would be considered too risky. Note that the Karlson threshold is not universal and can vary according to pot design and tightness. In terms of waste heat recovery, this constraint represents a limitation on the possibilities to enhance the energy grade of the exhaust gas. Another way to do this would be to increase the tightness while maintaining the same internal pressure. However, this possibility was not studied in the present work.

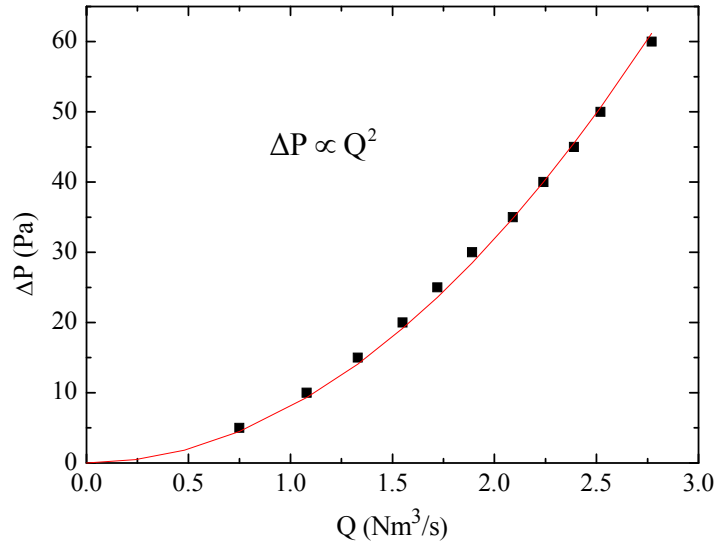


Figure 3.8 Inlet-to-outlet pressure drop (solid symbols) and correlation (red line) versus draft condition.

3.9 Conclusions

In this chapter, we presented a CFD model of the upper part of an aluminum smelting pot. The model was employed to study the heat transfer mechanisms in that domain. A comparison with the thermal circuit model showed that both models yielded coherent results in terms of temperatures and heat transfer rates. The TRC model has the advantage that is much simpler and faster to use, whereas the CFD model provides more detailed information.

We have been able to develop new correlations with the CFD model in order to determine the average convection coefficient on specific surfaces, under different draft conditions. These correlations are used in our TRC model. The non-uniformity of the heat transfer coefficient was also revealed by the CFD model, with some surface areas exhibiting a high heat transfer density and others, a smaller. The relative importance of natural convection versus forced convection was also studied. We showed that natural convection works to enhance the heat transfer coefficients most of the times, and that under normal ventilation rates, most of the heat transfer is due to forced convection,

whereas under reduced draft, both natural and forced convections are equally important. Finally, a quadratic pressure drop versus mass flow rate correlation gives a good fit to the pot CFD results. All the above knowledge can be used in order to analyze current pot designs and guide future pot developments.

**CHAPTER 4 REDUCED VENTILATION OF UPPER PART OF ALUMINUM
SMELTING POT: POTENTIAL BENEFITS, DRAWBACKS,
AND DESIGN MODIFICATIONS**

Abstract

Maintaining current draft conditions in the upper part of Al smelting cell requires important electricity consumption for the fans. A reduction of the ventilation rate could significantly diminish the total power requirement at the blowers. However, adverse changes in operating conditions due to this ventilation reduction may disrupt the pot thermal equilibrium. A CFD model was created to investigate the influence of ventilation reduction on pot thermal balance. With the objective of maintaining normal heat losses by the top of the cell, several modifications are simulated, such as using plate fins on the anode assembly, changing hood gap geometry and modifying anode cover thickness. Heat transfer rates are determined for these modified designs, and compared to those currently achieved.

Résumé

Maintenir les conditions de ventilation actuelle dans la partie supérieure des cuves d'électrolyse requiert une grande quantité d'électricité pour actionner les ventilateurs. Réduire le taux de ventilation pourrait significativement réduire la consommation des ventilateurs. Par contre, des impacts négatifs sur les conditions d'opération pourraient résulter d'une réduction du taux de ventilation. Un modèle CFD a été créé pour étudier l'impact de la réduction de ventilation sur les cuves. L'objectif est de maintenir le même taux de dissipation thermique par le dessus des cuves. Des modifications sont proposées à cet effet, telles que l'ajout d'ailettes sur l'assemblage anodique, des changements dans la géométrie des gaps entre les capots et sur l'épaisseur de la couverture anodique. Les taux de transfert thermique ont été déterminés pour chaque nouveau design et comparé à la situation actuelle.

4.1 Introduction

Today's aluminum reduction technology is based on the Hall-Héroult process, which requires intensive energy input. Typically, ~13-15 MWh are required for producing 1 ton of Al, and roughly half of the energy input is lost from pots as waste heat. Due to the extensive amount of heat lost in the Al production industry, waste heat recovery has become a much researched topic in recent years. The "simplest" way to capture waste heat is from the pot exhaust gas which contains ~35%-40% of the heat lost by pots. Sørhuus and Wedde (2009) presents the design of a heat exchanger (HEX) for cooling the collected pot gases and thus recovering heat from them. Fouling on the HEX surfaces was analyzed and it was found that an annual cleaning was sufficient to maintain a proper heat transfer in the HEX even though the pot exhaust is largely contaminated with fouling agents. Fler et al. (2010) paid attention to the particle characteristics in the effluent, exhaust gas properties, and fouling propensity in the gas stream in front of the dry scrubber. The aforementioned works are mainly focused on current pot effluents, which are at a relatively low temperature (~100-130°C). Such low energy grade limits the potential usage of the waste heat.

Several theoretical and experimental studies have shown that the cell ventilation condition has the most influence on the pot exhaust temperature and heat content. Based on reported measurements in Gadd's thesis (Gadd 2003), the exhaust temperature could increase by 50°C when cell draft is reduced to 40% of the normal condition. Abbas et al. (2009) has determined the top heat losses in different draft conditions (i.e., from 3% to 160% of normal draft conditions) based on CFD simulations. This work shows that the pot effluents temperature can increase by over 100°C as the draft condition decreases to 20% of normal conditions. This work also proposes some geometrical modifications of the smelting pot to enhance the thermal quality of the pot gases (Abbas 2010). Lorentsen et al. (2009) reported that Hydro (Norway) has developed a gas suction technology that collects the CO₂ close to the feed hole, yielding a warmer and more concentrated flue gas, with less fan power required. An increase of temperature means an enhancement of the thermal quality of the waste heat, while an increase of CO₂ concentration is desirable in view of CO₂ capture processes. Moreover, reducing the cell ventilation rate can reduce drastically the fan power requirement, since it is typically proportional to the flow rate to

power 3 ($P_{\text{fan}} \sim Q^3$). For the sake of illustration, let us consider the fan energy consumption at a typical modern plant producing $\sim 260,000$ ton/y of Al. Two fans work to transport the flue gases to the gas treatment center, each with a power of 8467 kW, for a total annual electricity consumption as high as 148.3 GWh. Assuming 0.05 US\$/kWh, the annual cost of electricity for fans would be 7.4 MUS\$. If one can reduce the ventilation rate by half, the fan power can be roughly reduced to 1/8th of the normal consumption.

However, reducing pot ventilation may disturb current operating conditions. For instance, reduced ventilation means that less heat is extracted through the top section of the smelting pot (Abbas et al. 2009; Zhao et al. 2013a), and therefore, more heat has to be dissipated via sidewalls which could melt the frozen electrolyte and jeopardize pot integrity. Another aspect to be considered is the fume emissions from the pots to the potroom. A certain level of negative pressure should be maintained in the pots to prevent emissions to potroom.

In this work, we studied the heat transfer impacts of ventilation reduction in an Al smelting pot with CFD simulations. The model is based on actual pot design and operation. Different modifications are studied to overcome the adverse changes due to ventilation reduction. The objective of this work is to compare different scenarios in order to reduce the ventilation to a minimum level while maintaining current thermal equilibrium in the bath.

4.2 CFD Model

4.2.1 Simplifying Assumptions

The domain of interest is the upper section of an aluminum reduction cell, above the electrolytic bath. Several assumptions are made to reduce the computational burden:

- (i) A typical 350kA aluminum cell contains 40 anodes, divided in two parallel rows. By imposing a negative pressure at exit, air in the potroom enters the domain through gaps between hoods, around anode rods and other superstructure openings, and dilutes the CO₂ released by the Hall-Héroult process. The effluents are collected in a duct through 5 inlets located equidistantly on the bottom of the superstructure. Neglecting side effects and considering that the heat transfer and

flow pattern is the same below each of the 5 inlets, only the domain above two anodes needs to be simulated, as shown in Fig. 4.1. Such a unit consists of two anodes, 1/4 feed hole, 1/4 duct inlet, and the corresponding anode cover, superstructure and hoods. The flow pattern is periodic in the direction of the anodes row. This allows simulating only 1/20th of a pot.

- (ii) The bottom boundaries of the simulated domain are the immersed part of the anodic blocks and the bottom surface of crust. The CO₂ layer due to the accumulation of the hot gas emissions from the bath is not included. Here, we estimated the mass flow rate of the hot gas and imposed it as a mass inflow to the domain at the feed hole.
- (iii) A typical new anode has a height of ~0.6 m, and it is consumed to ~0.15 m before removal from the pot. The heat transfer rate through an anode varies strongly during anode consumption. However, since each pot contains 40 anodes at different levels of consumption, an average height of 0.4 m was assumed for the anodic blocks.
- (iv) A part of the potroom and upper cavity neighboring to the superstructure and hoods was included in the domain with an extended length of 0.5 m. The infiltration of air in the cavity under hoods comes from the gaps between hoods.

Other very narrow gaps were ignored in the model. The gap width is 1 cm.

The simulation domain is different from the model presented in chapter 3, because the purpose of the CFD model right now is to find the influence of different geometrical modifications on the top heat loss. The model was extended downward to include the anodes and anode cover, and the prediction error of heat transfer in the pot cavity under hoods due to the assumed boundary conditions at bottom can be attenuated. New boundary conditions were defined at the bottom of the anodes and anode cover to represent the heat exchange with the bath.

4.2.2 Governing Equations

The governing equations are those expressing the conservation of mass, momentum in each direction, energy, and electrical charge. Reynolds-Averaged Navier-Stokes (RANS) equations are applied to simulate the turbulent flow. Incompressible fluid flow and

steady-state conditions are considered. Pressure work and kinetic energy terms are neglected in the energy equation. Viscous heating is also ignored. Note that in the solids, only the energy and electrical charge equations are solved. All properties were assumed to vary with temperature and the equations are available in the Ansys Fluent documentation (Fluent 2012). As for heat transfer by radiation, the gas is treated as a non-participating medium. Only surface-to-surface radiation heat exchange is involved in the CFD, and is calculated with the Discrete Ordinates (DO) Radiation Model (Fluent 2012), which can be run in parallel. All surfaces corresponding to inlets and outlets are treated as blackbodies.

4.2.3 Turbulence Model

The RANS equations need a turbulence model to calculate the Reynolds stresses term. A proper choice of turbulence model is required to achieve an adequate tradeoff between accuracy and computational time. The airflow pattern in the cavity under the hoods shares many similarities with the induced airflow in enclosed environments (e.g., jet flow

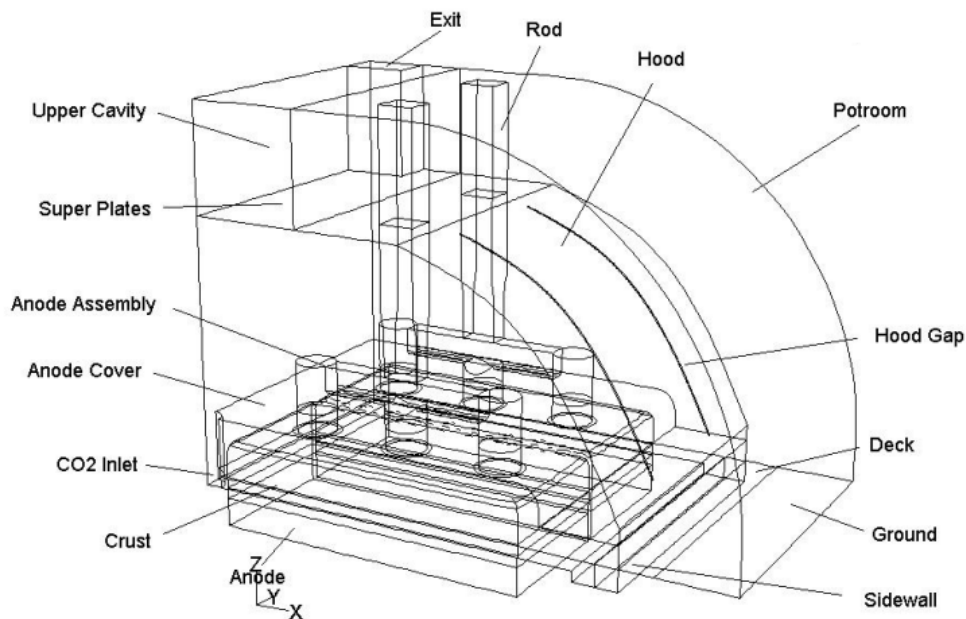


Figure 4.1 Schematic view of the domain of the CFD model.

and impingement on a wall, and buoyancy-driven flow). Before 2005, the k - ϵ family of turbulence models was very popular in indoor environment simulation and a general conclusion is that overall the RNG k - ϵ model provides the best performance. Recently, the k - ω turbulence models have attracted more attention in industrial applications. A comprehensive review on validation of turbulence models was reported in literature (Zhai et al. 2007; Zhang et al. 2007). They compared CFD simulations to experimental results. The RNG k - ϵ and SST k - ω have shown the best performance. In cases with strong natural convection and high-Reynolds number jet flow, the SST k - ω model provided better results. In the present problem, airflow at potroom temperature is induced into the cavity under hoods where the wall temperature can reach 200-300°C. Strong natural convection thus occurs between the walls and the airflow in the cavity (Zhao et al. 2013) and for this reason the SST k - ω model was chosen.

4.2.4 Numerical Modeling and Mesh

The equations of the present model were solved with a CFD commercial software that relies on the finite volume approach (Fluent 2012). Meshing of the domain was built so as to respect the requirements of the turbulence model. The SST k - ω model in the CFD software applies a two-layer zonal model to simulate the flow in the region close to the walls. However, to avoid first near-wall nodes in the buffer layer region, the near-wall meshes should ideally be either coarse ($y^+ > 30$) or fine ($y^+ \approx 1$). Based on earlier work from Zhao (Zhao et al. 2013), the wall function method (applied to coarse meshes) poorly describes the near wall region with low Reynolds number flows. The airflow in the present study is relatively weak and does not have a high Reynolds number near walls. Moreover, when reducing the pot draft condition, buoyancy will significantly influence the flow features. Therefore, a fine near-wall mesh is used.

The mesh is created in GAMBIT 2.4 and consists of prism volumes in the boundary layer and Tet/Hybrid volumes in the core of the domain. A mesh independence study is presented below. A typical mesh contained ~ 2.5 million control volumes. The SIMPLE algorithm was used to solve flow equations. Default criteria in the software were used to declare convergence of a simulation. The solution strategy relied on a step-by-step procedure. One can first launch the simulation with a low value of gravity, and

converge it using first-order schemes. Following that the resulting physical fields are used as an initial guess for a new simulation in which gravity is adjusted properly. Similarly, second-order schemes could then be introduced. Approximately 24 hours were required for performing one simulation.

4.2.5 Boundary Conditions

Atmospheric pressure is imposed at the potroom boundary. The pressure at the exit (inlet of the collecting duct) was an adjustable negative pressure (-10 to -50 Pa). The exhaust draft condition can be varied by changing the inlet-to-outlet pressure difference, which is the sum of pressure losses through hood gaps and in the cavity under hoods. To simulate the CO_2 emission from the bath into the cavity, the bottom surface of feed hole was defined as a mass inflow boundary from which hot gases (CO_2) are released at 940°C with a mass flow rate of 2.6 g/s for our simulated domain (based on 1.3 vol% hot gas concentration in the pot effluents). Since the properties of CO_2 are close to those of air and the typical CO_2 concentration is just ~ 1 - 2% in the exhaust, we replaced the CO_2 gas with air to simplify the model. The turbulence intensity was set to 1% at all flow boundaries to indicate a low turbulent inflow. Turbulent viscosity ratio was fixed to 1 at the potroom boundary for simulating an external free flow (Fluent 2012). The hydraulic diameter was used to define the turbulence at the mass inflow and outlet boundaries. Impermeability and no-slip flow are assumed on all other solid surfaces.

Convective heat transfer is imposed at the surface of anode blocks immersed in the bath, at the external surface of the sidewall and at the surface of deck and ground. The bath temperature was set at 955°C . Combined external radiation and convection heat transfer is defined at the bottom surface of the crust and the surfaces of anode exposed in the CO_2 layer. The gas temperature representing CO_2 was 940°C in the present simulations. The convection coefficient in the pseudo CO_2 layer was determined by an analysis presented in the next section. At the potroom boundary, the ambient temperature near the pot is set to 50°C while the temperature is assumed to 70°C at the boundary of upper cavity. Radiation between the pot surfaces and the far-field environment is also considered in the model. The background temperature in the potroom was 30°C , and that

for the upper cavity, 70°C. On sidewalls, a heat transfer coefficient of 10 W/m²·K was considered with an ambient temperature of 100°C. The emissivity of anode cover and crust were 0.4 and 0.3, respectively (Rye et al. 1995). The emissivity of metal surfaces in the cavity was 0.8, while it was 0.5 at the surfaces outside the cavity (Perry et al. 1984). Electrical insulation is imposed on all surfaces of the domain except for the top surface of rod where a current of 8500 A/rod is imposed and the bottom of anodes imposed by a zero voltage.

4.3 Verification and Validation

Values of y^+ were verified on all wall boundaries. The value of y^+ is equal to ~ 1 in the cavity under hoods and $\sim 1-3$ in the potroom and upper cavity, which satisfies the requirement of the enhanced wall function used in SST $k-\omega$ model. Also, the blending function, which is incorporated in the SST $k-\omega$ model and which controls the turbulent model transition between the standard $k-\epsilon$ model in the core area and the $k-\omega$ model in the near-wall regions, was looked at. It was found that the $k-\epsilon$ model was successfully applied in the areas of jet flow and the core space of the cavity, while the $k-\omega$ mode was activated in the area near wall surfaces.

Mesh independence was thoroughly investigated. Previous work (Zhao et al. 2013) showed that a maximum control volume length scale of 5 cm in the core area of flow domain is fine enough to capture the main heat transfer and flow patterns. However, a refined surface mesh is required in particular areas such as for the gaps and anode assembly. The bulk volumes are created based on the surface mesh and gradually grown to 5 cm (mesh#1, 2.45 million control volumes). A mesh with a maximum volume length scale of 3 cm was also created (mesh#2), with 3.98 million control volumes. Mesh#1 was compared to mesh#2 for both ventilation rates (i.e., normal 2.4 Nm³/s, and reduced to 1.2 Nm³/s). Results did not change significantly from mesh#1 to mesh#2 (Table 4.1). Therefore, mesh#1 is considered adequate for the rest of this work. An analysis was performed to determine proper values for some uncertain simulation parameters. For example, a series of simulations was performed with different distances from the surface of hoods to the potroom boundary. It was found that the mass flow rate and temperature of the exhaust, and the heat transfer rate from the bath did not change when the potroom

domain was extended above 0.5 m. Another uncertain parameter was the convection heat transfer coefficient of the CO₂ gas under the crust. The dominant heat transfer mechanism in the cavity under crust is radiation (radiation heat transfer coefficient of ~100 W/m²·K, (Taylor et al. 1996)). Three different values of 5, 10 and 20 W/m²·K were assigned to the convection coefficient to test its influence and very little influence was found (e.g., 0.16% relative error in the total heat transfer rate from the bath). Therefore, we used a value of 10 W/m²·K in the rest of this work.

Table 4.1 Comparison of CFD results with two meshes, for two ventilation conditions (shaded lines are for reduced ventilation).

Parameter	Mesh#1	Mesh#2	Relative error, %	Description
\dot{m}_{gas} (kg / s)	0.1446	0.1452	0.41	Mass flow rate at exit
	0.0734	0.0733	0.14	
T_{gas} (°C)	132.5	133.5	0.75	Gas average temp. at exit
	175.5	174.5	0.57	
T_{hood} (°C)	138.5	138.5	0	Average temp. of hoods
	169.5	172.5	1.7	
p_{gap} (Pa)	-18.55	-18.75	1	Aver. pressure at gaps
	-4.28	-4.28	0	
q_{gas} (W)	15650	15800	0.95	Heat loss at exit
	11100	11050	0.45	
q_{bath} (W)	9100	9160	0.66	Heat transfer rate from bath
	8380	8360	0.24	

4.4 Top Heat Loss in Current Pots under Normal and Reduced Ventilation Rates

When reducing ventilation in the pot, one of the most adverse influences is the reduction of bath heat loss by the top of the cell. When that happens more heat will escape by the sidewalls, which is exactly where the protective ledge thickness is very sensitive to the heat flux. A higher heat flux may melt the inner frozen crust and narrow the lining thickness. Moreover, the crust strength over the side-channel could also be reduced due to the inner crust melting, which is likely to increase the area of collapsed open holes in the side-channel cover. Therefore, when reducing the ventilation of the cell, strategies should be developed in order to increase the top bath heat loss up to its “normal” value to avoid these negative impacts. In order to understand how the heat transfer changes in the domain due to ventilation reduction, a simulation was performed under normal ventilation ($2.4 \text{ Nm}^3/\text{s}$) and another one, under reduced ventilation (50% of normal ventilation rate).

Figure 4.2 reports the heat transfer rate related to different components under the two ventilation scenarios considered. q_{bath} represents the total heat extracted from the bath through the top of the cell. q_{cover} , q_{stubs} , q_{yoke} , and q_{rod} represent respectively the total heat transfer rate that leaves the surface area of the cover, stubs, yoke and rod that is exposed to the gas in the cavity. Note that the total heat loss via the upper part of a pot consists of the heat extracted from bath (q_{bath}) and the heat generated by Joule heating in the anode and the anode assembly, which is why the summation of q_{cover} , q_{stubs} , q_{yoke} , and q_{rod} is larger than q_{bath} . Experiments (Shen et al. 2008) performed in a 75 kA prebaked cell have shown that under normal conditions ~76% of the heat leaves the domain in the exhaust gas and the rest (~24%) is being dissipated directly in the potroom environment via the surfaces of hoods and superstructures. The anode assembly (in particular, stubs and yoke) is responsible for most of the heat loss via the top of the cell, while there is also a significant portion escaping through the anode cover. When appropriate, a line separates the radiative and convective contributions in Fig. 4.2. For example, the heat loss from the top surface of anode cover (q_{cover}) is reduced from 4805 W to 4435 W when the ventilation flow is reduced by half. However, the radiative heat loss is actually increased by 755 W while the convective heat loss is attenuated by 1125 W. The rod surface is a special case where radiation is received and therefore the radiation heat transfer rate is a

negative value (indicated by the dotted bars, in Fig. 4.2). The convective heat loss is actually the sum of the solid bar (net heat loss) and the dotted bar in each case.

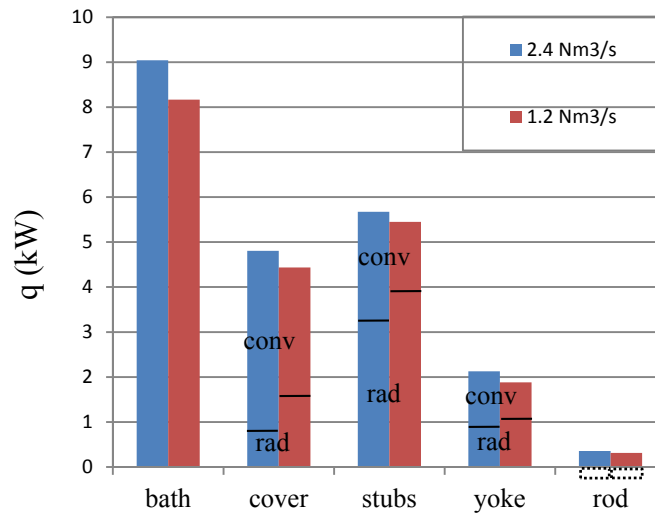


Figure 4.2 Heat losses due to convection and radiation from different components in different ventilation conditions.

When the ventilation flow is reduced by half, the total heat transfer rate extracted from bath by the top of the cell is decreased from 9040 W to 8165 W, i.e. a reduction of 875 W (in the two anodes model). In practice, this extra heat of 875 W would have to escape from other pot components. It is found that the heat losses from all surfaces are reduced somehow. And although the heat loss reduction by each surface seems relatively weak, their sum is large enough to potentially influence the overall pot thermal balance. Looking at Fig. 4.2, one can also conclude that convective heat losses are reduced in a less ventilated pot, while the radiation increases due to warmer surfaces. However, the overall enhanced radiative heat loss is not enough to compensate the reduction in convective heat loss. Convection is the main mechanism for heat loss from anode cover surface, while radiation dominates the heat loss from anode assembly surface.

Some conclusions can be drawn from the abovementioned analysis. These will help to design proper modifications to the pot in order to maintain thermal equilibrium under low ventilation scenarios:

- (i) The convective heat loss in the cavity is decreased as the ventilation is reduced, while the radiative heat loss has the opposite behavior.

(ii) The enhanced radiative heat loss is not enough to compensate the reduction of convective heat loss due to ventilation reduction, and this is the main reason why the net top heat loss is reduced.

(iii) Radiation plays a significant role on the yoke and stubs for the two draft conditions. When ventilation is reduced, radiation becomes the most influencing mechanism in the top heat loss.

Three types of modifications are studied in the following sections to achieve proper thermal equilibrium (i.e., to extract from the bath the missing 875 W of heat mentioned previously): use of fins on the anode assembly, change of the gaps geometry, and change of anode cover geometry and surface properties.

4.5 Addition of Fins on Anode Assembly

The first group of scenarios is the addition of fins on the anode assembly. Plate fins were positioned on anode yoke and stubs, as shown in Fig. 4.3. The purpose of the fins is to increase the convective heat loss from the anode assembly to the airflow in the cavity. Traditionally, the design of fins involves an optimization of different design variables, e.g. fin dimensions, materials and arrangement. Here, we studied two designs (cases a1 and a2) to evaluate their efficiency in maintaining top heat loss under low flow of ventilation. We fixed the fin width and thickness at 5 cm and 1 cm, respectively. Fin material is steel (as yoke and stubs). Case a1 only has one plate fin, while case a2 has three plate fins. New meshes were built with the fins and CFD simulations were performed under reduced ventilation for these designs.

The influence of fins on the total heat transfer rate from bath is shown in Fig. 4.4. Compared to the 1.2 Nm³/s ventilated situation with no fins (case_1/2), case a1 increases the heat transfer rate from the bath by 315W and case a2 by 385W, respectively (see Fig. 4.4). It is found that using one or three fins does not change significantly the net top heat losses. However, in both cases, there is still a significant gap for achieving the “normal” heat transfer rate dissipated via the top section under normal level of ventilation flow. The use of fins on anode assembly was thus found to be inadequate to fully compensate the reduction of top heat loss caused by such reduced ventilation flow. Even though this scenario could be applied, the addition of fins on anode assembly needs to deal with

several practical problems. For a used anode assembly, the carbon butt has to be knocked off and recycled, and the anode assembly is sent to the rodding workshop and prepared for re-use. During this process, the deformation of fins (or even destruction) on the anode assembly seems to be inevitable.

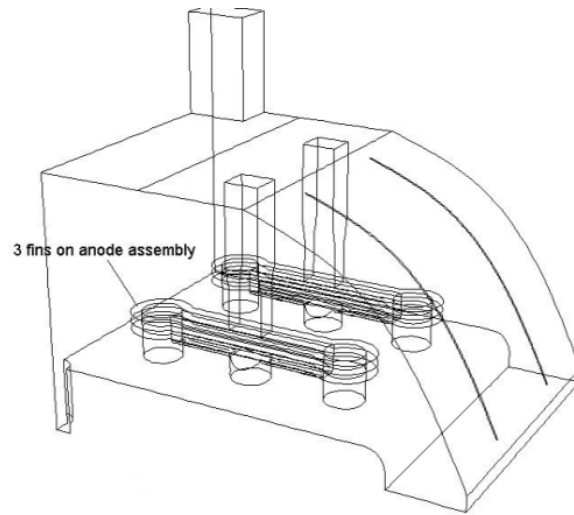


Figure 4.3 Schematic of fins addition on anode assembly (case a2).

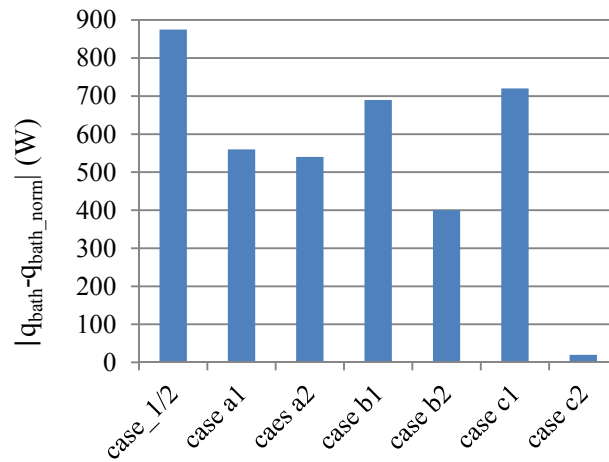


Figure 4.4 The difference of heat transfer rate extracted from bath by the top of the cell between normal condition and simulated scenarios.

In order to understand why such a result was achieved, the relative enhancement of convective and radiative heat losses from different components, for different scenarios, is presented in Table 4.2. The reference case for this table is the 50% of normal ventilation case, without fins, namely case_1/2. Positive heat transfer rate indicates an enhancement with respect to case_1/2 while a negative value means reduction of heat transfer introduced by the geometrical modification. Table 4.2 indicates that on the one hand fins increase the convective heat loss on cover, stubs and yoke, while on the other hand the fins reduce the radiative heat loss from these components (cases a1 and a2). It can be explained by the fact that the fins on anode assembly block the radiation transfer from cover, yoke and stubs to other cold surfaces. Although the fins create more surface area, the overall effect on the radiation heat transfer is nevertheless negative. Therefore, fins alone were found to be poorly efficient, in particular when considering the complexity they would introduce in production and mechanical operations.

4.6 Modification of Hood Gaps Geometry

In the second group of scenarios, we considered to enhance the convection heat losses by increasing the induced airflow velocity from hood gaps (case b1) or by adopting a horizontal flow arrangement from hood gaps (case b2). In case b1, the flow velocity can be increased by reducing the total gap area (increasing the tightness of the pot). We assumed in the CFD model a uniform width of 1 cm for each gap. The gap area could be reduced by welding flaps on the edge of each hood to cover a part of the gap. It is obvious that the covering flaps cannot provide a perfect sealing on hood gaps. However, comparing with the mass flow rate through uncovered gaps, the leakage through flapped gaps could be neglected in the present model. In this scenario (b1, as shown in Fig. 4.5 on left), the upper half of each gap was assumed covered and therefore the flow velocity through the uncovered gap needs to be doubled in order to maintain the same mass flow rate through the pot. The results are shown in Fig. 4.4. It is found that there is still a ~700 W gap of the heat transfer rate from bath compared to normal operating conditions. Even though the faster induced flow significantly increases the convection heat loss on anode cover, when comparing with case_1/2 there is a large sacrifice in the radiative heat loss from anode cover, as illustrated in Table 4.2. In addition, the convective heat loss

from the anode assembly is not significantly increased in this case. The flow induced from the lower half gap is “trapped” in the side-channel which is formed by the height difference between the anodic block and the pot deck. Another negative effect is that the more tight pot structure introduces a significant increase on the driving pressure difference (i.e. from -10 Pa to -40 Pa) and would therefore need additional fan power to maintain 50% of normal ventilation. In the future, an optimization on the flow pattern could be helpful for the convection enhancement on the anode assembly.

To replace current vertical gaps, a horizontal gap was considered in case b2, as shown in Fig. 4.5 on right. With such geometry, the flow passes more efficiently over the anode cover and anode assembly. A horizontal gap on hoods was created in the CFD model and the gaps between hoods were covered by flaps as in case b1. From Fig. 4.4, we found that the heat transfer rate from bath was increased by ~ 475 W when compared with the 50% normal ventilation case. In other words, there is still ~ 400 W of heat extracted from the bath that is missing compared to normal conditions. Table 4.2 indicates that the convective heat losses from cover, stubs and yoke are distinctly enhanced by such flow arrangement. However, the overall enhancement of heat loss is attenuated by the reduction of radiation heat transfer on all three surfaces. This is due to the strong temperature-dependence of radiative emissions. A small surface temperature reduction induced by convection can result in a large radiative heat transfer reduction. In any case, both strategies b1 and b2 are not adequate enough to recover the reduction of top heat loss under the low ventilation condition studied here. Moreover, a reduction in the gap area will also induce a significant additional pressure difference to maintain the ventilation rate as it is.

Table 4.2 Convection and radiation heat transfer enhancement (in W) provided by different scenarios compared to case_1/2.

		case a1	case a2	case b1	case b2	case c1	case c2
cover	conv	325	262	687	624	71	402
	rad	-282	-258	-547	-503	90	-425
stubs	conv	421	599	180	610	63	464
	rad	-303	-371	-61	-406	-106	738
yoke	conv	241	258	-207	178	82	46
	rad	-141	-170	109	-99	-38	-272
rod	conv	-26	-28	-5	-10	7	12
	rad	-1	7	24	22	-21	-80

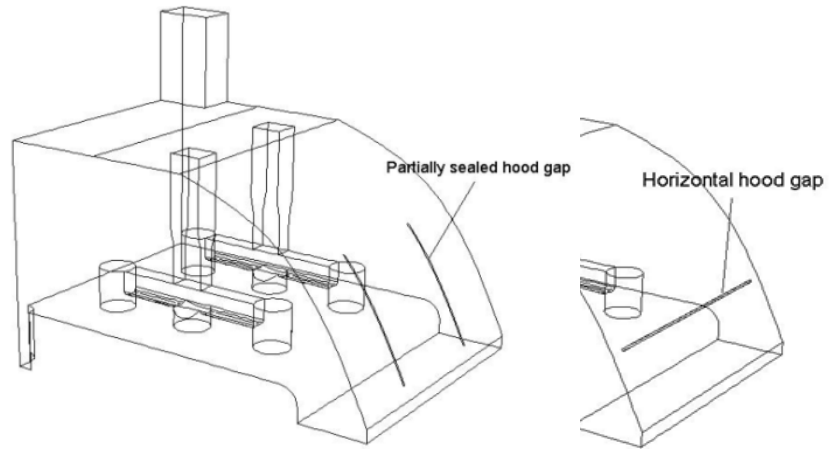


Figure 4.5 Schematics of sealed hood gaps (case b1, left) and horizontal hood gaps (case b2, right).

4.7 Modifications on Anode Cover

For an opaque, diffuse, gray surface, the net radiative transfer is strongly influenced by the surface emissivity. When increasing the emissivity, the net radiation transfer of the surface will also increase. For the normal condition the emissivity of the top surface of anode cover was assumed to be 0.4. In case c1 we assumed that the emissivity could be increased to 0.8 (e.g., a dust layer on the anode cover) and with that we performed the simulation without any other geometrical modification. By studying the results presented in Fig. 4.4 and Table 4.2, the increase in terms of top heat loss was found to be limited: Only ~200 W additional heat is extracted and when compared to the low ventilation case without modification; there is still ~700 W that should be extracted in order to maintain current conditions.

When the ventilation flow is reduced to 50% of normal condition, the contribution from radiation in the top heat loss is larger than that of convection, as shown in Fig. 4.2. Since the addition of fins on anode assembly has proven to suppress the radiative heat transfer, one may think about enhancing the radiation heat loss rather than the convective heat loss. The radiative heat exchanges between surfaces are determined by surface emissivity and temperature, view factors and surface areas. Among these factors, view factor and surface area are strongly dependent on the pot geometry. In case c2, the idea tested consisted in exposing an additional segment of anode stubs (5 cm deep) in the cavity by removing some anode cover material surrounding the stubs, as shown in Fig. 4.6. In such a case, the deeper exposed stubs have a higher surface temperature which can increase both convection and radiation heat transfer from these surfaces. Meanwhile, the original configuration of anode assembly is maintained to avoid any interference of additional structure in the radiation heat exchanges in the cavity. Moreover, the anode cover still has a 5 cm thickness close to the stubs to prevent the anode from being burnt with the oxygen of the air. Results of the CFD simulations are shown in Fig. 4.4. The heat transfer rate from bath in case c2 is almost the same as that in the normal ventilation case. This strategy thus seems to have the potential to enhance the top heat loss to the normal level while the ventilation flow is reduced by half. By studying the detailed information of heat losses from different components in Table 4.2, we found that the heat loss from the stubs is significantly enhanced, both by convection and radiation. The more

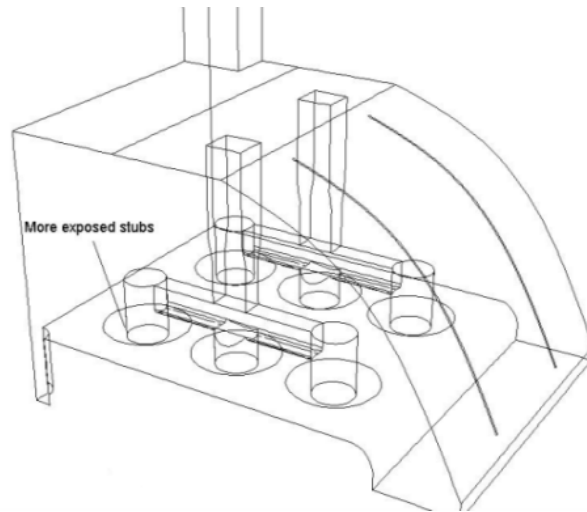


Figure 4.6 Schematic of more exposed stubs in the cavity (case c2).

exposed stubs with higher temperature ($\sim 500^{\circ}\text{C}$) can emit more radiation while convective heat loss is also increased as a result from more stubs in contact with the airflow in the cavity. Lastly, this modification will induce little effect on the total driving pressure between the gaps and exit.

4.8 Conclusions

Different advantages can be envisioned by a reduction of cell ventilation. However, it also creates thermal imbalance compared to current pot operation since less heat is removed from the bath by the top of the cell. A CFD model of the upper part of a typical cell was developed in order to investigate different scenarios. The objective was to find how to maintain the same amount of heat removed from the bath even when the ventilation is reduced. The most promising set-up found was to expose a larger portion of the stubs to the flow of air. In future work, different simultaneous combinations of the different scenarios could be investigated.

**CHAPTER 5 AIRFLOW AND THERMAL CONDITIONS IN ALUMINUM
SMELTING POTROOMS UNDER DIFFERENT CONDITIONS**

Abstract

Potrooms are elongated buildings in which electrolysis of alumina is carried out, and have the particularity, among others, to be naturally ventilated. A CFD model is developed to simulate the ventilation and heat transfer patterns within a smelter potroom. The model is used to study thermal comfort in the potroom under different wind and outdoor temperature scenarios. The influence of wind and buoyancy on the airflow rate through potroom openings is demonstrated. The heat stress during hot weather is assessed for the different cases. In particular, the reduction of pot ventilation rate, a potential strategy for facilitating waste heat recovery from smelting cells, is assessed in terms of its influence on the thermal conditions in the potroom. It is found that the pot draft reduction can be realised without significantly increasing the heat stress.

Résumé

Les salles de cuves sont des bâtiments allongés où l'électrolyse de l'aluminium est réalisée et qui ont comme particularité d'être ventilées naturellement. Un modèle CFD est développé pour simuler la ventilation et le transfert thermique dans ce bâtiment. Le modèle est utilisé pour étudier le confort thermique dans la salle de cuves sous différentes conditions de vent et de température extérieure. L'influence du vent et de la force d'Archimède sur le débit d'air évacué est démontrée. Le stress thermique pendant l'été est déterminé pour différents cas. En particulier, la réduction de la ventilation des cuves, (une stratégie potentielle pour faciliter la récupération des rejets thermiques d'une cuve) est étudiée en termes de son influence sur les conditions thermiques dans la salle de cuves. Il est montré que les modifications de ces conditions n'ont pas d'impacts significatifs.

5.1 Introduction

Primary aluminum is produced via the Hall-Héroult process (Grjotheim and Kvande 1986). Electrolytic cells (often called “pots”) are aligned in a long building named a “potroom”, as shown in Fig. 5.1a. As our reference, this is an Alcoa’s smelter at Deschambault in Québec, Canada (ADQ). Although this process is over a century old, the energy efficiency is still relatively low, with roughly half of the energy input dissipated into the atmosphere in the form of waste heat. Considering that efficiency, the electricity requirement of 13-15 MWh to produce one ton of aluminum, and typical plant dimensions and productivity, it can be estimated that the smelting process corresponds to a continuous internal heat gain of $\sim 6500 \text{ W/m}^2$ of floor. This value is quite large compared to internal gains in other types of buildings. The typical ventilation system to cope with this heat gain in potrooms is described with more details in Section 5.2.

The process heat escapes from a pot in part through its shell directly into the potroom air. Also, heat is released via the pot exhaust gases (mixture of dilution air introduced into the pot and of process by-products such as CO_2), collected by a duct system. The exhaust gas can contain $\sim 35\text{-}40\%$ of the total waste heat, at a temperature approximately 100°C above ambient. Although the amount of heat released from pots is enormous, most of the heat either has a relatively low thermal quality (low temperature) or is difficult to recover (sensitive to working conditions). In order to increase the potential benefits of using pot gas for waste heat recovery, its temperature would need to be increased. Several theoretical and experimental studies have illustrated that the pot exhaust gas temperature is significantly increased by reducing the amount of dilution air introduced in the pot, i.e. the pot ventilation level (Gadd 2003; Abbas et al. 2009; Abbas 2010; Lorentsen et al. 2009). Recently, Zhao et al. (2013; 2013a) have studied the top heat losses in a smelting pot, and their results have demonstrated the potential of increasing pot gas temperature up to 50°C by reducing half of the pot normal draft level. Considering an application such as power generation with an Organic Rankine Cycle, this temperature raise could significantly increase the efficiency of the cycle in such a way that it could become more viable. However, attention should be paid on the influence of pot draft condition on potroom building performance and workers’ health. A reduced pot ventilation redistributes the heat losses in the upper part of smelting cells (Abbas et al.

2009; Zhao et al. 2013a). A portion of the heat, previously taken away by the exhaust gas will be redirected into the potroom. Considering current high internal heat gain in potroom, it is required to verify how reduced pot ventilation would modify thermal conditions in potroom and how the overall potroom ventilation would be affected. Also, the influence of outdoor weather conditions combining with the reduced pot draft condition is yet to be addressed. Building heat stress in harsh environments such as potrooms in summer should be carefully assessed to maintain people's safety and health. Modifications in the potroom, if necessary, should thus be done before implementing pot ventilation reduction.

Computational Fluid Dynamics (CFD) has become very popular to study ventilation patterns in the built environment over the past 20 years (Chow 1995; Li et al. 2013). Building ventilation can be qualified of either mechanical or natural depending on the driving mechanisms. Ventilation in potrooms is almost entirely driven by buoyancy forces due to the heat released from smelting pots. Furthermore, wind is also important as it creates a pressure difference at the openings of the building. One of the exploratory works on simulating turbulent flow in the presence of strong buoyancy forces in a building enclosure was performed by Cook and Lomas (1998), where they validated the two eddy viscosity turbulence model for predicting a buoyancy-driven ventilated flow by comparing simulation results with experimental measurements. Cook et al. (2003) used CFD simulations to study the wind-assisted stack ventilation of a single-storey enclosure with high and low-level openings. They developed an approach to impose constant pressure boundary conditions at the inlet and outlet of the enclosure rather than to simulate the flow transport through them from an external domain. This approach can significantly reduce the simulated domain while maintaining an accurate prediction of flow and thermal conditions in the enclosure. Recently, Ji et al. (Ji et al. 2007; Ji and Cook 2007) extended their CFD models into more complicated building structures, such as single-storey with atrium and multi-storey with atrium.

In the present paper, we estimate the influence of pot ventilation reduction on the flow pattern and thermal conditions in potroom by using CFD simulations. In addition to presenting an advanced potroom ventilation model, the main purpose is to verify whether the thermal conditions in the potroom under low pot ventilation levels are acceptable. An

allowable working time is calculated to assess the heat stress based on the thermal balance between the human metabolism and the hot environment. In addition, the changes in airflow patterns and temperature fields around the pot are of interest. In order to reduce the computational burden, the outdoor environment was not included in the CFD model and we considered the wind-assisted ventilation by imposing an equivalent pressure difference between the inlet and outlet of the potroom. Several typical scenarios, considering the influences of wind, ambient temperature, and solar radiation, were simulated.

5.2 Description of the ventilation in potrooms

In modern smelters, aluminum is produced in a series of elongated buildings called potrooms, each of which containing several dozens of smelting pots. A typical potroom can have a footprint of 1000 m by 30 m, and a height of 25 m. Pots are lined up along the potroom length and are electrically connected in series. Figure 5.1b shows the simulated geometry, which consists of one slice of potroom where two half-pots and other pieces of equipment are included. Normally, one end of the pot is facing the working aisle for tapping operations, and the other end is connected with the ducts collecting pot exhaust gases. Between two pots, a space is reserved for the installation of busbars and for pot operations (e.g., anode change).

Because the aluminum reduction process releases a large amount of heat from pot shell into the potroom (~450 kW per pot), outdoor air is used for cooling down the pots and keeping the potroom environment comfortable. Additionally, a certain amount of air from the potroom is driven into the pots (to collect CO₂ and other gases emitted by the process) and must be replaced by fresh air. Finally, pollutants released from pots and other equipment into the potroom (such as HF, SO₂, etc.), if any, must be diluted by the makeup air to acceptable concentration levels.

Ventilation of smelters relies essentially on buoyancy forces. The potroom can be viewed as a two-storey building. The lower floor is the basement, where openings are created on the two long façades of the building. The openings are equipped with panels that can be adjusted to increase or reduce their effective areas, and thus, the amount of makeup air. This adjustment is performed on a seasonal timescale and panels are usually

removed in the summer. Once ambient air is induced into the basement, a portion of the flow goes into the potroom (the upper floor) through claustra walls on the lateral sides (shown as arrow 1 in Fig. 5.1b), and the rest of the incoming airflow is going in basement and through two louvered plates in the floor between consecutive pots (arrow 2 in Fig. 5.1b). The air captures heat from pot surfaces, and is thus driven upward due to the buoyancy forces created by the interior-to-exterior air density difference (arrow 3 in Fig. 5.1b). A portion of the warmed air is exhausted through the vent at the roof while the rest flows to two lateral façades and falls down to the working floor (arrow 4 in Fig. 5.1b). Additionally, a small amount of air is taken into the pots through small gaps between hoods. A negative pressure is maintained in the pots to avoid releasing hazardous gases into the potroom environment. In addition to the stack effect, the inlet-to-outlet pressure difference due to the outdoor wind impinging on buildings can also assist or suppress the total ventilated airflow rate, depending on the exterior environmental conditions.

5.3 CFD modeling

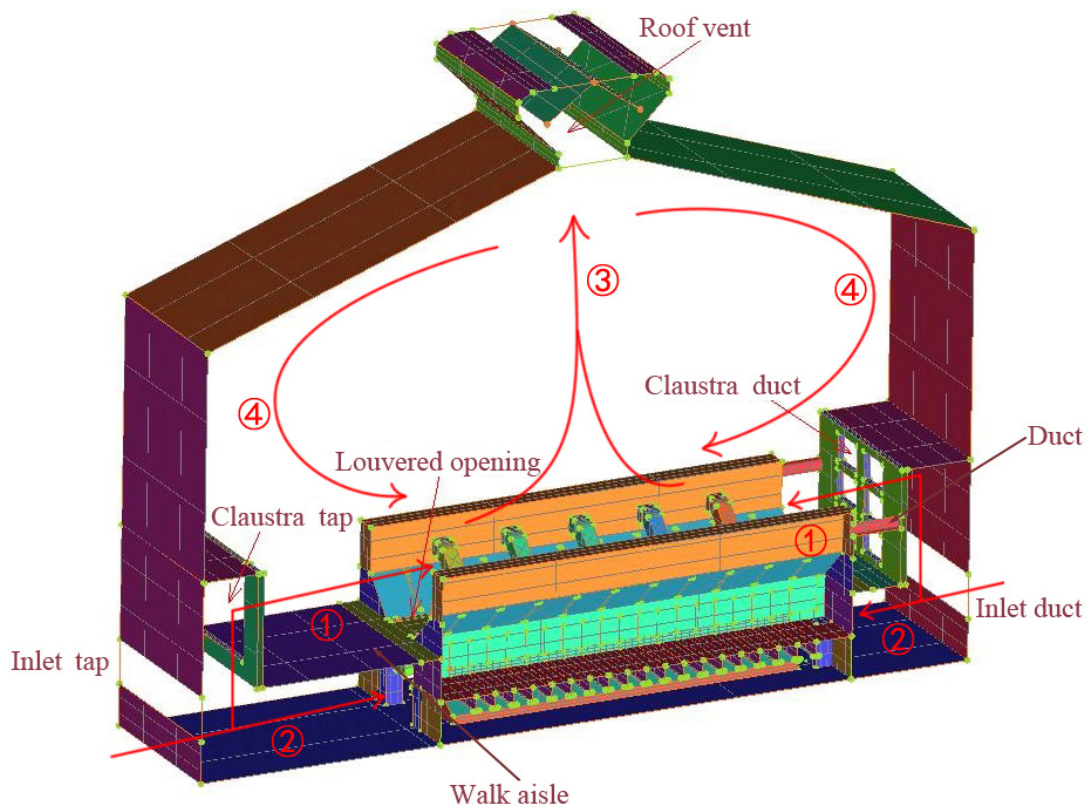
5.3.1 Description of the numerical domain

In order to reduce the computational burden while keeping an adequate representation of the physical geometry, only a slice of potroom was modeled considering the periodicity of the pot arrangement in the potroom, as shown in Fig. 5.1. Several assumptions were invoked to simplify the geometry:

- i) The complex physicochemical phenomena taking place in a smelting pot were not included in the model. A pot shell representing each “façade” of the pot was created and heat flux conditions were specifically imposed on each surface to simulate the heat loss from the pot.



(a)



(b)

Figure 5.1 (a) A plan of the studied smelter and (b) simulated domain representing a slice of potroom.

- ii) We ignored the detailed geometry of the structure above the super plate (i.e., anode bars, holding beam, and joint parts). Five busbars were considered. The assumption is reasonable since in the present work we are not interested in the detailed heat transfer and fluid flow in the vicinity of these parts. At the duct end, a segment of the pot collecting duct was included in the model. Although the pot geometry is significantly simplified, the thermal boundary conditions are defined in such a way that the total amount of heat released in the potroom is as in the actual one.
- iii) The only pot gaps included in the model are the openings between hoods. However, due to the tremendous scale variation between the gap breadth ($\sim 0.005\text{--}0.05$ m) and the potroom width (~ 20 m), it is difficult to model the real gap geometry, and at the same time, maintain the number of control volumes of the mesh to an acceptable value. A series of ten gaps with a width 0.1 m were thus created to represent hood gaps on each side of a pot. Gaps between hoods and superstructure, and around anode rods were not considered, because of their small surface areas.
- iv) The pot shell has many extrusive structures which could tremendously increase the number of modelling cells. A series of pot cradles was considered since it creates a significant resistance to airflow. Moreover, there exist other components in the basement between two pots, such as the cathode collecting bar, the anode and cathode busbars. All these structures were represented by a single large bar located in the area between two pots. A porous jump surface was created beneath the bar for simulating the resistance to airflow of these bars on the up-rising air flow.
- v) The perforated claustra wall and louvered pot sides create additional resistance to airflow. In the model, a porous zone is defined to simulate the claustra wall, and a porous jump surface is considered at the louver area.

5.3.2 Governing equations

The governing equations representing the conservations of mass, momentum in each direction, and energy are discretized and solved with a commercial CFD software, Ansys Fluent 13.0. Turbulence was considered in the governing equations via the Reynolds-averaged Navier-Stokes (RANS) method. The Reynolds stresses term due to turbulence is modeled based on the Boussinesq eddy viscosity assumption. Detailed formulas are

available in literature (Fluent 2012). In the present problem, incompressible flow and steady-state conditions are considered. Pressure work and kinetic energy terms are neglected in the energy equation since the gas is treated as an incompressible flow. Viscous heating is also disregarded in the simulation. Species diffusion is not considered in the problem.

The air properties (i.e., specific heat, thermal conductivity and viscosity) are functions of temperature (polynomial fittings based on the data published in (Bergman et al. 2011)). The air density is modeled by using the “incompressible-ideal-gas” model, and is defined as:

$$\rho = \frac{p_{op}}{\frac{R}{M_w} T} \quad (5.1)$$

where R is the universal gas constant, M_w , the molecular weight of the gas, and p_{op} , the defined operating pressure (constant) which is the mean pressure in the simulated domain. Under this approach, the air density is only influenced by the local temperature field and the buoyancy force in the momentum equations is proportional to density variations. A “reduced pressure” (pressure minus hydrostatic pressure, i.e. $p' = p - \rho_{ref} gH$), is considered in the momentum equations. Therefore, a reference density ρ_{ref} should be defined. In the present case, it is equal to that at the outdoor temperature in order to consider stack effect appropriately. Detailed description of these choices is presented in (Zhao and Gosselin 2014).

A turbulence model is required to close the model. Two equation eddy-viscosity turbulence models are generally suitable for the simulation of air flow and heat transfer of indoor environments, particularly when the time-averaged parameters, such as mean temperature or mean flow velocity, are the results of interest (Zhai et al. 2007; Zhang et al. 2007). Based on a literature review, it was found that the RNG k- ϵ model and the SST k- ω model are the most appreciated two equation eddy-viscosity models used in the simulation of indoor air flow. Since the SST k- ω model shows a good performance in the simulations of various types of natural ventilation in buildings (Hussain and Oosthuizen 2012b; Ramponi and Blocken 2012), it is determined to simulate the turbulence in all simulations in this work.

Discrete Ordinates (DO) model was used in the simulations to account for radiation, since this model is supported for parallel calculations. Although air is treated as a non-participating medium, DOs allow determining surface-to-surface heat transfer rates in the complex geometry of this problem. Additionally, this radiation model can also provide the radiant temperature field within the entire domain, which is required in order to assess thermal comfort of the workers (Parsons 1999).

The model is solved in steady-state conditions. The method to interpolate the variable gradient is the least squares cell-based gradient evaluation. PRESTO! scheme is chosen for the pressure interpolation at the surfaces of control volume. Pressure-velocity coupling is achieved by using SIMPLE segregated algorithm. All of the other variables are interpolated with a second-order upwind scheme except for the radiative intensity, which can be appropriately calculated in the first-order because the air is considered as non-participating medium and the optical thickness is thus zero in the radiation transport equation. Convergence is achieved when scaled residues of the governing equation are reaching the default recommended values (Fluent 2012).

5.3.3 Boundary conditions

As mentioned previously, the exterior of the potroom was not included in the simulation. Based on the approach developed in (Cook et al. 2003), pressure was imposed at the inlets and outlets of the potroom to represent the wind force. The pressure created by the wind on the building façade is calculated by the following equation:

$$p_{wind} = C_{p_wind} \frac{1}{2} \rho_o U_{ref}^2 \quad (5.2)$$

where C_{p_wind} is the pressure coefficient, ρ_o the exterior air density, and U_{ref} the mean wind speed at an external reference position. C_{p_wind} is a dimensionless parameter and is influenced by the shape of the building, the wind direction and the neighboring terrain. Although C_{p_wind} values can be obtained from some established correlations or calculation programs, determining the correct pressure coefficient is a challenge in itself. A CFD model was created to simulate the air movement around a potroom building (Zhao and Gosselin 2014). The results illustrated that the C_{p_wind} values are quite different from

those calculated from the available tools, because of the geometrical specificity of potroom (i.e. an extremely elongated shape). We adopted the interpolated wind pressure coefficients at windward, leeward and top roof from the CFD model of the previous work. It should be noticed that these C_{p_wind} values are only valid for the wind direction perpendicular to the lateral potroom walls.

A special attention needs to be devoted to determining U_{ref} in Eq. (5.2). Normally, the mean wind speed is measured at the height of a meteorological station tower which is located in a relatively flat terrain and with no local shielding. The variation of mean wind speed with the height is most commonly represented by a power law expression. Eq. (5.3) was used to adjust the mean wind speed from a local meteorological station to the terrain of the studied building.

$$U_{ref} = U_{met} \left(\frac{\delta_{met}}{H_{met}} \right)^{\alpha_{met}} \left(\frac{H_{ref}}{\delta} \right)^{\alpha} \quad (5.3)$$

where U_{met} is the mean wind speed measured at the tip of the weather station tower, and H_{met} , the height of the tower, usually 33 ft (10 m) above ground level. The reference height H_{ref} is usually defined as 10 m from the ground. α and δ are atmospheric boundary layer parameters and determined based on the classification of terrain category (ASHRAE 2009). The values of wind speed measured at the closest weather station were thus adjusted with Eq. (5.3) to obtain the required reference velocity. In this work, reference velocity values of 0, 5 and 15 km/h were found to be representative of different levels of wind strength. Once the reference velocity, along with the average pressure coefficients at the inlets and outlets are obtained, the imposed pressure boundary conditions could be calculated using Eq. (5.2). For the smelter considered (ADQ), two wind directions are of particular interest, from northwest and from southeast, both of which being approximately perpendicular to the two long façades of the potroom. As seen in Fig. 5.1, the potroom-slice model has an inlet at the tapping end (the side close to the walking aisle), an inlet at the duct end (the side close to the off-gas collecting ducts) and an outlet at the roof vent. With the CFD model that was developed, one can define either the tapping end or the duct end as the windward side (positive pressure) to simulate the wind blowing from either direction. Table 5.1 presents the calculated pressure

boundary conditions with different wind reference velocities. We assumed that the inlet at the tapping end is windward side based on the dominant wind direction.

Table 5.1 Pressure boundary conditions [Pa].

	Scenario 1	Scenario 2	Scenario 3
Windward inlet	0	0.71	5.76
Leeward inlet	0	-1.53	-12.5
Roof vent	0	-1.2	-9.6

One of the disadvantages of imposing boundary conditions at building openings rather than far away from the building (i.e., with a model that would include a portion of the ambient) is that the detailed flow pattern through the openings, namely the contraction of the flow as it enters an opening and its subsequent expansion, will not be captured. These effects will reduce the flow rate through openings. In order to incorporate that aspect into the CFD model, the areas of the openings have been reduced by a factor corresponding to the discharge coefficient C_d for outlet and expansion coefficient C_e for inlet. In this work, we have thus reduced both the inlet and outlet areas by a factor 0.6. By imposing a constant pressure in the reduced area, the net effect is to obtain a flow rate equivalent to the actual one. Detailed validation of this procedure was presented in (Cook et al. 2003).

The turbulence parameters are required at the inlets of the building. We specified the hydraulic diameter and the turbulence intensity at the inlet of each long façade of the potroom. The hydraulic diameter is calculated with $D_h = 2LW/(L+W)$, where L and W are the length and width of the opening. Turbulence intensity is relatively difficult to obtain, since the outdoor atmospheric boundary layer is significantly influenced by the studied building and the surrounding obstacles. Results from wind tunnel tests reported in literature normally report only the measurement of turbulence intensity profile in an atmospheric boundary layer without the presence of the studied building (True 2003; Saathof et al. 1995). Through all of the literature, the turbulence intensity at the level near the ground is typical reported in the range of 15%-30%. A sensitivity analysis was performed to verify the impact of different turbulence intensity on the parameters of

interest, e.g., the ventilated airflow rates through inlets and outlet, the temperature at the vent, etc. The results have shown that increasing the turbulence intensity at the inlet from 10% to 30% only had a marginal effect on the parameters of interest. The turbulence conditions in the upstream flow have a very limited influence on the flow condition inside the potroom since the ventilated air flow pattern is strongly redefined when it is going through the claustra walls and the louvered sides.

A special attention was devoted to the pot louvered sides and to the two lateral claustra walls, which consist of internal sub-structures and provide additional resistances to the airflow represented by porous jumps. The software user's guide (Fluent 2012) provides an analytical expression, which is widely applied for calculating the mass flow rate of a turbulent flow through square-edged holes in a plate:

$$\dot{m} = C_d A_f \sqrt{(2\rho\Delta p) / (1 - (A_f / A_p)^2)} \quad (5.4)$$

Rearranging the equation and using the relationship $\dot{m} = \rho v A_p$, we can obtain

$$\frac{\Delta p}{\Delta x} = \left(\frac{1}{2} \rho v^2 \right) \underbrace{\frac{1}{C_d^2} \frac{(A_p / A_f)^2 - 1}{t}}_{C'_p} \quad (5.5)$$

where the right-hand side term corresponds to a pressure loss coefficient, C'_p . Smith and Winkle have proposed correlations for the discharge coefficient, C , through perforated plates with square-edged holes on equilateral triangular spacing for different Reynolds numbers (Smith and Van Winkle 1958). The claustra wall at the side of the walking aisle is actually a square-hole perforated wall. We found an approximate discharge coefficient of $C_d=0.95$ based on these correlations and the geometrical characteristics of the claustra wall (i.e. thickness of the wall, hydraulic diameter of the holes, and ratio of hole pitch and hole diameter). Then the pressure loss coefficient of the claustra wall was calculated. As for the other claustra wall (at the duct end), 6 empty blocks were created in the wall body. Since the porosity in each hole is extremely high (~ 0.95), we assumed no flow resistance there. Finally, a porous-jump wall was defined on the louvered surfaces. The porous thickness is set at 6 cm and the pressure loss coefficient, 20 m^{-1} .

Thermal boundary conditions were applied on the surface of the potshells. Based on a series of measurements of heat losses from potshells performed by Alcoa, the

thermal boundary conditions were determined in order to achieve the same level of heat dissipation in the potroom as in practice. Uniform heat fluxes were assumed on all pot surfaces except for the pot sidewall where large variations of heat flux were observed in measurements. A polynomial fit of the heat flux versus position was created at the sidewall based on experimental measurements. As mentioned in the introduction, scenarios with reduced pot ventilation will be simulated in this work. In such a case, the capacity of the pot exhaust flow to carry away heat from the pot will be reduced due to smaller mass flow rate. A portion of the dissipated heat that was previously exhausted by the pot flue gases will be redirected to the pot superstructures (including hoods). A new distribution of the heat losses from the upper part of the pot was obtained based on our previous work (Zhao et al. 2013; Zhao et al. 2013a). The heat losses distribution among the pot gas, pot superstructure and hoods was established for a variety of ventilation conditions. Even in reduced pot ventilation scenarios, it is assumed that the total heat loss will remain constant, only its distribution between the different pot components will change. This is a prerequisite condition for reducing pot ventilation because the heat balance in bath should be maintained all the time. Zhao et al. (2013a) have shown that it is possible to maintain the pot thermal balance in reduced pot ventilation by adjusting different aspects of the pot design and operation. Table 5.2 presents the defined heat flux on pot shell under normal and 50% reduced pot ventilation rates.

For the surfaces of the façade (external wall of the potroom), convection and sky radiation were considered. A “universal” correlation was (Palyvos 2008) used to determine the convective heat transfer coefficient on windward and leeward walls for different wind speeds. Based on the book of heat transfer (Mills 1999), it is possible to define a sky temperature for radiative heat transfer based on the air temperature at ground level and a sky effective emissivity, $T_{sky} = ((0.727 + 0.0060T_{dp}(^{\circ}C))T(Kelvin)^4)^{1/4}$, with the ambient temperature T and the dewpoint of the air, T_{dp} . The solar irradiation incident on potroom walls was calculated based on the time and solar position. A detailed procedure for its calculation is shown in (McQuiston et al. 2010). Heat sources were applied in each parts of the potroom envelope (e.g. roof at tap side, wall at tap side) to represent the absorbed solar radiation. Finally, all boundaries in the domain, except the openings, were modeled as no-slip wall boundaries.

Table 5.2 Imposed thermal boundary conditions.

Components	Boundary condition, normal pot ventilation	Boundary condition, reduced pot ventilation	Emissivity
Superstructure	440 W/m ²	800 W/m ²	0.8
Pot hoods	800 W/m ²	1250 W/m ²	0.5
Pot bottom	1200 W/m ²		0.8
Pot sidewall	2000-9000 W/m ² , polynomial fits based on experiments		0.8
Inlets	T _{air} = 25°C (scenario 1), 35°C (scenario 2) or 35°C (scenario 3)		N/A
Busbars	85-135°C, depending on the location, from measurements		0.5
Potroom wall	Outdoor convection coefficient: $h_{conv}=7.4+4U_{ref}$ (windward) or $h_{conv}=4.2+3.5U_{ref}$ (leeward); Sky radiation: $T_{sky}=((0.727+0.0060T_{dp}(^{\circ}C))T(K)^4)^{1/4}$ with $\epsilon_{sky}=0.727+0.0060T_{dp}(^{\circ}C)$; Incident solar radiation: equivalent heat sources		

5.3.4 Mesh independence study

Mesh independence was extensively studied both at regions near surfaces and in the bulk domain. In the near-wall boundary layer, different mesh densities were created. For meshes #1 and #2, empirical “wall-functions” were applied to bridge the viscosity-affected region very close to the wall and the fully-turbulent region, and therefore the first cell node is far enough from the viscous-affected region. Six prism boundary layers were created in mesh #1, and 9 in mesh #2. y^+ verification revealed that the value was between 25 and 100 with these meshes, which is within the range of acceptable values for the “wall functions” model to be valid. Mesh #3 has 13 prism boundary layer meshes in which the first cell node is placed in the viscosity-affected area of the boundary layer. y^+ value was verified to be between 1 and 3 on most of the surfaces, which allows the solver to calculate the flow field and heat transfer all the way to the wall surface without using a wall function. A reference scenario was simulated (buoyancy-driven natural convection

with no wind present, with an ambient temperature of 15°C). Table 5.3 provides some of the most important results. It is observed that mesh #1 is good enough to predict the parameters of interest. Therefore, it was chosen in the following simulations.

Then the size effect of bulk volumes in mesh #1 was verified with a maximum size of 0.3, 0.5, and 1 m. The difference in the predicted mass flow rate is less than 4% between the three meshes, and the temperature difference is below ~0.5°C for the air temperature at roof vent, and 2°C for hood surface. However, since the scale of 1 m causes poor resolution on some small structures, such as the hood gaps and pot louvered surfaces, it was decided to retain a scale of 0.5 m for the bulk volume in the final model.

A verification of the discretization settings of the DO radiation model is also required since one of the results of interest is the mean radiant temperature field, which is calculated based on the total incident radiation at a specific point. The accuracy of the predictions of the DO model is strongly related to the number of discretized solid angles, $N_\theta \times N_\phi$. By comparing the predicted mean radiant temperature field in different number settings, local differences between 10 and 20 K were found between $N_\theta=N_\phi=2$ and $N_\theta=N_\phi=4$. On the other hand, when refining the discretization from $N_\theta=N_\phi=4$ to $N_\theta=N_\phi=8$, the local differences of mean radiant temperature were always less than 5 K. Therefore, in order to limit computational times and achieve acceptable results, it was decided to use $N_\theta=N_\phi=4$ for the rest of the simulations.

Table 5.3 Effect of the mesh on parameters of interest.

Parameters	Mesh #1	Mesh #2	Mesh #3
Mass flow rate through roof vent (kg/s)	15.95	15.9	15.85
Ave. temperature at roof neck (K)	305.8	305.9	306
Ave. temperature in potroom (K)	303.3	303.3	303.7
Mass flow rate at inlet 1 (kg/s)	9	8.95	8.9

5.4 Model validation from measurements in potroom

The simulated results were validated with in situ temperature measurements in a potroom. Figure 5.2 shows the positions of the temperature measurements in the potroom. At the duct end, middle and tap end of a given pot, the surface temperature was

measured at 4 points on the hood, 3 on the upper part of sidewall, and 1 on the lower part of sidewall (i.e., 24 data points). Temperature was also measured at two pot cradles for each sidewall position (only one cradle is shown in the figure). Temperature of potroom roof and side walls was measured at 4 locations. Finally, air temperature was measured at the roof vent, and at 3 positions at shoulder-level on the catwalk (the zone between two pots) indicated by red triangles in Figure 5.2. In the end, 34 measurement points were taken as a set of data. This set of data has been measured at 5 different days in order to consider different exterior conditions (i.e., high vs. low wind speed, daytime vs. nighttime, etc.).

A comparison between the CFD results and the measurements is reported in Table 5.4. A positive value means that the CFD result is larger than the measurement, and vice versa. Due to space limitation, only selected results are shown here. Measurement campaign A was done at noon during a sunny day. The wind speed was 5 km/h, based on a nearby meteorological station. Measurement campaign B was performed in a partly-sunny morning, and the wind speed was 10 km/h. The wind direction was perpendicular to the potroom wall at the tap. It is important to mention that due the inherent nature of industrial systems such as the one studied in this work, variability can be quite important. Temperatures is affected by a number of incontrollable elements such as the level of consumption of the anodes, the level of erosion of the refractories and cathodes, the plant operations, etc., and actually varies from pot to pot. In other words, an “exact” agreement between measurements and CFD simulations is not possible, and is actually not sought. The model is used to compare the scenarios with different pot ventilation levels and outdoor wind conditions. The purpose of the validation is to evaluate or quantify the level of agreement between the model and the reality, and to verify that the model can predict adequately the most important trends related to the objectives of this work.

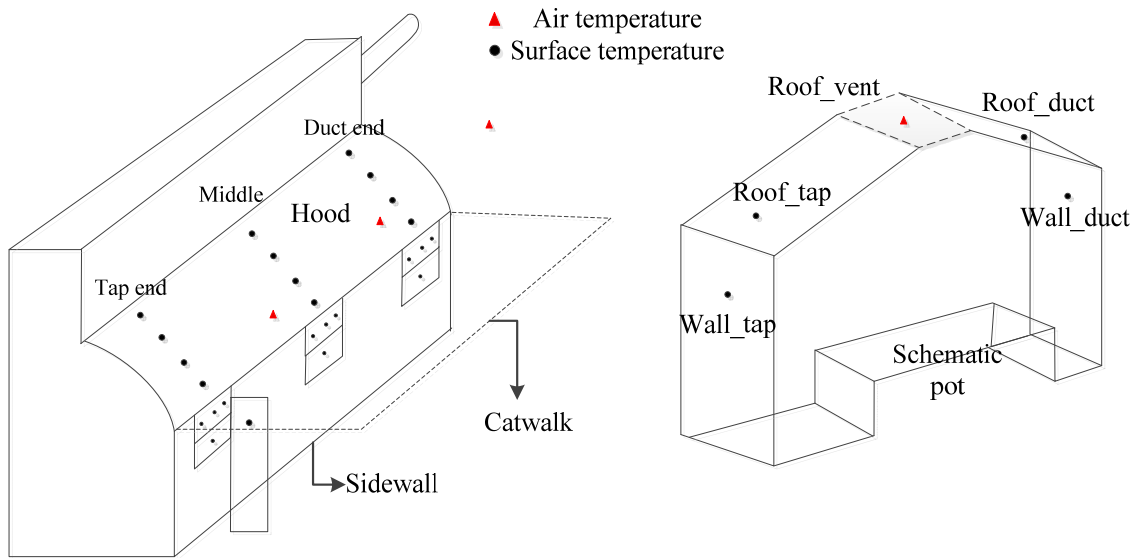


Figure 5.2 Positions where temperature measurements were performed.

From these results, it is seen that a good agreement is achieved in the predictions of the air temperature at the roof vent and above the catwalk, with differences of less than 2°C. Temperatures on potroom walls are also well predicted using the CFD model. Larger differences are found on pot surfaces. This is likely due to the simplifications of the pot geometry and assumed heat flux distribution in the CFD model. For example, hoods are modeled as flat planes, while they actually have a curved shape in reality. Uniform heat flux is imposed on hood surface while it can vary with position and depend on the convection and radiation at both interior and exterior of pot itself. Also, some details of the pot sidewall were not considered in the model. Nevertheless, the temperature difference is still considered acceptable compared with the high temperature on these components (hood temperature: 90-140°C, sidewall temperature: 250-390°C). The ventilated flow rate at roof vent is also compared with the data from ADQ. Due to the high non-uniform gas velocity distribution along the roof vent, an averaged gas velocity was used to calculate the air flow rate through vent. In summer, the real flow rate at roof vent is in the range of 12.4-15.2 m³/s while the simulated results are in the range of 12.3-14.6 m³/s under moderate wind conditions (weak and moderate outdoor winds). Considering the industrial application studied in this work, the results of the CFD model could thus be qualified of adequate.

Table 5.4 Temperature difference between CFD results and measurements, in K.

	Measurement campaign	A	B
Pot at tap	Hood (1 st point counted from top)	5	12
	Hood (3 rd point counted from top)	15	18
	Sidewall top	−15 to −10	−3 to 6
Middle of pot	Hood (1 st point counted from top)	−1	25
	Hood (3 rd point counted from top)	−5	20
	Sidewall top	−20 to 9	−7 to −1
	Sidewall low	8	−30
Potroom walls	Roof tap end	4	−5
	Wall tap end	5	−6
	Roof duct end	−1	−5
	Wall duct end	−3	−2
Air	Air roof vent	−0.5	0
	Catwalk middle	−1	1
	Catwalk tap end	−2	−2

5.5 Ventilation and thermal conditions in potroom under different pot ventilations

As mentioned in the introduction, pot ventilation carries away a huge amount of waste heat from the upper portion of smelting pots. A reduction of the amount of air suctioned in the pot will sacrifice to some extent the amount of heat carried away by the exhaust gases. Therefore, extra heat will inevitably escape from hoods and pot superstructure into the potroom. Zhao et al. (2013) have studied the relationship between the pot ventilation reduction and the distribution of the top heat losses in a smelting pot. Several designs were investigated to maintain a constant top heat loss under different ventilation levels (heat balance is crucial for a stable process). It was found that the total top heat loss could be maintained even if the pot ventilation was reduced to 50% of the normal condition, provided that proper pot design modifications or operation changes are implemented.

However, heat will be redistributed among different components of the pot. In the present work, we study cases in which pot ventilation is reduced by half while the total top heat loss is unchanged. Therefore, proper thermal boundary conditions on pot hoods and superstructure both for the normal and 50% reduced ventilation levels should be properly defined, as shown in Table 5.2. The heat losses from pot sidewalls and bottom are assumed to be unchanged.

5.5.1 Outdoor condition scenarios

The outdoor environmental conditions influence strongly the conditions in the potroom. Therefore, three scenarios were designed to represent different environmental conditions. Scenario 1 assumes that the outdoor air temperature is 25°C, with a 0 km/h wind. In other words, the potroom ventilation is driven only by buoyancy forces. This scenario is valid when the exterior wind is weak (e.g., wind speed smaller than 5 km/h). It is typically a good representation of what happens at the night, when the atmosphere boundary layer is calm. 25 °C is the maximum local ambient temperature at night in summer in the plant considered. Scenario 2 is designed to simulate potroom ventilation with a 5 km/h local wind speed perpendicularly approaching to the potroom wall at the tap end. The outdoor air temperature under this scenario is 35°C. This scenario represents a situation with a very hot environment and moderate wind-assisted potroom ventilation during daytime. Finally, the wind speed is increased to 15 km/h in scenario 3. The outdoor air temperature is still considered to be 35°C. This third scenario represents hot daytime with windy conditions.

5.5.2 Effect of pot ventilation reduction on potroom ventilation

First, the influence of reduced pot ventilation on the potroom ventilation was investigated. The airflow rates through different openings of the potroom (e.g., roof vent, claustra walls and louvered opening) were determined from the CFD simulations, under both normal and 50% reduced pot ventilation levels, see Fig. 5.3a-e. In practice, it is desirable to maintain or enhance the total ventilated air flow from roof vent to provide an adequate cooling of the potroom. In Fig. 5.3a, the mass flow rate at the roof vent is

actually increased by ~ 1 kg/s in all scenarios when 50% reduced pot ventilation is simulated. This can be explained by the fact that the pots dissipate more heat into the potroom as pot ventilation goes down, which actually promotes buoyancy forces and thus induces more make-up air into the potroom. Fig. 5.3b shows the airflow temperature at the roof vent. It is increased by $2-3^{\circ}\text{C}$ under 50% reduced pot ventilation for all scenarios. Figs. 5.3c-e reveal that the mass flow rate experiences no significant reduction through internal openings (<0.4 kg/s) between the two different pot ventilations. However, large variations are found among the different scenarios, i.e. under different wind conditions. It is seen that the ventilated air from the roof vent is suppressed when the outdoor wind becomes significant. The claustra wall at the tap end (windward) introduces much more air into potroom when the wind-assisted ventilation becomes stronger. On the other side (leeward), the direction of the flow is actually reversed through the other claustra wall when the outdoor wind reaches 15 km/h, and cross ventilation between the two lateral inlets occurs. A portion of air coming from the claustra wall at tapping end will leave from the claustra wall at duct end. The air flowing through the louvered plates into the potroom is also suppressed, but to a lesser extent.

It can be concluded that the reduced pot ventilation causes limited changes in the potroom ventilation, while the outdoor wind can significantly influence the ventilation pattern in the potroom. As the wind speed increases, it tends to suppress the ventilation from roof vent and can even create cross ventilation between two inlets at the basement.

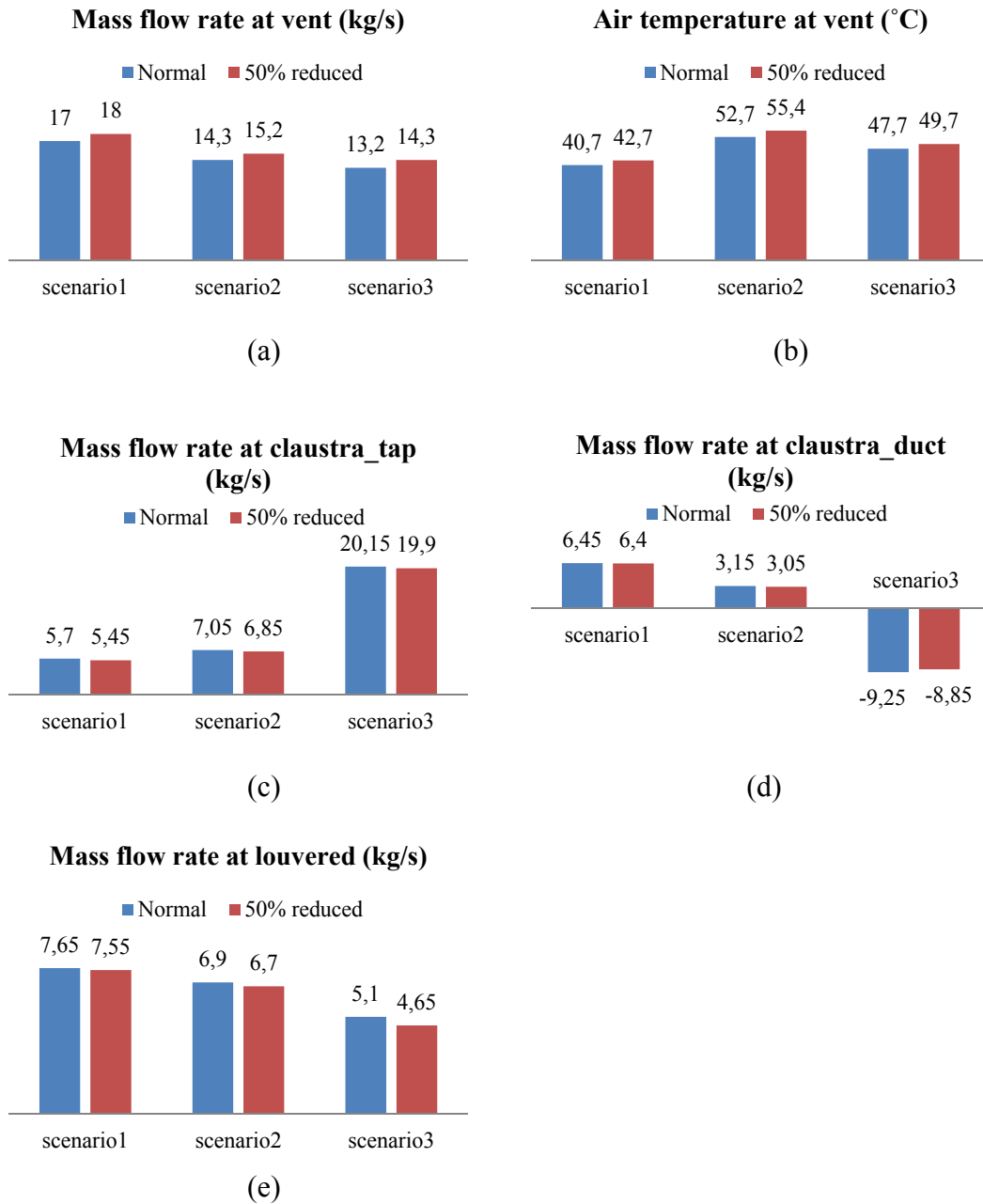


Figure 5.3 Air mass flow rate through different potroom openings under both normal and reduced pot ventilations.

5.5.3 Effect of pot ventilation reduction on temperature distribution in potroom

Another important aspect to consider in reduced pot ventilation is the temperature distribution in the potroom. As mentioned above, pot ventilation reduction results in more

heat being dissipated in the potroom. This could potentially deteriorate the working conditions and reduce overall productivity. Figs. 5.4a-b show the temperature profile in the middle plane between two adjacent pots, for both normal and 50% reduced pot ventilation levels under scenario 1. The maximum air temperature varies from $\sim 41^{\circ}\text{C}$ to $\sim 43^{\circ}\text{C}$. Due to the thermal stratification along the vertical direction, the air is warmer at higher positions such as near the potroom roof, and somewhat cooler at lower positions, such as the area on the catwalk. It means that a reduction in pot ventilation barely increases the air temperature in the area above the catwalk floor. Due to space limitation, only the temperature profiles from scenario 1 are shown, but the same trend holds true for the other scenarios. Overall, the air temperature is increased by $\sim 2^{\circ}\text{C}$ in the potroom when pot ventilation is reduced. The temperature profile on a horizontal surface at a height of 1.3 m above the catwalk is presented in Figs. 5.5a-b for the two ventilation levels. The air temperature in most of the area between two pots is not significantly affected by draft changes. On the other hand, the air is actually hotter near the pot surface under reduced pot ventilation. Note that the spatial variation of air temperature is visible on the horizontal surface. Figs. 5.6a-b show the temperature profiles on hoods and superstructure. Unlike air, pot surfaces become much warmer as pot ventilation goes down. Temperature on the central hood increases from 140°C to 170°C . Since more heat escapes from pot surfaces when less air is exhausted by the pots, this results in warmer pot surfaces.

Another parameter of interest is the mean radiant temperature, which is crucial when evaluating the heat stress and strain experience on workers. Figures 5.7 a-b show the mean radiant temperature fields of a surface which is at a height of 1.3 m above the aisle floor. The radiant temperature can be as high as 105°C even in the normal pot ventilation scenarios. However, it is increased by $\sim 10^{\circ}\text{C}$ when the pot ventilation is reduced by half. Large spatial variation is also observed in the radiant temperature.

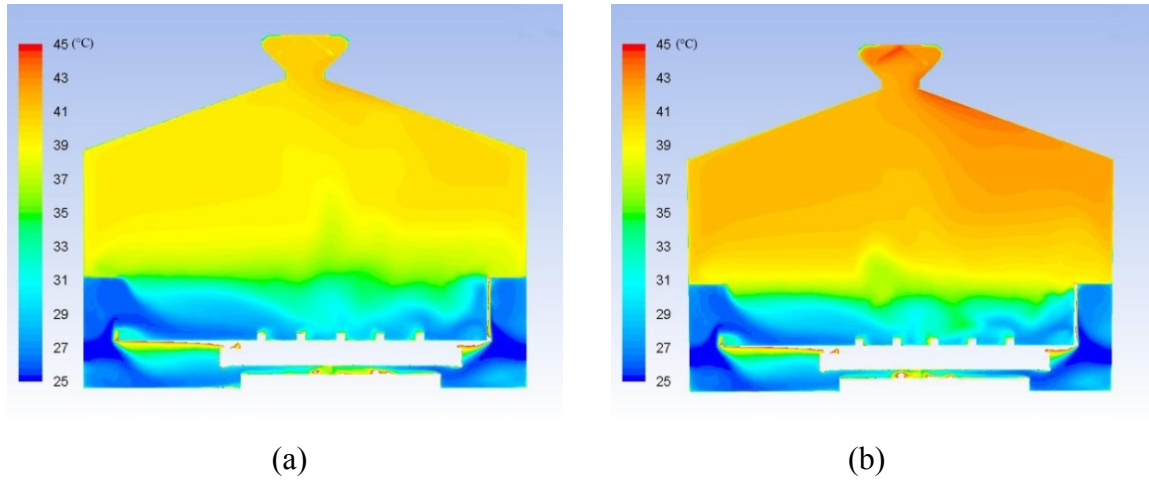


Figure 5.4 Air temperature profile in the middle plane of the sliced potroom under: (a) normal and (b) 50% reduced pot ventilations

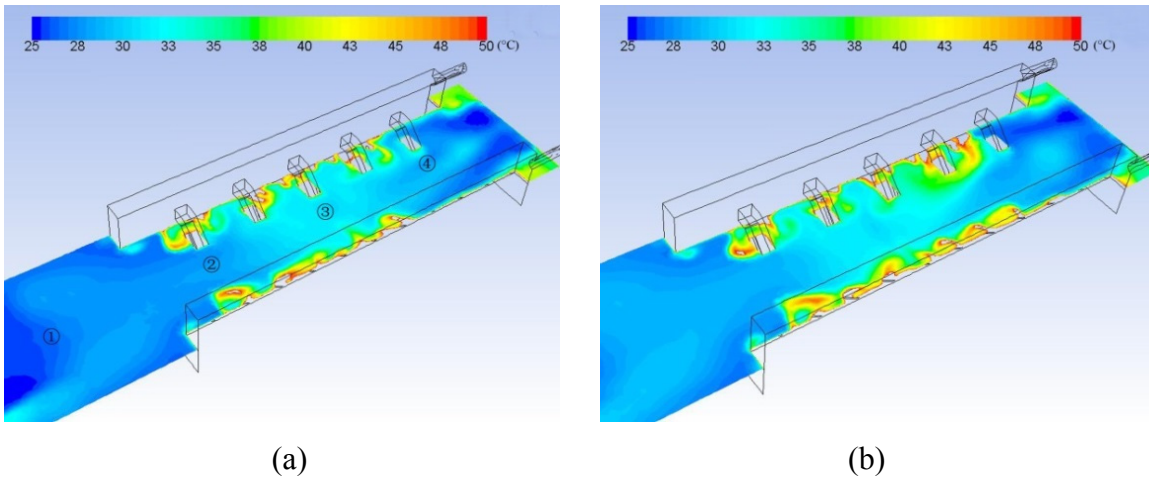


Figure 5.5 Air temperature profile on a horizontal surface at height of 1.3 m above the catwalk floor under: (a) normal and (b) 50% reduced pot ventilations.

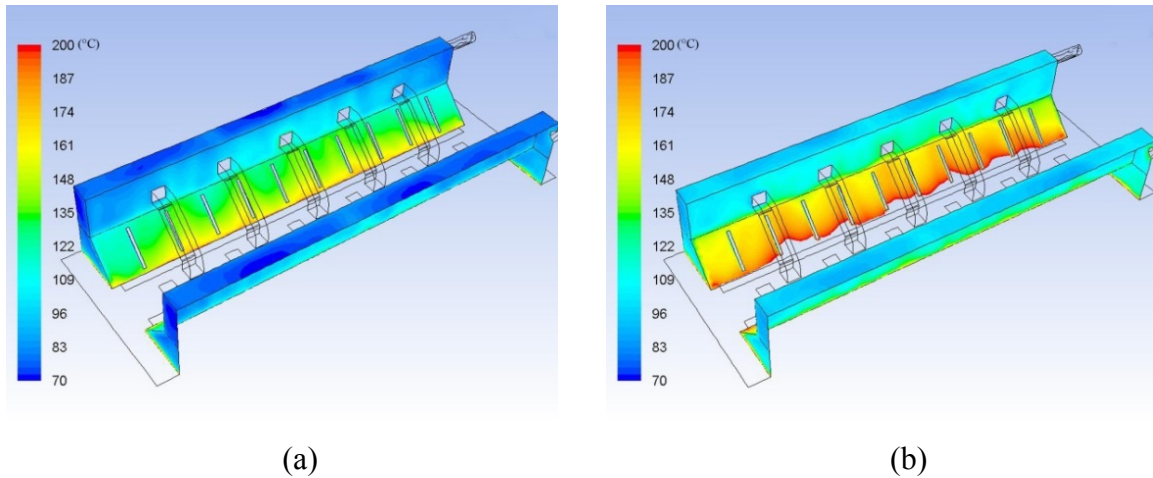


Figure 5.6 Temperature on hoods and superstructure under: (a) normal and (b) 50% reduced pot ventilations.

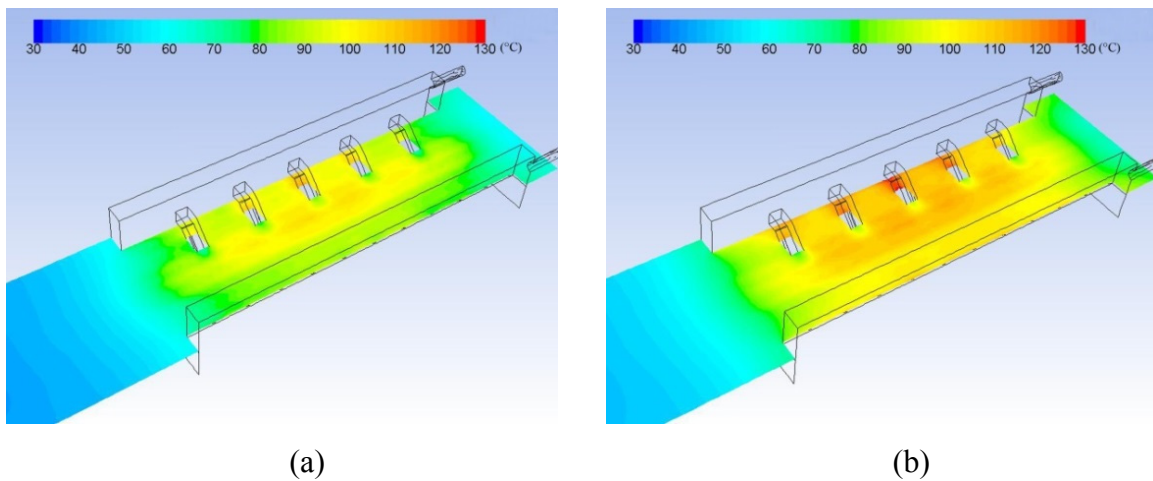


Figure 5.7 Mean radiant temperature on a horizontal surface at a height of 1.3 m above the catwalk floor under (a) normal and (b) 50% reduced pot ventilations.

5.6 Assessment of body heat stress under different pot ventilations

To assess the overall influence of different environmental factors on the thermal comfort of human body, a quantitative method is required. The dry bulb temperature (i.e., the air temperature in potroom) is not the only parameter to consider for maintaining a comfortable environment. For example, thermal radiation from hot surrounding surfaces can increase the temperature of human skin, a high relative humidity (RH) reduces the

heat losses by respiration and perspiration, and so on. In this work, we used the ISO 7933 standard (Parsons 1999) to assess the heat stress in potroom during the hottest time of the year. This standard was chosen instead of more traditional approaches for assessing thermal comfort (e.g., PMV, PPD), since due to its harshness, the potroom environment is far beyond the scope of these comfort models. The method specified in the standard ISO 7933 is based on the calculation of a required sweat rate (S_{req}). The method was developed and modified by continuous efforts both in laboratory and industrial investigations. The idea behind a “required sweat rate” is that this sweat rate is required to maintain the thermal equilibrium of the body in a hot environment. The body energy imbalance E_{req} is:

$$E_{req} = M - W - C_{res} - E_{res} - C_{skin} - R_{skin} \quad (5.6)$$

where M is the metabolic heat generation, W , the mechanical power and normally taken 0, C_{res} , the respiratory heat loss by convection, E_{res} , the respiratory heat loss by evaporation, C_{skin} , the heat exchange on the skin by convection, R_{skin} , the heat exchange on the skin by radiation, and E_{req} , the required heat exchange by evaporation of sweat for thermal equilibrium. Based on E_{req} , the required sweat rate can be established

$$S_{req} = E_{req} / r_{req} \quad (5.7)$$

where S_{req} is the required sweat rate and r_{req} , the evaporative efficiency at required sweat rate.

The calculation required 4 environmental parameters, i.e. air temperature, mean radiant temperature, humidity and air velocity, and two factors related to the activities in the potroom, namely the metabolic rate and insulation of clothing. The environmental parameters are the results obtained from the CFD simulations, except for humidity, which was assumed to be 45% in potroom. This typical potroom RH corresponds to a situation where the exterior RH would be 90% in local summer season, based on psychrometric charts (McQuiston et al. 2010). The metabolic rate for the operators in potroom can cover a wide range (Logan and Bernard 1999). When a worker waits or rests in the walking aisle, his/her metabolic rate is 110 W. When he/she performs pot maintenance on catwalks, 300 W is a good estimation of the body metabolic rate. The insulation of clothing is 0.2 m²·K/W or 1.3 clo which represents the thermal resistance of the mandatory clothing requirement in the plant.

The required sweat rate can be achieved by the person if it does not exceed the maximum evaporative rate of the human body and if it will not cause unacceptable water loss. In such a case, the allowable working time will not be limited by thermal considerations. Otherwise, a duration limited exposure (DLE) can be calculated. It takes into account the maximal heat storage Q_{\max} and maximal water loss D_{\max} for human bodies. In this work, conservative values of $Q_{\max}=50 \text{ Wh/m}^2$ and $D_{\max}=1500 \text{ Wh/m}^2$ were retained. The detailed description of the method could be found in the ISO 7933 standard.

We chose several typical positions both on the walking aisle (rest area, $M=110 \text{ W}$) and catwalk (work area, $M=300 \text{ W}$). The local heat stress was first estimated under normal pot ventilation and for the 3 wind scenarios described previously. The allowable exposure times are presented in Fig. 5.8. The estimated DLE at the walking aisle is not shown in this figure, because the required allowable sweat rate can be achieved in scenario 1, resulting in an infinite DLE in that case. In other words, there is no body heat imbalance in that case. In scenarios 2 and 3, DLE can be as large as 100 minutes and 350 minutes respectively, and it is estimated that the heat stress is not too important at the walking aisle. Therefore, the DLE at the walking aisle will not be considered in the following discussions.

As aforementioned, the temperature and velocity fields vary significantly with the location. As a result, the DLE also changes substantially within the space. The vertical position at which the DLE is calculated was chosen to be 1.3 m above the deck floor (shoulder height). At that height, the maximum local temperatures of air and radiation was used to determine a “conservative” DLE. On the catwalk, DLE evaluations were performed at tap end, middle, and duct end as those for the measurements of air temperature, see Fig. 5.2. It is seen that the required sweat rate cannot be achieved under the considered scenarios, and thus, limited DLE are obtained. In normal pot ventilation, the model estimates that the allowable working time without any risk of heat strain is between 8-16 minutes on catwalk. Comparing among the different scenarios (i.e. different outdoor environments), the DLE is increased by 5-6 minutes when the outdoor temperature goes down from 35°C (summer daytime) to 25°C (summer night). When strong wind is present (scenario 3), the DLE can be increased by 2-4 minutes on the

catwalk. The model indicates that the heat stress in the area between two pots is always high during daytime in summer.

Considering these results, it is important to mention the limitations of the comfort model. The literature (Parsons 1999) mentions that the validity of ISO 7933 could be questionable if the estimated DLE is less than 30 minutes as we have calculated on the catwalk. However, considering the lack of more advanced methods in literature, the present model has the advantage of providing a comparison of the thermal stress in different environments and pot conditions. It should be remembered that the main objective of this work is to verify the changes between normal and 50% reduced pot ventilations.

Figure 5.9 presents the difference of estimated DLE between both pot ventilations in 3 scenarios. It is seen that the allowable exposure time decreases by a maximum of 1.8 minutes in scenario 1, and 0.8-0.9 minutes in scenarios 2 and 3. The relative time drop compared to the DLE in normal pot ventilation varies between 2.5-10%. The variation of allowable time drop between scenarios 2 and 3 is small, 0.1-0.3 minutes, which indicates that the outdoor wind condition only has a limited influence on the internal thermal conditions.

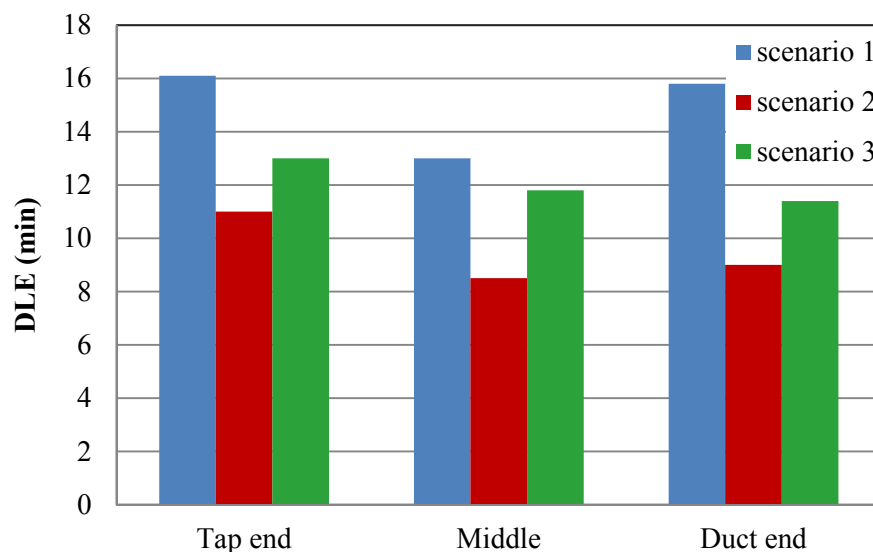


Figure 5.8 Comparison of the estimated DLE in 3 scenarios with normal pot ventilation.

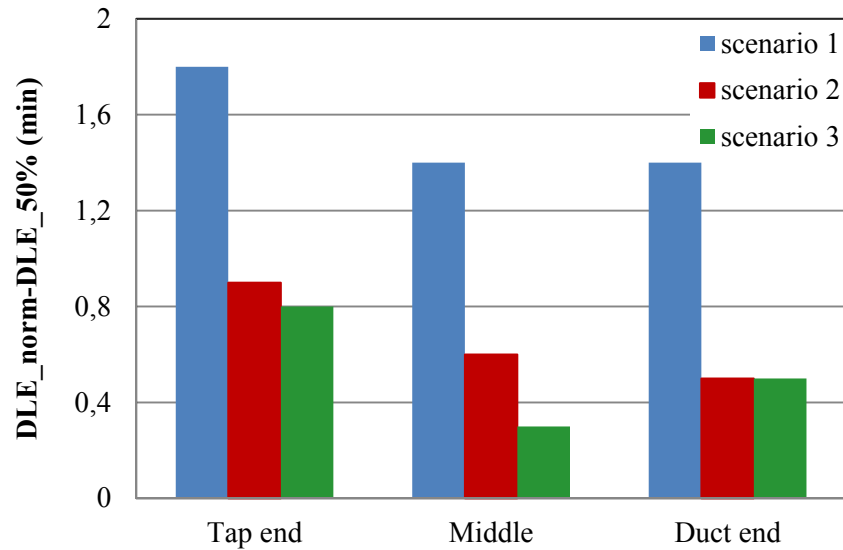


Figure 5.9 Difference of DLE between normal and 50% reduced pot ventilations, in 3 scenarios.

The vertical distribution of heat stress conditions was also assessed by calculating the DLE in scenario 1 and under 50% reduced pot ventilation at different heights, i.e., 0.5 m (legs), 1.3 m (body), 1.7 m (head), as presented in Fig. 5.10. A maximum variation of 1.2 minutes is found along the vertical direction. Normally, the lower position will receive more thermal radiation than the higher position, which causes a shorter DLE. In addition, wind at 5 km/h, but blowing from the duct end, was also simulated. The DLE is not significantly changed. Only the DLE at the duct end is increased by 1-2 minutes. This is because cold air comes from the claustra wall at duct end and provides a better cooling there. Since the radiant temperature remains almost the same, the overall thermal conditions will not be improved significantly.

The presented results have illustrated that the variation of pot ventilation should not significantly influence the heat stress in the potroom, considering that the thermal stress is already high in the working area between two pots.

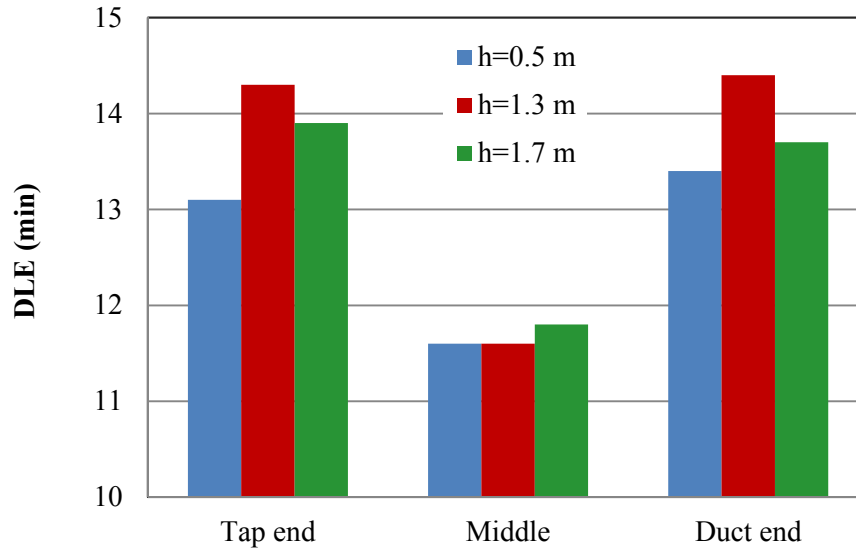


Figure 5.10 Vertical distribution of the DLE in scenario 1, under 50% reduced pot ventilation.

5.7 Conclusions

Potrooms are industrial buildings where electrolytic cells are lined up to carry on the Hall-Héroult alumina reduction process. These buildings are mainly ventilated naturally, based on buoyancy and wind. Therefore, any modification in terms of pot design and operations, as well as in outdoor conditions, is likely to affect the heat transfer and air flow patterns within a given potroom.

This chapter presents a detailed study of the natural ventilation in potrooms by using CFD simulations. Both buoyancy and wind driven forces were considered in the simulations. The advanced model was validated with air and surface temperature measurements performed in the plant. In the end, airflow and temperature fields can be determined from the simulation results. A thermal comfort model was also developed to calculate the duration limitation exposure for operators working in the potroom environment.

In this chapter, the model was used to study, among other things, the impact of the pot ventilation level on the overall ventilation in the potroom, under different scenarios (wind speed, wind direction, outdoor temperature). It was found that the reduction of the pot ventilation level can result in larger heat dissipation rates in the potroom, but that the

effect in terms of DLE is limited for all the scenarios considered. The model that has been developed could be used in the future to study the impact of a variety of other modifications in terms of potroom design.

**CHAPTER 6 ESTIMATION OF THE EFFICIENCY OF POT TIGHTNESS IN
REDUCED POT DRAFT BASED ON CFD SIMULATIONS**

Abstract

Reduction of pot draft is a promising approach for energy saving and waste heat recovery in aluminum smelting cells. Pot tightness, or control of fugitive emissions, is investigated in a smelting cell with reduced draft, down to half of the current level based on CFD simulations. Models with different simulation length scales are created in order to iteratively define proper boundary conditions around the leaking area. A systematic analysis of the pot tightness is presented by considering various factors, e.g., pot draft, hood placement. The results have shown that current pot structure, even within ideal operating conditions, fails to maintain 100% hooding efficiency under a 50% reduced pot draft. Two design modifications are proposed and verified. An efficient sealing is observed when covering the lower half of the gaps between hoods. An estimation of the leaking hydrogen fluoride is made under different scenarios in order to quantitatively verify the modifications.

Résumé

Réduire le taux de ventilation de cuves est une approche prometteuse pour économiser de l'énergie et faciliter la récupération des rejets thermiques. L'étanchéité des cuves, pour contrôler les fuites de gaz, est investiguée dans une cuve avec un taux de ventilation réduit avec un modèle CFD. Des sous-modèles avec différentes dimensions sont créés pour définir itérativement les conditions aux limites. Une analyse systématique de l'étanchéité est présentée pour considérer différents facteurs comme le taux de ventilation et le positionnement des capots. Les résultats ont montré que le design actuel, même avec un parfait positionnement des capots, ne permet pas de maintenir l'étanchéité si on réduit de moitié le taux de ventilation de la cuve. Le scellement du bas de l'espace entre les capots permet cependant d'améliorer l'étanchéité. Une estimation des émissions de HF dans la salle de cuves est proposée.

6.1 Introduction

The current aluminum reduction technology is based on the Hall-Héroult process. An electric current circulates between a carbon anode and a cathode through an electrolytic bath in which alumina is dissolved. The alumina reacts with carbon by a series of electro-chemical reactions, and as a result, carbon dioxide (CO₂) is emitted as a by-product. A liquid aluminum layer accumulates at the bottom of the pot, and can be periodically syphoned out. The overall process can be written in a very simplified and compact formula: $2\text{Al}_2\text{O}_3 + 3\text{C} + \text{electricity} \rightarrow 4\text{Al} + 3\text{CO}_2$. Within the process, only half of the consumed electricity can be converted efficiently. The remaining energy is dissipated into the environment as waste heat.

As the global aluminum industry becomes less profitable and as the cost of energy rises up, producers have to improve process efficiency. Waste heat recovery is an interesting possibility to do that. An energy and exergy balance of the electrolysis process was performed in literature (Nowicki and Gosselin 2012). Several authors have proposed concepts to collect the waste heat contained in pot effluents (Sorhuus et al. 2010; Sørhuus and Wedde 2009; Fleer et al. 2010). Nevertheless, these concepts are still preliminary. Currently, the low temperature of the pot gas (~130°C in summer and ~100°C in winter in a plant such as ADQ (Alcoa's smelter in Deschambault, Québec, Canada)) is a major handicap for an economically beneficial recovery of the waste heat. Zhao et al. (2013a) developed a thermal circuit network to investigate the heat transfer in pots under different scenarios and they found that the reduction of the pot ventilation rate is the most efficient way to rise the temperature of the exhaust gas. Meanwhile, a reduction of the ventilation rate could tremendously reduce the total power requirement of the fans, because the fan power is proportional to the flow rate to power 3. Considering that currently ~2% of a smelter's total electricity consumption (~0.3 MWh/ton Al) is used for the fans, the potential saving is considerable. In addition, the draft reduction will extract less diluted air from the potroom. Since the reduced air suction introduces less moisture into the pots, a reduction of HF (Hydrogen Fluoride) evolution in pot cavity is also expected as a side-effect (Patterson 2002; Meghlaoui 2002).

However, there are number of challenges to address before pot ventilation reduction could be implemented in practice. The gases released by the electrolytic

reactions contain a small portion of hazardous components, among which gaseous and particulate fluoride, and SO_2 . Modern smelting pots are equipped with a pot ventilation system to collect the flue gases. The pot draft condition is chosen to achieve a vacuum in the pot, which results in a virtually leakage free pot. Since the control of hazardous gases is of great importance for the employees' health in the potroom and for environmental reasons, an intensive research has been done to understand the mechanisms of fluoride emissions from pots. The early efforts were mainly devoted to monitoring the HF concentration in the pot exhaust gas under different pot conditions and during various pot operations (Tarcy 2003; Slaughter et al. 2003; Dando and Tang 2005; Dando and Tang 2006). More recently, HF concentration was measured in the pot cavity to determine where HF is released from and to develop correlations between various sources of water and the resulting HF emissions (Osen et al. 2011; Sommerseth et al. 2011). Although literature is abundant in this field, fewer works are available on the pot gas leakage into the potroom. Dando and Tang (2005; 2006) reported the transient measurement of the HF concentration profile in the area just above pot hoods in different pot conditions. It was found that the thermal buoyancy from crust holes and the air leakage of the pneumatic system of the alumina feeding system are the two main reasons explaining HF release from pots when the hoods are into place. In addition to experiments, analytical models were developed to calculate the pot draft and to investigate pot hooding efficiency (Dernedde 1990; Karlsen et al. 1998). These models considered the flow infiltration through pot gaps due to natural and mechanical ventilations in the pot, but they were too simple to provide accurate results.

Computational Fluid Dynamics (CFD) simulation has been used over the last decades for simulating the ventilation in built environments. It was also employed to predict the air ventilation and HF distribution in aluminum smelting potrooms (Berkoe et al. 2005; Vershenya et al. 2011), i.e. the building where the pots are aligned. CFD simulations of fugitive emissions from aluminum smelting pots were realized in (Abbas et al. 2009). The model was built to predict the fugitive emissions in both normal and reduced ventilation conditions. It was estimated from CFD models that the pot could remain free of leakage until the pot ventilation is reduced to 10% of normal condition, although this conclusion seemed to be inconsistent with the measurements of HF in

potrooms. In addition, the CFD model only considered a pot under ideal operations (good crust integrity and perfect placement of hoods).

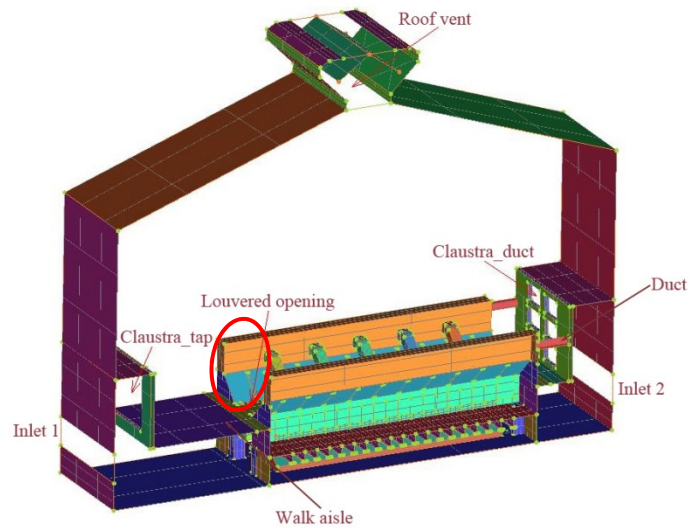
The main leakage of fluoride species occurs during pot operations, e.g. removing two or three hoods for anode change and opening the end door for aluminum tapping. In some smelters, a temporary high-draft ventilation is imposed to enhance the vacuum in pot during pot operations and thus limit the fluoride emissions. HF can also be emitted from pot gaps even when no operations are taking place, with the pot covered appropriately with hoods. Such emission is called “background fugitive emission” and accounts for 20-30% of total emissions in a potroom (Aljabri et al. 2003). In fact, the background emission is directly influenced by the pot draft condition and pot tightness. However, the literature review revealed few numerical analysis of the background fugitive emission in current pot ventilation, let alone under tentatively reduced conditions. In the viewpoint of practice, the background fugitive emission is influenced by several factors, i.e. pot draft condition, pot openings, crust condition and exterior airflow condition. No study was found in literature on the influence of the exterior wind on the pot tightness and fugitive emissions.

In this work, we develop a CFD model to study the factors influencing the background fugitive emissions and to verify the hooding efficiency of current pot structure in tentatively reduced ventilation rates. A reduced pot draft condition is also investigated in the present work. Modifications in pot structure are proposed. The objective is to reduce the pot ventilation rate by half and to enhance the thermal quality of the waste heat in pot exhaust gas, while maintaining hooding efficiency to prevent fugitive emissions into potroom.

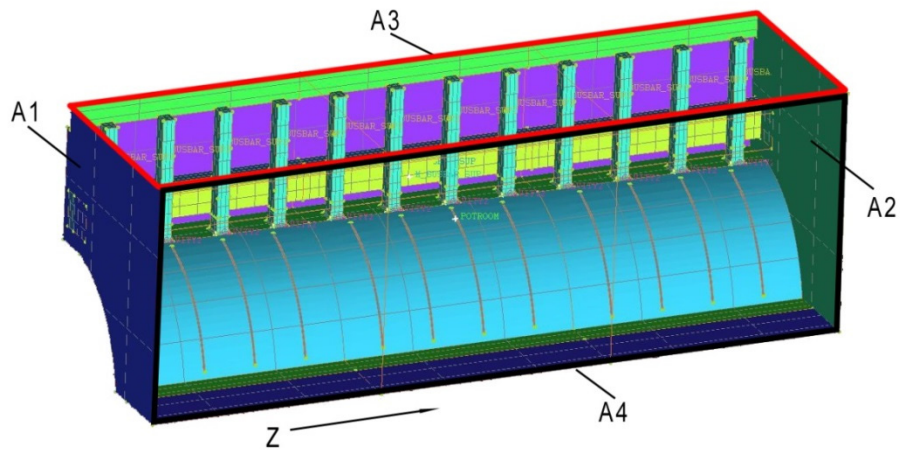
6.2 Description of pot ventilation principles

The potroom can be viewed as a two-storey building, as shown in Fig. 6.1a. The lower floor is the basement, where cooling air is introduced from the openings on the two long façades of the building. Once air comes in, it goes into the potroom (the upper floor) through several inner openings, such as perforated walls on the lateral sides and louvered plates in the floor between consecutive pots. The air captures heat from pot surfaces, and is thus driven upward due to the buoyancy forces. A portion of the warmed air is

exhausted through the vent at the roof while the remaining flow forms circulation loops in the potroom. A certain amount of air is taken into the pots through small gaps on hoods and pot superstructure. A negative pressure is maintained in the pots to avoid releasing hazardous gases into the potroom environment.



(a)



(b)

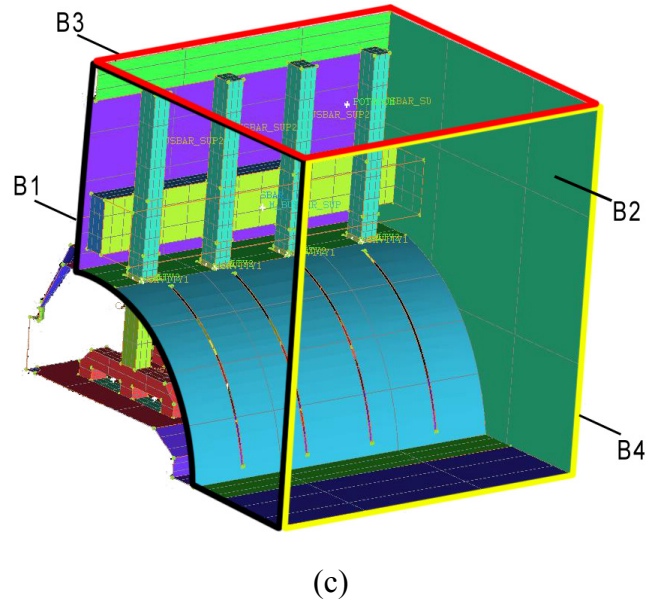


Figure 6.1 Three CFD sub-models considered in this work: (a) potroom model; (b) sliced pot model; (c) a 3D slice of potroom.

The pressure at the interior and exterior of the pot can be schematized as in Fig. 6.2, where we assumed a constant air density to illustrate the hydrostatic pressure as a function of the vertical position. In other words, to draw the interior pressure line in Fig. 6.2, one would consider the density based on the average temperature in the pot, and similarly for the exterior pressure line. $P_{i,nat}$ is the internal pressure in a situation where only buoyancy creates ventilation in the pot cavity under hoods, while $P_{i,mec}$ is for the situation where mechanical ventilation also works at the gas collecting duct. Once air is exhausted out by the ventilation system, the internal pressure is reduced and the corresponding line in Fig. 6.2 shifts to the left. The higher the ventilated flow rate, the more the internal pressure shifts to the left. The gap space and the heat released from the bottom of pot cavity can also influence the distance between the two pressure profiles. In addition, the flowing air at the exterior can change the local external pressure, as mentioned in Section 6.5.3. From the pressure lines in Fig. 6.2, it is apparent that gas leakage is most likely to happen at the top of the pot cavity when the internal and external pressure lines cross below the top of the pot.

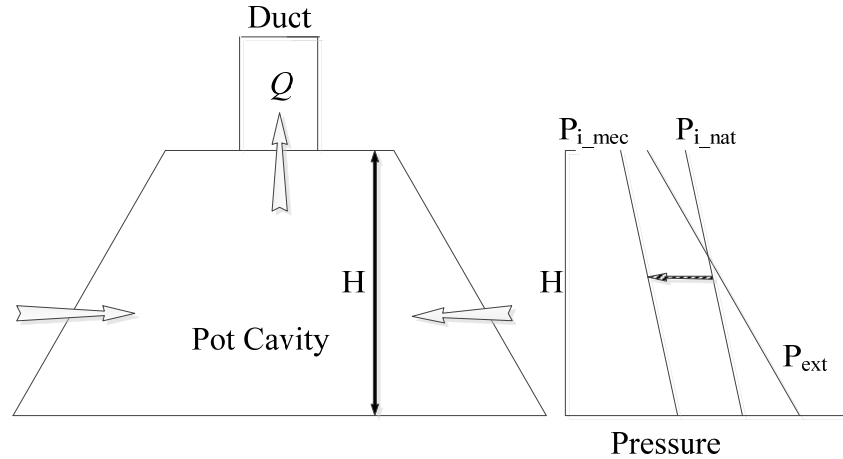


Figure 6.2 Schematic representation of the pressure difference distribution along the hoods.

Although the above analysis is useful to understand how pot leakage can occur, CFD provides a much more realistic model where the temperature-dependent gas properties and the 3D gas pressure distribution can be directly calculated and the gas leakage can be locally tracked.

6.3 Numerical model

6.3.1 Computational domains and simplifying assumptions

The CFD simulations performed in this work involve different lengthscales, ranging from the small gap width between hoods (2 to 6 cm) up to the potroom with dimensions of the order of 10 m. A good grid resolution is required in the pot gaps in order to accurately capture possible gas leakage through the gaps. Considering the trade-off between the actual geometrical representation of the domain and the corresponding computational efforts, two CFD models with different computational domains were built to simulate the pot ventilation in both potroom and pot cavity. Fig. 6.1b represents a potroom space that is surrounded by a quarter of a pot superstructure and also includes 12 anode rods and a horizontal beam. The domain height is 2.8 m, counted from the walking floor and its width reaches to the middle plane with the neighboring pot. This model is referred to as the *potroom model* in the following sections. The model in Fig. 6.1c consists of a 1/10th pot cavity under hoods (including 4 anode assemblies) and the corresponding potroom,

named later the *sliced pot model*. The overall simulation procedure starts by performing a simulation in the *potroom model* to determine the flow field and heat transfer patterns in that zone (e.g. velocity, static pressure, turbulent parameters, air temperature, etc.). Then, depending on the pot segment of interest, the flow information at different cross-section surfaces is extracted from the *potroom model*, and introduced into the *sliced pot model* as boundary conditions. The second simulation is performed in the pot model which can predict the coupling between the pot interior and exterior at the gaps. In both models, we made the following simplifications in order to focus on the issues of interest and facilitate the simulations:

- Only half of the area between two pots is included in the models and the surface A4 (depicted by thick black lines) in Fig. 6.1b and B4 (thick yellow lines) in Fig. 6.1c are treated as symmetry planes. In fact, there are 4-5 anode busbars standing in this area and connecting to the pot at one side. The real flow could be influenced by these obstacles. However, they are normally installed at a distance of 0.3-0.4 m away from the pot shell and the influence of the busbar is limited compared to other parts, such as anode rods and supporting beam.
- Other trivial structures and parts, such as connecting pieces, are ignored in the models in order to minimize the required number of control volumes.
- The geometry of anode assemblies is represented by more regular shapes in order to create a mesh with good quality.
- Only the gaps around anode rod and between hoods are modeled while the gaps between the hoods and the superstructure's horizontal plate are ignored, because they are very small compared with the other considered gap areas.

6.3.2 Governing equations

The conservation equations for mass, momentum, and energy are discretized and solved in the commercial CFD code, ANSYS FLUENT 14.5, via the finite volume method. Steady-state conditions are considered. Pressure work and kinetic energy variations are neglected in the energy equation since the gas is treated as incompressible. No species diffusion is simulated in the problem. Therefore, the governing equations (conservations of mass, momentum and energy) are written as follows:

$$\frac{\partial(\rho u_i)}{\partial x_i} = 0 \quad (6.1)$$

$$\frac{\partial(\rho u_i u_j)}{\partial x_i} = -\frac{\partial p}{\partial x_i} + \frac{\partial}{\partial x_j} \left(\mu_{eff} \left(\frac{\partial u_i}{\partial x_j} + \frac{\partial u_j}{\partial x_i} \right) - \frac{2}{3} \rho \delta_{ij} K \right) + \rho \vec{g} \quad (6.2)$$

$$\frac{\partial(\rho u_i h)}{\partial x_i} = \frac{\partial}{\partial x_i} \left(k_{eff} \frac{\partial T}{\partial x_i} \right) + S_h \quad (6.3)$$

where the sensible enthalpy of the gas h is defined as $h = \int_{T_{ref}}^T C_p dT$. C_p is the temperature-dependent heat capacity of air. The Reynolds stresses term due to the turbulence is modeled based on the Boussinesq eddy viscosity assumption. Therefore, μ_{eff} is the effective viscosity (i.e., $\mu + \mu_t$, where μ_t is the turbulent viscosity, defined according to the turbulence model that is used), K is the turbulent kinetic energy and $\delta_{ij}=0$ ($i \neq j$) or 1 ($i=j$). k_{eff} is the effective thermal conductivity (e.g., $k + k_t$, where k_t is the turbulent thermal conductivity, defined according to the turbulence model being used). S_h includes the volumetric heat source due to the Joule heating effect in solids where a current passes, such as in the anode assembly. The volumetric heat generation (Joule heating) is assumed to be uniform in the solids and was calculated based on the typical current and resistivity in each part of the anode assembly. Viscous heating is ignored in the simulation. Note that in the solids, only the energy equation is solved, without the advective terms.

The air properties (i.e., specific heat, thermal conductivity, and viscosity) are user-defined functions with respect to temperature (polynomial fittings based on data published in (Bergman et al. 2011)). The air density is determined based on the “incompressible-ideal-gas” model of the CFD code used (Fluent 2012), which is defined as:

$$\rho = \frac{P_{op}}{\frac{R}{M_w} T} \quad (6.4)$$

where R is the universal gas constant, M_w , the molecular weight of the gas, and p_{op} , the defined operating pressure normally representing the mean pressure in the computational domain. The density, defined by Eq. (6.4), depends only on the local temperature field,

and thus buoyancy forces can be considered in the momentum equations. The Boussinesq assumption for the air density was not used in the work, since its validity is questionable in the case of large temperature differences as experienced in pots and potrooms (Zhao and Gosselin 2014).

A proper choice of turbulence models should be made to achieve a trade-off between accuracy and computational time. The flow pattern in pot and potroom shares many similarities with the ventilated airflow around and in buildings (e.g., jet flow through hood gaps, flow impingement on surfaces, and both natural and mechanical ventilation). The two equation eddy-viscosity turbulence models are widely used in the simulations of air ventilation and heat transfer in buildings, particularly when the time-averaged parameters, e.g. averaged velocity, pressure, and temperature, are of interest in the simulations.

The SST $k-\omega$ model applies the $k-\omega$ model to simulate turbulence in near wall area and it gradually converts to the standard $k-\epsilon$ model when the modeling flow goes away from wall. When modeling the flow in the near wall region, the central point of the first mesh layer should be placed in the viscous sublayer, i.e. $y^+ < 5$. At least 10 cells are required to accurately resolve the flow boundary layer near wall. The SST $k-\omega$ model also accepts a coarse boundary mesh ($y^+ > 25$) and applies empirical formulas (i.e. wall functions) to resolve the viscously-affected region. However, it is recommended to avoid to place the central point of the first mesh layer in the transitional layer ($5 < y^+ < 25$) although such mesh can be solved in the SST $k-\omega$ model. In this work, a hybrid mesh scheme is used to resolve different areas. Prism meshes are created in the near wall region and tetra meshes, in the bulk area. Different mesh scales are used depending on the local flow characteristics. Thin prism layers are paved on the surfaces of pot superstructure and the surfaces surrounding the pot cavity under hoods, because the nearby flow exhibits the features of a low Reynolds flow. They are either driven by mixed convection or circulating around obstacles. Therefore, 10 prism layers are created to resolve the flow boundary layer near wall and the first layer thickness satisfies the requirement of $y^+ < 5$. The maximum mesh size in the pot cavity is 0.05 m while it can reach 0.2 m in the potroom for both the *potroom model* and the *sliced pot model*. Attention should be paid to some specific areas. For instance, the control volume side

length is as small as 0.005 m in the area near the gaps between anode rod and pot superstructure, since a good resolution is required to determine whether there is an exfiltration of pot gas from the gap. Small mesh is also required at the exterior and interior of the gap space between hoods in order to solve jet flow through it. The *potroom model* contains approximately 4.5 million cells and the *sliced pot model*, 6 million cells. Finer meshes were tested and did not change significantly the results, as will be described later.

The entire fluid domain is treated as a non-participating material in terms of radiative heat transfer. Discrete Ordinates (DO) model is used to calculate surface-to-surface radiation heat transfer, considering the possibility to implement it with parallel calculations in the software used. Default values are used in setting the parameters of angular discretization and pixelation of space.

The two models are solved in steady-state condition and the gravitational acceleration, g , is gradually increased from 0.1 m/s^2 to 9.81 m/s^2 to facilitate convergence. The method to interpolate the variable gradient is the least squares cell-based gradient evaluation. The interpolation scheme of surface pressure between two cells is PRESTO! which is suitable for flows with high swirling and high Rayleigh number (buoyancy driven flow) (Fluent 2012). Pressure-velocity coupling is achieved by using SIMPLE segregated algorithm. All of the other variables are interpolated with the second-order upwind scheme except for radiative intensity, which is calculated via the first-order upwind scheme because the air is considered as a non-participating medium and the optical thickness is therefore zero in the radiation transport equation. Default under-relaxation factors are retained, except that for momentum equations which had to be reduced for a better convergence. Default values of the scaled residuals are considered to declare convergence. The CFD models are solved in parallel with 4 processors, each having frequency of 3.40 GHz. It takes approximately 20 hours to run one simulation of the *potroom model* and 30 hours for the *sliced pot model*.

6.3.3 Boundary conditions

For the *potroom model* (Fig. 6.1b), a velocity inlet is imposed on the surface A1, while a pressure outlet is used for the surfaces A2 and A3. A4 is treated as symmetrical surface.

In Fig. 6.1b-c, some boundary surfaces, such as A3, A4, B1, B3 and B4, are depicted by thick boundary lines with different colors, in order to show well the internal structures in the two models. The required information (air velocity, pressure and temperature) is obtained from the simulation results from an upper-level model (Fig. 6.1a), which was developed for simulating the potroom ventilation (Zhao et al. 2014). Due to the influence of outdoor environmental conditions (e.g., outdoor air temperature, outdoor wind), different profiles can be extracted at a cross-section surface (marked by a thick red circle) and used as inputs into the surface A1 of the *potroom model* to consider the environmental effects on the flow pattern around pot superstructure. Three wind speeds, representing calm (0 km/h), medium (10 km/h) and strong wind conditions (20 km/h), are studied. Velocity magnitude and direction is imposed at the louvered opening based on the real geometry of the louvered plate (obtained from (Zhao et al. 2014)). In addition, a no-slip condition is considered on the superstructure wall and on the concrete catwalk. Two sets of heat fluxes, corresponding to two scenarios of different pot ventilation levels (i.e., 2.4 Nm³/s vs. 1.2 Nm³/s), are imposed on both the pot superstructure wall and pot hoods, because pot heat loss is varied with the pot draft conditions. The gap between hoods is set as a pressure outlet and governed by a user-defined pressure distribution, which is interpolated from an analytical model considering both natural and mechanical ventilation in the pot cavity and with a prescribed constant air density. The Joule heating in anode busbars is represented by a constant heat source of 7000 W/m³ (manually calculate based on the operating conditions).

The boundary conditions in the *sliced pot model* are related to two simulated domains: pot cavity under hoods and a portion of potroom. In the pot cavity, variable heat fluxes are imposed on the crust surface, depending on the crust location. The heat flux on the crust just covering carbon anode (2000 W/m²) is normally higher than that on the crust in side-channel (1500 W/m²). A total mass flow rate $\dot{m}_{hotgas}=0.005$ kg/s obtained based on the balance of aluminum consumption in the electrolysis reaction is defined at the two 1/4 feeder holes to represent the hot gases (mainly CO₂ that is approximated here as air in the CFD simulations) released from the bath. The stub bottom surface is at a fixed temperature of 450°C. Negative pressure is imposed at the outlet of the model (i.e., the inlet of collecting duct) and its value can be “adjusted”, depending on the pot

ventilation that one wants to simulate. Joule heating in anode yoke and stubs is treated as a constant heat source of $12,000 \text{ W/m}^3$. Effective outside convection is used on the surfaces of pot superstructure that are not connected to the potroom domain. The boundary types of the potroom domain are the same as those in the *potroom model*. Specifically, a velocity profile extracted from the results of the *potroom model* is imposed at the surface B1. By using the velocity profile extracted from the surfaces at different z positions of the *potroom model*, the simulation of the sliced pot representing different segment of a smelting pot can be performed. Boundary conditions on the other surfaces (e.g. B2, B3 and B4) are the same as those in the *potroom model*.

6.3.4 Mesh independence study

A mesh independence study is performed in order to verify the errors due to grid discretization. The boundary layer mesh in near-wall region is verified by comparing the results achieved with a reference mesh (with 10 prism mesh layers) to those obtained with a denser mesh (with 14 prism mesh layers). In both cases, the thickness of the first layer is only 0.0008 m, which makes y^+ value smaller than 3 in most areas. The discrepancy between the two meshes in terms of predicted air temperature at the outlet is within 1°C ($T_{air} \approx 120^\circ\text{C}$), with a variation of the ventilated mass rate changes of less than 1.5%. The average temperature on the surface of hoods and anode rods changed by only 2 to 4°C . Therefore, the boundary mesh with 10 prism mesh layers is used in the following study.

The length scale of control volumes in the bulk of the pot cavity and potroom was gradually reduced to determine a proper size for the simulation. It was found that 0.05 m in pot cavity and 0.2 m in potroom for both *potroom model* and *sliced pot model* yields a good trade-off between simulation accuracy and computational efforts. Finer meshes were considered and did not affect significantly the monitored parameters.

6.4 **Model validation**

The numerical model was validated by comparing different measurements performed at the ADQ plant to the results of the model.

First, a series of temperature measurements was performed on pot surfaces and in the potroom. Surface temperature was measured in 24 positions on pot shells and 4 positions on building walls. Air temperature was also measured at 3 positions at shoulder-level between two consecutive pots. This series of measurements was repeated 5 times for different weather conditions. The CFD model was used to simulate these conditions. It is found that the model could accurately predict the temperature distribution. A maximal discrepancy of 25°C is found for the surface of the pot shell (on average the difference was below 10°C) and 6°C for the potroom walls. The maximal discrepancy for air temperature is even less, about 2°C. These values are considered acceptable, compared with the high surface temperatures (hood temperature: 90-140°C, sidewall temperature: 250-390°C, potroom walls and air temperatures: 15-50°C) and considering the geometrical simplification of the CFD model.

Additionally, the mass flow rate at the roof vent, which was measured at the plant, was compared to the one achieved in the simulations. In summer, the real flow rate at the roof vent is in the range of 12.4-15.2 m³/s while the simulated results are in the range of 12.3-14.6 m³/s under moderate wind conditions (weak and moderate outdoor winds).

Another comparison was made between the measured static pressure in the pot cavity and the simulated results. The sensor was positioned under one hood located in the middle of a cell and the pressure was measured at different heights (from the bottom of the pot cavity to the middle height of the pot cavity) and varied between -6 Pa and -12 Pa. Under the same pot ventilation rate and hooding conditions, the simulated pressure is well stratified in the vertical direction. The pressure is as low as -8 Pa in the side channel just above anode cover and it is about -6 Pa in the middle height of the pot cavity. A large discrepancy is observed in the lowest position of the pot cavity, because the real situations may be different than the ideal conditions of the simulation (e.g. the surface profile of the anode cover, the emission of hot gases from the openings on anode cover, etc.). Nevertheless, the pressure profile agrees relatively well in the rest of the cavity where the influence of the uncertain boundary situation mentioned above is minor.

Finally, the results of smoke tests that had been done in the potroom were also used to validate the main flow patterns, at least in a qualitative way. The comparison between the smoke tests and the model was good, and all the main features observed

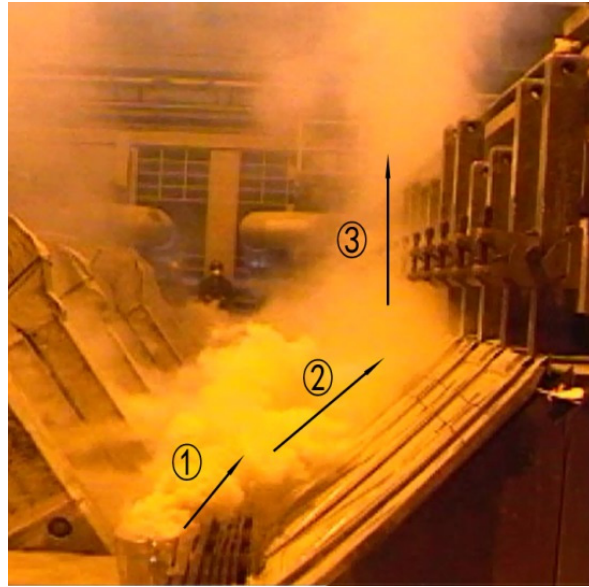
during the smoke tests were predicted by the model. For example, smoke tests have revealed the vortex (arrow 1 in Fig. 6.3a) where the air is going over the edge of the pot end, as well as the plume shape above the pot (arrow 3 in Fig. 6.3a). Also, the smoke tests showed the creeping flow along pot hoods (arrow 2 in Fig. 6.3a), where air is flowing up all the way to the top of the pot. These flow structures were also revealed by the CFD simulations. The vortex flow is clearly seen in the similar position of Fig. 6.3b, which is the flow pattern in the *potroom model*. The flow near the hoods and pot superstructure is also consistent with the smoke tests. Fig. 6.3c is the flow pattern in the *sliced pot model*, representing the middle section of a pot. The creeping flow on pot hoods and the uprising flow along pot structure were well predicted by the model. Considering the industrial application studied in this work, and the purpose of this work, the results of the CFD model could thus be qualified of adequate.

6.5 Pot tightness in various pot conditions

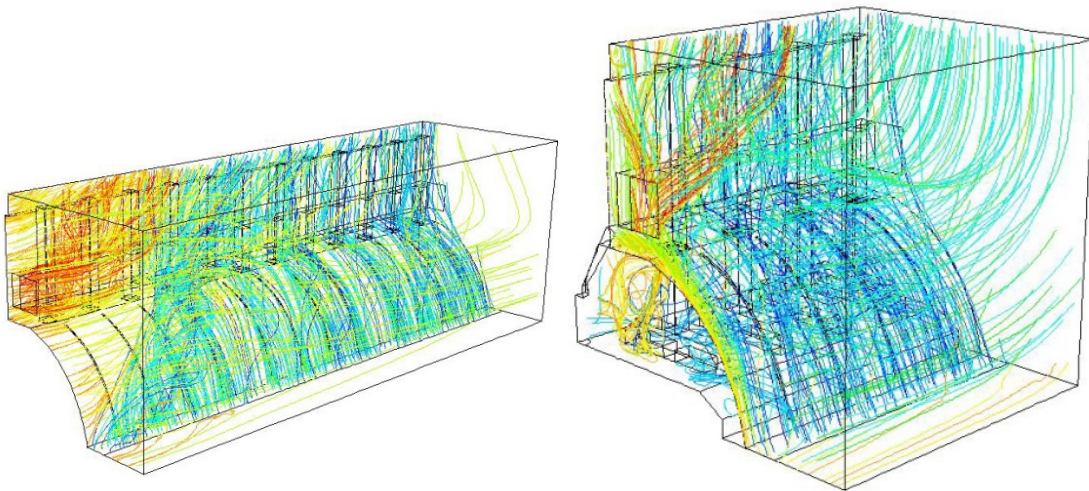
In this section, different factors that influence the pot tightness are studied with CFD simulations. The pot ventilation rate is one of the most important parameters to determine the negative pressure in the pot cavity in order to avoid leakage. A higher draft condition demands a higher vacuum, and vice versa. The gap width between two neighbouring hoods is another factor that significantly controls the suction rate of potroom air into the pot cavity. A loose placement of hoods due to the hood deformation or incautious manipulations may cause a significant reduction of vacuum in the pot and allow fugitive emissions. Another factor influencing leakage relates to the air flow pattern itself. For example, the air in the potroom blows over the shell of pot superstructure and may impose either positive or negative pressure (depending on the flow direction and the structure itself) on the external surface of pot superstructure. Finally, the release of pot gas from crust openings could also increase the risk of leakage. These factors are studied in the next sub-sections.

6.5.1 Effect of different pot drafts

The pot draft condition is adjustable in the numerical model by specifying different pressures at the outlet of the *sliced pot model*. A series of simulations were



(a)



(b)

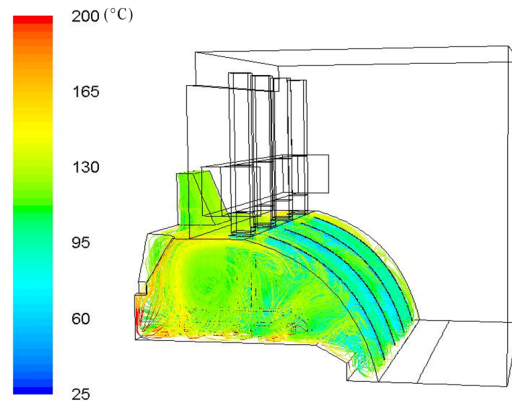
(c)

Figure 6.3 Comparison of flow patterns between smoke tests and CFD results, (a) airflow in smoke tests; (b) airflow streamlines in the *potroom model*; (c) airflow streamlines in the *sliced pot model*.

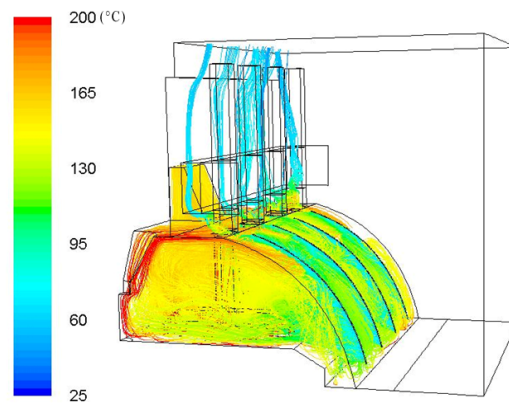
performed with a gradual reduction of the pot draft from normal level down to 50% reduced lever. We assumed that the other parameters are as in the reference case, i.e. the width of hood gaps equal to 0.02 m, a good crust integrity (no open holes in crust except for the feeding holes), and a medium wind flowing from the tapping end. The objectives

of this parametric study are two: 1) to determine at which draft level the current pot structure with ideal pot conditions can retain a 100% tightness and 2) to estimate the fugitive emissions (if any) in a 50% reduced draft condition, which is the “objective” pot draft for potential waste heat recovery applications.

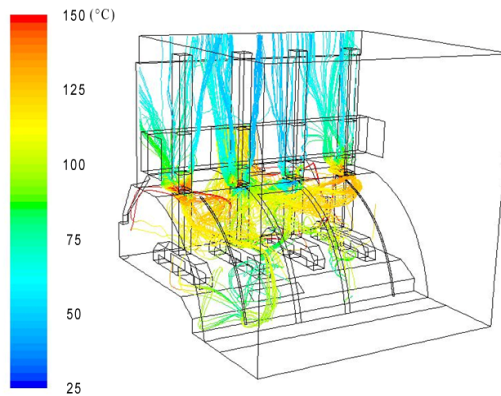
From the simulation results, the fugitive emissions from different pot gaps can be visualised by tracking the flow pathlines through the gaps. Under the normal pot draft (i.e. $2.4 \text{ Nm}^3/\text{s}$), there is no leakage at the pot openings (Fig. 6.4a), which indicates that a good pot tightness is present in the pot. Pot gas starts to leak out when the draft is reduced to ~65% of the normal level. Under 50% reduced draft condition, a significant leakage happens at the gaps between the horizontal plate of pot superstructure and the anode rods (Fig. 6.4b). As the pot draft is reduced, the vacuum in the pot cavity is significantly decreased. Meanwhile, buoyancy in the pot cavity induces a monotonically increase of pressure with the vertical position. Under the combined effects of the fan system and buoyancy, the area just beneath the superstructure horizontal plate exhibits the larger pressure difference and allows the fugitive emissions on the pot gaps around anode rods. Pressure profiles under normal and 50% reduced pot drafts are depicted at a specific cross-section of the *sliced pot model* in Fig. 6.5a-b. The reference pressure, namely zero pressure, refers to the pressure in the core area of potroom. It is shown that the pressure at the bottom of the pot cavity (the area just above anode crust) is as low as -5 Pa under normal pot draft and the pressure is still at approximately -2.5 Pa in the area beneath the superstructure horizontal plate. There is a distinct pressure difference between the interior and exterior of the superstructure plate. This pressure difference guarantees that the flow is always entering into the pot, not out. However, the vacuum level is tremendously decreased under 50% reduced pot draft and the internal pressure below the superstructure plate is only -0.5 Pa , which cannot guarantee a negative pressure difference between the interior and exterior (external pressure is not always positive, see Section 6.5.3). The results suggest that the current pot structure, even in ideal pot conditions, is unable to maintain good tightness in 50% reduced draft condition, and modifications would be required to enhance the pot tightness.



(a)

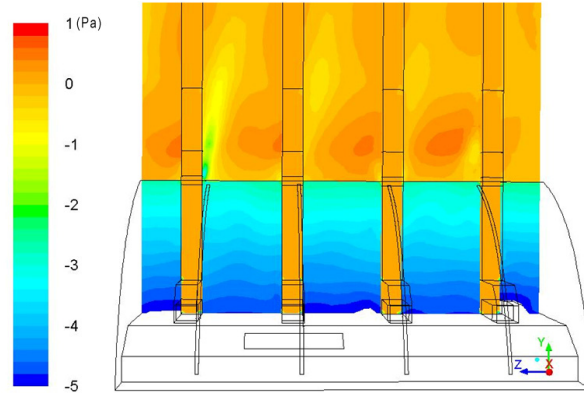


(b)

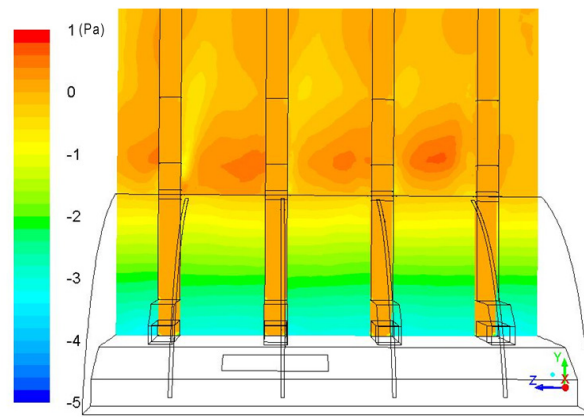


(c)

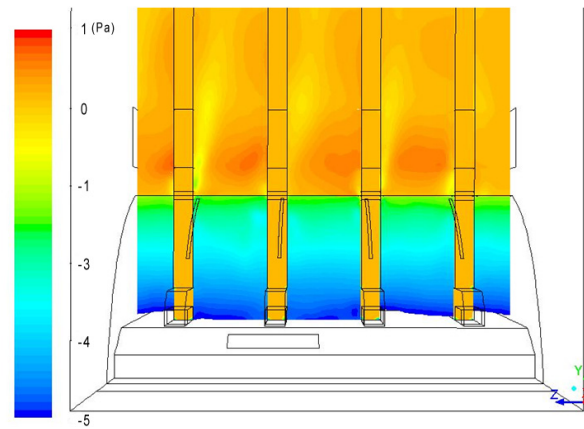
Figure 6.4 Flow pathlines starting from the hood gaps under different scenarios: (a) normal pot draft condition; (b) 50% reduced draft condition; (c) 50% reduced draft condition and one hood slid down.



(a)



(b)



(c)

Figure 6.5 Static pressure profile at a cross-section 0.85 m away from the central-plan of the pot in the *sliced pot model* under different scenarios: (a) normal pot draft condition; (b) 50% reduced draft condition; (c) 50% reduced draft condition with the modification of coving of the lower half of hood gaps.

6.5.2 Effect of the gap space between hoods

Although the normal gap space between hoods is typically around 2 cm, it can vary significantly in practice, as mentioned previously. In this sub-section, the gap space is changed to simulate different hooding conditions. The reference case is when all gaps between hoods have a width of 2 cm. Then, 4 cm gap is assigned to one of the four gaps in the 1/10 *sliced pot model* to represent a very common scenario where some of the hoods are not well placed due to their deformation in time or incautious placement. In the next scenario, all gaps between hoods are 4 cm wide which corresponds to a very bad placement of hoods. Finally, one hood mismatched with the pot superstructure is simulated by creating a large gap space around the mismatched hood (Fig. 6.4c). In all hooding scenarios, the pot draft condition was varied from normal to 50% reduced levels.

The estimation of how much fugitive emissions are released out of a pot is not trivial. No universal model can be applied to establish HF evolution for any type of smelting pot. The locations where HF is emitted from pot bath and crust can also vary in time, and from pot to pot. As a result, it can be difficult to precisely simulate the HF transport in the pot. In this work, two assumptions are invoked to simplify the calculations. First, one assumes that the HF concentration in the leaking pot gas is the same as that measured at the inlet of the collecting duct, which is available in literature. For a modern pot with more than 300 kA, the HF concentration at the inlet of the collecting duct is around 300-400 ppm (Dando and Tang 2006; Osen et al. 2011; Sommerseth et al. 2011). Due to its high temperature, emitted HF is lighter than the air in the cavity under the hoods. It will thus be driven upward and will accumulate at the top of the pot cavity under the superstructure horizontal plate. Therefore, the HF concentration is expected to be relatively uniform at the top of the pot cavity and we choose 350 ppm for the HF concentration in that zone under normal pot ventilation.

Another assumption is that the HF concentration of the leakage linearly increases with the reduced pot draft condition. In other words, the HF concentration of the leakage is doubled to 700 ppm as the draft is reduced by 50%. It is also reasonable because the diluted air flow rate dominates the total gas volume in the pot.

Using the two above-mentioned assumptions and knowing the mass flow rate of the leaking gas through pot openings, one can calculate how much HF escapes from a

1/10 pot into the potroom. A pot will emit approximately ten times this amount. We also know how many pots a potroom contains and how many tons of aluminum a potroom produces per year. Therefore, we can obtain HF emissions with respect to aluminum production (i.e., kg HF/ton Al). The HF emissions calculated in this manner are the sole contribution of “background fugitive emissions” (i.e. HF emission “at rest”, without pot operation) and can be compared with the regulatory limits of fluoride emissions. As mentioned previously, one of the scenarios in this study considers a hood slid down from its original position. Considering that the current model represents only 1/10th of a pot, it is unlikely that such bad hood placement would occur in each 1/10th of a pot. When calculating the total emissions of a pot in this scenario, we assumed that only one hood had slid down in each pot based on a survey of such hoods in a potroom.

The HF emissions under different hood gaps are reported in Fig. 6.6. Both normal and 50% reduced pot drafts were considered for the simulations. The first pair of columns represents the HF emissions under ideal pot conditions, namely the reference case or “4 gaps of 2 cm”. The pot is leakage free in the normal pot draft condition. If the pot draft is reduced by half, the gas leakage represents an addition of HF emission of 0.85 kg HF/t Al. Ref. (Tjahyono et al. 2011) presents some of the regulatory limits of fluoride emissions around the world as of 2011. The best performance in terms of total fluoride emissions is 0.2 kg F/t Al. Iceland requires 0.35 kg F/t Al. In the rest of the world, the limit is in the range 0.6-1.5 kg F/t Al. By comparing these limits with 0.85 kg HF/t Al, it appears that the 50% reduced pot draft condition is likely to be unacceptable. In the “1 gap of 4 cm” scenario (i.e. one hood gap with 4 cm breadth), the pot tightness is maintained well under normal draft condition and the HF emission is zero. However, a significant HF leakage, 0.027 kg HF/t Al, is observed even in normal draft if all hood gaps have a breadth of 4 cm (the “4 gaps of 4 cm” scenario), which corresponds to a very bad placement of hoods. In the case with one hood slid down, the equivalent HF emission as calculated by the present method is 0.043 kg HF/t Al. Since the pot tightness is barely maintained under ideal pot conditions for the 50% reduced draft condition, the other scenarios exhibit even worse performances. Therefore, modifications to the pot structure have to be implemented before reducing the draft level, which will be presented in Section 6.6.

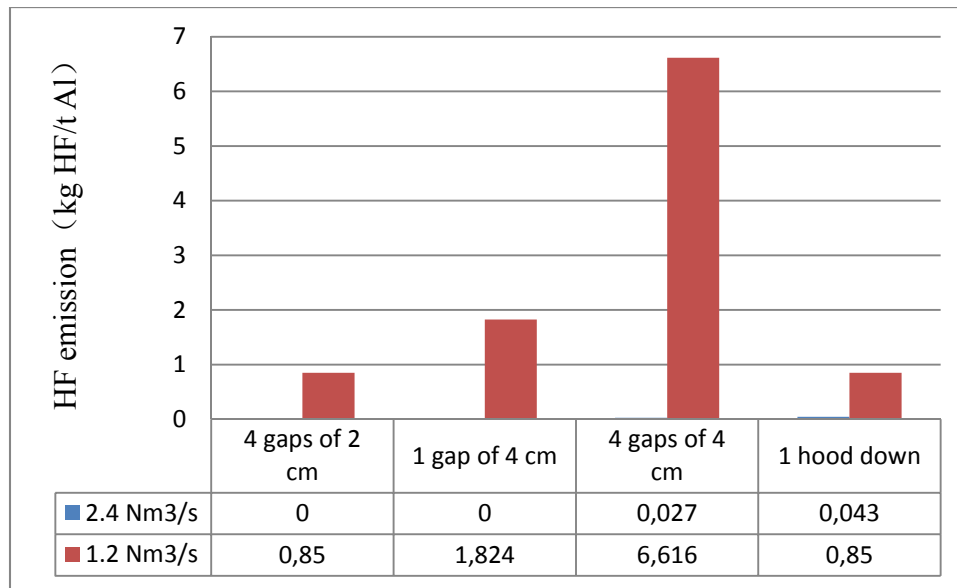


Figure 6.6 Estimated additional equivalent HF emissions in different scenarios of hood placement under both normal and 50% reduced draft conditions.

6.5.3 Effect of air flow pattern in potroom

The pressure imposed on the exterior of pot hoods and superstructure by the air flow in the potroom depends on the local flow pattern and structures. Available literature provides few experimental data or simulation results regarding this issue. In that zone, the static pressure is actually determined by numerous factors, such as the pot geometry, the buoyancy forces and wind-induced airflow in the potroom. One can input different velocity profiles on the surface A1 of the *potroom model* or the surface B1 of the *sliced pot model* to consider scenarios with different outdoor winds and different imposed heat fluxes on the surfaces of pot shell to simulate cases with different pot drafts (normal vs. 50% reduced pot drafts).

Figures 6.7a-b show the static pressure imposed on the hoods and superstructure under both normal and 50% reduced pot drafts. The outdoor wind is 10 km/h, blowing from the tapping end, which is a good representation of the potroom environment during daytime and with a medium wind outside. The pressure around the anode rods basically fluctuates around 0 Pa, depending on the airflow direction. The pressure at the windward surfaces is 0 to 1 Pa while it is 0 to -0.6 Pa at the side and leeward surfaces. The wind

induced pressure could be as low as -2 Pa in some areas with strong vortex due to the sharp-edge of the anode rod and the twist of two different air streams. The pressure distribution on the external pot shell has revealed that the pressure in the wake could be lower than that in the interior of the pot shell. If the pot vacuum is reduced due to the reduction of pot ventilation, pot gas will leak out from these areas.

6.5.4 Effect of the crust conditions (crust integrity and heat flux on it)

The open holes in the anode cover or crust can also affect pot tightness. They were represented in the present study by a gas inlet (0.5m×0.15m rectangle) on the anode cover, and a uniform velocity inlet is imposed to simulate the gases released from the bath (we assumed the same gas velocity as that of the gas released from feed holes). It is a very coarse approximation because we are only interested in the influence of the hot gas on the pot tightness.

The result shows little influence of such a hot gas on the leakage from the top openings. In fact, the released hot gas is deflected into the core area of the pot cavity by the makeup air inducing from potroom. The CFD result has shown that the hot gas from the open hole can barely rise up to the upper level when it just comes out from the hole.

In the second case, an increased heat flux is defined on the anode cover to represent the increase of top heat loss due to the reduction of the anode thickness, i.e. the consumption of the anode in bath. Based on an analytical model presented in our previous work (Zhao et al. 2013), the heat flux on the anode cover was increased from 2000 W/m² to 2500 W/m². Once again, increasing the amount of heat on anode cover did not significantly influence gas leakage in the simulation.

The results have shown that the crust conditions are not as important as the other factors. However, it should be noted that this conclusion is derived based on the influence of crust condition on the flow pattern. In fact, open holes can also emit more fluoride in the cavity under the hood. As a result, the increase in fluoride concentration can also increase the fugitive emissions into the potroom. Since the fluoride evolution is hard to predict and the simulation of fluoride transport in pot is not included in the present work, this issue is beyond the scope of this work.

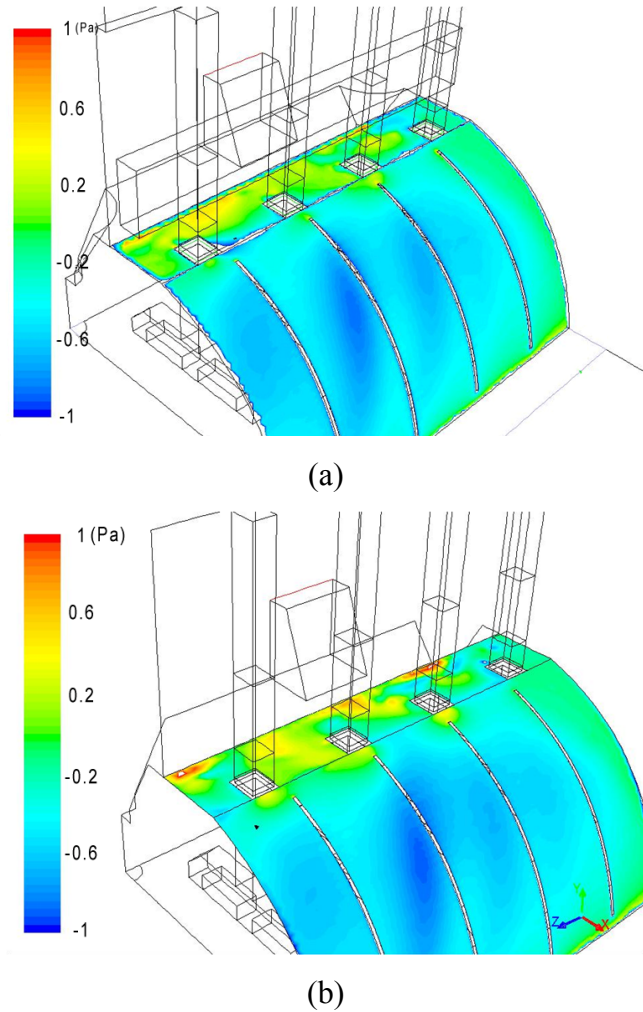


Figure 6.7 Static pressure on the pot shell due to the air flow in potroom, (a) normal draft condition; (b) 50% reduced draft condition.

6.6 Improvement of pot tightness

As mentioned previously, the objective of this chapter is to assess the pot tightness under reduced pot ventilation, and if required, to enhance it. The preceding section has illustrated that current pot structure cannot maintain satisfactory pot tightness under only half of the normal pot draft. Therefore, several modifications to the pot structures are proposed and their efficiency for retaining pot tightness and preventing gas leakages are estimated from simulations. Only scenarios with 50% reduced pot draft is simulated in this section.

6.6.1 Installation of fiber brushes

In the aluminum smelting pot that we studied, fiber brushes are usually installed to offer a partial sealing of the gap between the anode rod and the superstructure horizontal plate. A CFD simulation is performed to estimate its efficiency for a low pot draft condition.

Non-permeable walls were introduced to represent the barriers, and as a result, the gap around the anode rod is reduced to one quarter of its original value. The pot ventilation level simulated is $1.2 \text{ Nm}^3/\text{s}$, i.e. half of the normal draft. The result of the simulation showed that the pot tightness is retained under half of the normal pot draft with the usage of brushes. Although the brushes cannot completely cover the opening around anode rod, the uncovered area is actually at the windward side of the anode rod with respect to the external flowing air, which creates a positive pressure above the uncovered opening and acts as a barrier against gas leakage.

The performance of a pot with brushes is further verified in a case where there is one gap with a wider opening (4 cm width) between hoods due to the hood deformation or an inappropriate placement, or the “1 gap of 4 cm” case. Significant leakage is observed from both the gaps around rods and between hoods. The equivalent HF emission is 0.36 kg HF/t Al , which is comparable with legal emission limits. Considering that this would be an additional emission to the current emissions and that this scenario can represent real situations of hood placement, the installation of barriers at the gaps around anode rods does not seem to be sufficient to prevent leakage for a pot operating with a 50% reduced draft. The results tend to demonstrate that brushes can only retain pot tightness when the pot is operated under ideal conditions. A detailed survey of the pressure in the area just beneath the superstructure horizontal plate shows that the installed brushes slightly increase the vacuum in the top area of the internal pot, but do not produce a significantly lower pressure compared with that at the exterior of pot shell.

6.6.2 Covering of the lower half of the gaps between hoods

Since gas leakage from pot openings is mostly due to the loss of vacuum in the pot cavity, one potential design modification is to cover a significant portion of the current opening, i.e. the lower half of the gaps between hoods. This modification aims at

increasing the pot tightness by reducing the opening area, and moving upward the neutral pressure plane. The pressure profile in both the pot cavity and potroom can be depicted approximately in Fig. 6.2. The internal pressure is dictated not only by the buoyancy forces but also by the mechanical ventilation induced by the pot ventilation system. It is seen that the largest pressure difference happens in the lower position of the pot cavity. The pressure difference is decreased as the height rises up, which in turn results in the same pattern for the induced airflow. In other words, the lower the position, the higher the air suction rate. When the pot draft is reduced, the majority of air inflow passes through the lower portion of the gaps between hoods. We considered a scenario where barriers (e.g., “lips” along the hood edge) are installed to cover the lower half part of the gaps in order to increase the pot tightness. In the CFD model, we assumed that the covering was perfect and the vertical extension of the gaps between hoods is shortened to only half of the original ones, as shown in Fig. 6.8.

The influence of this modification on pot vacuum is studied by the model developed in this chapter. Gas leakage vanished even in $1.2 \text{ Nm}^3/\text{s}$ pot draft. The internal pressure profile with and without modifications is compared for a specific cross-section surface in Fig. 6.5b-c. In the area just beneath the superstructure horizontal plate, the negative pressure is reduced to $\sim -2\text{Pa}$ (Fig. 6.5c) while it is only $\sim -0.5\text{Pa}$ (Fig. 6.5b) in the case without modifications. The results have illustrated that covering the lower part of the gap between hoods could sufficiently enhance the pot vacuum in reduced pot draft conditions.

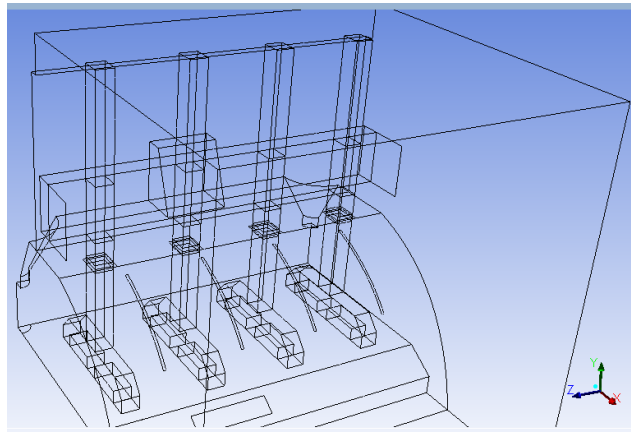


Figure 6.8 schematic representation illustrating the sealing of the lower half of hood gaps.

The modification was also verified in scenarios with different gap spaces. Figure 9 shows the equivalent HF emission of the pot with gaps covered by half in different scenarios. Again, the HF emission of the non-modified pot under 50% reduced pot draft is 0.85 kg HF/ton Al. The results indicate that this modification can enhance pot tightness sufficiently to prevent leakage in the “4 gaps of 2 cm” case (ideal condition) and the “1 gap of 4 cm” case, which are the two most common situations. The leakage is well controlled even when 2 or all hood gaps are 4 cm wide (the “2 gaps of 4 cm” and “4 gaps of 4 cm” scenarios). The equivalent HF emission is only around 0.02 kg HF/t Al, which is minor compared with the regulatory emission limits mentioned above. The only exception is found when one hood is slid down from the superstructure and a significant opening is created at the hood top. The equivalent HF emission is comparable to the regulatory limits and thus, hoods slid down should be replaced as much as possible in real operations.

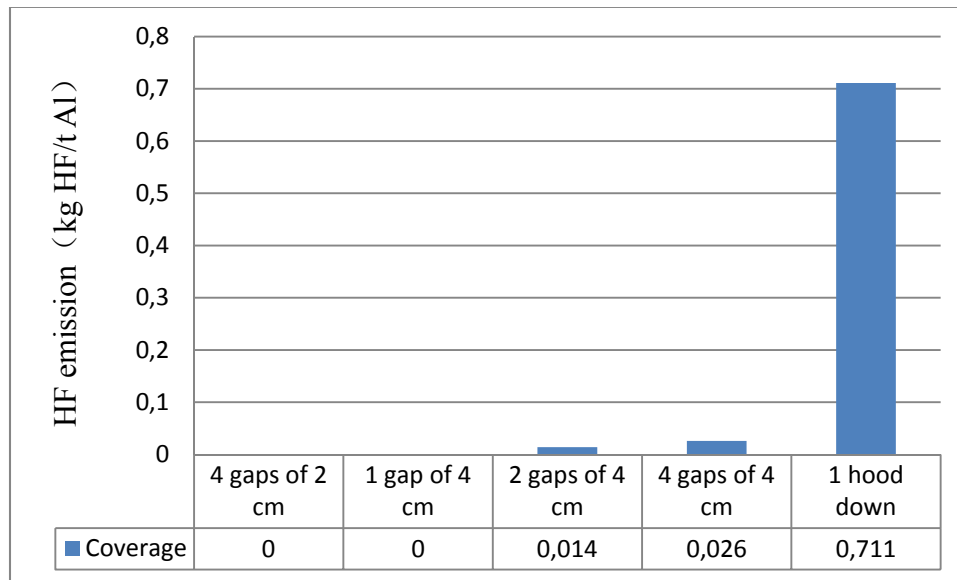


Figure 6.9 Additional equivalent HF emissions from the pot when reducing the draft by half and sealing the lower half of the gaps between hoods, under different hood placement scenarios.

6.7 Conclusions

In the present paper, a CFD model is developed and validated to study pot tightness under different scenarios. Two domains with different simulation lengthscales are created to simulate the heat transfer and air flow in both interior and exterior of pots. In the perspective of waste heat recovery and energy savings, a particular attention is devoted to the possible reduction of pot draft conditions.

The CFD results reveal that current pot structure can maintain good tightness in normal draft condition, but fails in 50% reduced draft. Since the leakage of pot gas in a reduced draft condition would add up to the currently existing fluoride emissions, it would be required to enhance pot tightness in order to reduce the pot ventilation rate. Two pot designs are tested under 50% reduced draft. The installation of barriers at the gaps around anode rods gives a good tightness within ideal pot conditions. Nevertheless, based on our model, it fails if only one hood gap space extends to 4 cm. Covering half of the hood gaps has shown a desirable tightness even when all gaps are 4 cm wide.

The simulation results have illustrated that the pot gas can be constrained in the pot with only 50% of normal ventilation rate with a proper sealing of the pot. In addition, the influence of the air flow in the potroom on the pressure on the pot shell is demonstrated and can extract pot gas out if the pot vacuum is too small. Heat flux and open holes on anode cover had little influence on the leakage of pot gas in our simulations.

CHAPTER 7 CONCLUSIONS AND FUTURE WORK

This thesis aims at solving two key questions: how to efficiently collect the waste heat from aluminum smelting cells and how to technically realize the recovery. Based on the distribution of waste heat dissipation in cells, the pot exhaust gas carries away 35%-40% of heat content while the rest is released from the pot shell, i.e., hoods and superstructure, sidewall and bottom. It is therefore required to determine a most effective way to retrieve the heat from pots. Besides, different pot parameters need to be optimized in order to maximize the thermal quality of the waste heat. Once it was determined to reduce the draft of pot exhaust gas, a detailed study was done on how to achieve a pot draft reduction without other adverse effects. In the present work, three expected problems associated with the draft reduction were investigated using CFD simulations. The main results are summarized in the following sections. The simulated results have illustrated a successful realization of the pot draft reduction. Future works may include an experimental validation in real smelters and an economical application of the recovered waste heat.

7.1 Mechanism of heat transfer in the upper part of an aluminum smelting cell

Although a few papers suggested to collect waste heat through pot sidewalls, it is still not recommended because of the subtle thermal balance between the electrolytic bath and the heat loss from sidewalls. Therefore, in this thesis, attention was paid to the upper part of an aluminum smelting cell.

A simple mathematical model based on a thermal circuit representation was first developed to study how heat is dissipated in the cell upper part. This model considered all mechanisms of heat transfer (i.e., conduction, convection and radiation) occurring in the cell and can be solved quickly. It only requires the bath temperature and ambient temperature as boundary conditions and can determine the internal temperatures and heat transfer rates in each component. We developed an original formulation to be applied in fin-like elements with internal Joule heating, such as anode rod, yoke and stubs.

Within this model, a sensitivity analysis of the parameters of interest was done. The purpose is to maximize the temperature of the pot exhaust gas while taking into account the thermal management in the cell. Among different parameters, the mass flow rate of the pot exhaust gas has the larger influence on its temperature and heat content. A

50% reduction of the normal draft level can increase the gas temperature by 50-60°C, which is a significant augmentation in terms of thermal quality. The gas temperature is also strongly correlated to the convection on the top surface of anode cover and on the surface of yoke and stubs. In order to achieve a proper heat management under reduced pot ventilation, these areas may play a role of modulation. Strengthening the thermal insulation of hoods redirected more heat in the pot gas, and an optimal insulating level was obtained. Ambient temperature and anode height are also important factors when designing any modification in the pot.

A CFD model was then developed to obtain more details than with the simple model. Besides, the CFD model provided more accurate correlations between the convective heat transfer coefficient and pot draft condition, which were applied in the thermal circuit model. The non-uniformity of heat transfer in surfaces was visualized and the relative importance of natural vs. forced convections was revealed under different pot ventilation. The results show that the forced convection is dominating heat transfer under normal pot draft while both mechanisms are equally important under reduced drafts.

This model can be easily adapted to any type of industrial pots and used to calculate the heat condition in pot. It is also a quick tool to estimate any possible changes in pot and operating parameters. The calculated results can give the engineers some coarse results in order to reduce the experimental scales.

7.2 The reduction of pot draft condition

Based on the above mentioned study, it has become apparent that the reduction of pot draft is the most promising strategy for waste heat recovery from smelting cells. In fact, the reduction of pot draft condition can bring out some other benefits, such as a tremendous saving of electricity for fan operation, downsizing the collecting ducts and less fluoride evolution. In the present studies, our objective was set to achieve a reduction by half of the normal pot draft condition. For the smelters in ADQ, that means to reduce the single pot draft from 2.4 Nm³/s to 1.2 Nm³/s. Further reduction is possible but the corresponding modifications would become more stringent.

We have expected three main issues that might result from the implementation of pot draft reduction. The first influence is the satisfaction in the top heat loss, which may

cause heat imbalance in the bath. Enhancement in heat transfer is required in the upper part of smelting cells. Then, the reduction of pot draft redirects a portion of the dissipated heat into the potroom. It is important to estimate the influence of the additional heat on the heat stress in potroom. The final mission is to guarantee the hooding efficiency of pot superstructure under reduced pot draft, because of the control of fugitive emissions.

7.2.1 Heat management in reduced pot draft

The first problem in relation with the pot draft reduction is the heat loss from the upper part of a smelting cell. The total top heat loss is reduced by ~10% as the pot draft goes down to half of its normal value. According to the engineers' experiences, it would be a significant change in the total heat balance of the pot and modification is required to enhance the top heat loss.

A CFD model was developed to investigate how to remove the same amount of heat from the bath under the 50% reduced pot draft scenario. Different modifications were simulated, including addition of fins on anode assembly, geometrical modification of hood gaps and geomorphological modification of anode cover. The results have shown that the scenario of exposing more stubs to the air in the hooded space can perfectly compensate the missing capacity in the top heat loss. The installation of fins on anode assembly gave little contribution to the top heat loss. Although more heat can be convectively removed from the increased area of anode assembly, the fins also created interferences with radiative heat transfer. The net effect was marginal. A scenario with moderate effect lied in horizontally oriented hood gaps. However, the enhancement in top heat loss was not enough to recover the missing part.

7.2.2 Heat stress of potroom in reduced pot draft

In the second part, the heat stress in potroom was estimated under a 50% reduced pot draft. To address this issue, air ventilation and heat transfer were simulated in a potroom. In order to limit the number of control volumes, the fluid boundary conditions were directly defined on the building's openings. Both buoyancy and wind driven forces were considered in the simulations. Higher heat flux was imposed on the pot shell to represent a new heat loss distribution in 50% reduced pot draft. An international standard, which is

usually applied in extremely hot environment, was employed to estimate the heat stress in potroom. A specific parameter, During Limitation Exposure, was obtained from the standard to measure heat stress on working operators. The results have revealed an intensive heat stress existing in the potroom in summer season while the heat stress, compared with that in normal pot draft, was only slightly increased in the 50% reduced pot draft condition. This model also provided our industrial partner with a tool to study other modifications related to potroom design.

7.2.3 Pot tightness and emission control in reduced pot draft

The final work was focused on the pot tightness under reduced pot draft. Two CFD models with different simulation scales were created to simulate the flow in both the interior and exterior of a pot. It was found that current pot structure can maintain good tightness in normal draft condition while it is likely to fail in 50% reduced draft. The constant leakage of pot gas will contribute to an additional fluoride emission even more than the current baseline. Two modifications in the pot structure were proposed and verified. If the pot was maintained in ideal conditions, the installation of barriers at the gaps around anode rods provided a good tightness. Nevertheless, leakage occurred if only one hood gap space is as large as 0.04m which frequently occurs in reality. Covering the lower half of the hood gap has shown a desirable tightness even when all gaps were 4 cm wide. The results have illustrated that the pot gas can be constrained in the pot with only 50% of normal ventilation rate if proper sealing was realised on pots.

7.2.4 Other “side” contributions of this thesis

It is important to mention that although this work was initially motivated by the desire to facilitate waste heat recovery from pots, several other practical benefits have resulted from our work, such as:

- The air ventilation in potroom can be simulated by using the CFD model representing a slice of potroom. Optimization of the ventilation was performed based on the interests from industrial partners. For example, potroom ventilation was simulated in different scenarios where the interior openings on wall and floor

were modified. The potroom structure was optimized to achieve a better sidewall cooling, which is of critical importance for the “load creeping” in smelting cells.

- New pressure coefficients on the exterior wall of potroom were established for the specific potroom geometry, as the coefficients calculated from some conventional correlations were not suitable for such buildings.
- CFD simulations of fugitive emissions from smelting pot provided with deep insight in the pot tightness, which in turn helped to improve the emission control in current cells.
- A procedure of CFD simulation of the air ventilation in a tall building with strong heat source, such as the potroom, was presented for the CFD simulation in other types of buildings with the similar conditions. Different modeling settings, such as the definition of air density, the choice of reference density and the influence of environment, were studied and verified in the simulations.

7.3 Future work

This thesis has demonstrated the possibility of a 50% reduction of the normal pot draft in an aluminum smelting cell based on numerical simulations. Several technical problems associated with the draft reduction have been addressed. Possible future work can be summarized as follows:

- Although the simulated results are verified and validated with experimental measurements in real pots, large-scale experiments in real smelters are required to directly validate the simulated results. All validated scenarios are limited in a normal pot draft condition. Therefore, the reduced pot draft should be applied to real pots with the proper modifications for testing pot functionality.
- All works involved in this thesis are focused on the pot upper part while it is also crucial to design facilities for extracting heat from the exhaust gas. A heat exchanger should be designed and well integrated into the duct system. Moreover, the application of waste heat should be studied case-by-case, depending on the local situation and potential users. For instance, it can provide a heat source for neighboring residences or greenhouses. If the local electricity price is high, an

Organic Rankine Cycle may be considered to produce electricity. Direct use in the pot, such as for alumina preheating, could also be considered.

- Our thermal circuit model can be further extended to the sidewalls and bottom. It could be used as a quick tool for controlling the heat balance in the pot. Thermal capacitances may be included to take into account transient dynamics.
- The transport of hydrogen fluoride in the pot hooded space should be added in the CFD simulation. To have the information of HF concentration may help us to design new pot structures for a better control of fugitive emissions. The challenge of this work is to find a proper way to define the HF evolution in the pot.

REFERENCES

- Abbas, H., 2010. Mechanism of Top Heat Loss from Aluminium Smelting Cells. Ph.D. Thesis, Chemical and Material Engineering, University of Auckland.
- Abbas, H., Taylor M.P., Farid, M. and Chen, J.J., 2009. The Impact of Cell Ventilation on the Top Heat Losses and Fugitive Emissions in an Aluminium Smelting Cell. *TMS-Light Metals*, p. 551-561.
- Alie, C., Backham, L., Croiset, E. and Douglas, P.L., 2005. Simulation of CO₂ Capture Using MEA Scrubbing: A Flowsheet Decomposition Method. *Energy Conversion and Management* 46 (3), p. 475-487.
- Aljabri, N., Venkatasubramaniam, K.G., AlFarsi, Y.A.M. and Dubai, J.A., 2003. HF Emission from Dubal's Electrolysis Cell. *TMS-Light Metals*, p. 487-494.
- ASHRAE. 2009. *ASHRAE Handbook-Fundamentals*. Atlanta, GA, 24.3-24.5.
- Bergman, T.L., Lavine, A.S., Incropera, F.P. and Dewitt, D.P., 2011. *Introduction to Heat Transfer*. John Wiley & Sons, Incorporated.
- Berkoe, J., Diwakar, P., Martin, L., Baxter, B., Read, C.M., Grover, P. and Ziegler, D., 2005. CFD Modeling of the Fjardaal Smelter Potroom Ventilation. *TMS-Light Metals*, p. 373-378.
- Biedler, P., 2003. Modeling of an Aluminum Reduction Cell for the Development of a State Estimator. West Virginia University.
- Bruggeman, J.N., and Danka, D.J., 1990. Two-Dimensional Thermal Modeling of the Hall-Heroult Cell. *TMS-Light Metals*, p. 203-209.
- Chataigner, Y., Gosselin, L. and Doré, G., 2009. Optimization of Embedded Inclined Open-Ended Channel in Natural Convection Used as Heat Drain. *International Journal of Thermal Sciences* 48 (6), p. 1151-1160.
- Chen, Q., 1995. Comparison of Different k- ϵ Models for Indoor Air Flow Computations. *Numerical Heat Transfer, Part B: Fundamental* 28 (3), p. 353-369.
- Chow, W.K., 1995. Ventilation Design: Use of Computational Fluid Dynamics as a Study Tool. *Building Services Engineering Research and Technology* 16 (2), p. 63-76.
- Cook, M.J., Ji, Y. and Hunt, G.R., 2003. CFD Modelling of Natural Ventilation: Combined Wind and Buoyancy Forces. *International Journal of Ventilation* 1 (3), p. 169-179.
- Cook, M.J. and Lomas, K.J., 1998. Buoyancy-Driven Displacement Ventilation Flows: Evaluation of Two Eddy Viscosity Turbulence Models for Prediction. *Building Services Engineering Research and Technology* 19 (1), p. 15-21.
- Dando, N.R. and Tang, R., 2006. Impact of Tending Practices on Fluoride Evolution and Emission from Aluminum Smelting Pots. *TMS-Light Metals*, p. 203-206.
- Dando, N.R. and Tang, R., 2005. Fluoride Evolution/Emission from Aluminum Smelting Pots-Impact of Ore Feeding and Cover Practices. *TMS-Light Metals*, p. 363-366.

- David, J., and Herzog, H., 2000. The Cost of Carbon Capture. In *Fifth International Conference on Greenhouse Gas Control Technologies, Cairns, Australia*, p. 13-16.
- Dernedde, E., 1990. Gas Collection Efficiency on Prebake Reduction Cells. *The American Industrial Hygiene Association Journal* 51 (1), p. 44–49.
- Dernedde, E., 2004. Ventilation Rates of Smelter Buildings in Northern Climates. *TMS-Light Metals*, p. 347–350.
- Doheim, M.A., El-Kersh, A.M. and Ali, M.M., 2007. Computational Modeling of Flow in Aluminum Reduction Cells due to Gas Bubbles and Electromagnetic Forces. *Metallurgical and Materials Transactions B* 38 (1), p. 113–119.
- Dupuis, M., 1998. Computation of Aluminum Reduction Cell Energy Balance Using ANSYS® Finite Element Models. *TMS-Light Metals*, p. 409–418.
- Dupuis, M., 2001. 3D Modeling of the Ventilation Pattern in an Aluminium Smelter Potroom Building Using CFX-4. In *Proceedings of the CFDSC Conference*, p. 161–166.
- Dupuis, M., 2010. Development and Application of an ANSYS (r) Based Thermo-Electro- Mechanical Anode Stub Hole Design Tool. *TMS-Light Metals*.
- Dupuis, M., Bojarevics, V. and Freilbergs, J., 2004. Demonstration Thermo-Electric and MHD Mathematical Models of a 500 kA Aluminum Electrolysis Cell: Part 2. *TMS-Light Metals*, p. 453–460.
- Dussault, J., Gosselin, L. and Galstian, T., 2012. Integration of Smart Windows into Building Design for Reduction of Yearly Overall Energy Consumption and Peak Loads. *Solar Energy* 86 (11), p. 3405–3416.
- Eggen, T., Rolseth, S., Rye, K.A. and Thonstad, J., 1992. Alumina Crusting in Cryolite Melts, Part I: Penetration of Molten Electrolyte into Alumina. *TMS-Light Metals*.
- Eick, I., and Vogelsang, D., 1999. Dimensioning of Cooling Fins for High-Amperage Reduction Cells. *TMS-Light Metals*, p. 527–533.
- Fanisalek, H., Bashiri, M. and Kamali, R., 2011. Waste Heat Recovery Trial from Aluminum Reduction Cell Exhaust Gases. *Energy Technology 2011: Carbon Dioxide and Other Greenhouse Gas Reduction Metallurgy and Waste Heat Recovery*, p. 65.
- Fleer, M., Lorentsen, O.A., Harvey, W., Palsson, H., and Saevarsdottir, G., 2010. Heat Recovery from the Exhaust Gas of Aluminum Reduction Cells. Minerals, Metals and Materials Society/AIME, 420 Commonwealth Dr., P. O. Box 430 Warrendale PA 15086 USA.
- Fluent Ansys, 2012. *Ansys Fluent 14.5 Users Guide*. Fluent Inc., Lebanon, NH.
- Fortin, H., Kandev, N. and Fafard, M., 2012. FEM Analysis of Voltage Drop in the Anode Connector Induced by Steel Stub Diameter Reduction. *Finite Elements in Analysis and Design* 52, p. 71–82.

- Fraser, K.J., Taylor, M.P. and Jenkin, A.M., 1990. Electrolyte Heat and Mass Transport Processes in Hall Heroult Electrolysis Cells. *TMS-Light Metals*, p. 221–226.
- Gadd, M.D., Ph.D. Thesis. 2003. Aluminium Smelter Cell Energy Flow Monitoring. Chemical and Materials Engineering, University of Auckland.
- Gadd, M.D., Welch, B.J. and Ackland, A.D., 2000. The Effect of Process Operations on Smelter Cell Top Heat Losses. *TMS-Light Metals*.
- Green, D.W., and others. 2008. *Perry's Chemical Engineers' Handbook*. Vol. 796. McGraw-hill New York.
- Grjotheim, K., and Kvande, H., 1986. *Understanding the Hall–Heroult Process for Production of Aluminium*. Aluminum-Verlag, P. O. Box 1207, D-4000 Dusseldorf 1, FRG, 1986.
- Gusberti, V., Severo, D.S., Welch, B.J. and Skyllas-Kazacos, M., 2012. Modeling the Mass and Energy Balance of Different Aluminium Smelting Cell Technologies. *TMS-Light Metals*, p. 929–934.
- Hatem, G., Llavona, M., Log, T., Sancho, J.P. and OSTVOLD, T., 1988. Thermal-Conductivity of Some Alumina Powders and Synthetic Hall-Heroult Crusts. *JOURNAL OF METALS*, 40, p. 127.
- Haugland, E., Borset, H., Gikling, H. and Hoie, H., 2003. Effects of Ambient Temperature and Ventilation on Shell Temperature, Heat Balance and Side Ledge of an Alumina Reduction Cell. *TMS-Light Metals*, p. 269–276.
- Haupin, W.E., 1971. Calculating Thickness of Containing Walls Frozen from Melt. *J METALS* 23 (7), p. 41–44.
- Hofmann, H.M., Kaiser, R., Kind, M. and Martin, H., 2007. Calculations of Steady and Pulsating Impinging Jets—an Assessment of 13 Widely Used Turbulence Models. *Numerical Heat Transfer, Part B: Fundamentals* 51 (6), p. 565–583.
- Hussain, S., and Oosthuizen, P.H., 2012a. Numerical Investigations of Buoyancy-Driven Natural Ventilation in a Simple Atrium Building and Its Effect on the Thermal Comfort Conditions. *Applied Thermal Engineering* 40, p. 358–372.
- Hussain, S. and Oosthuizen, P.H., 2012b. Validation of Numerical Modeling of Conditions in an Atrium Space with a Hybrid Ventilation System. *Building and Environment* 52, p. 152–161.
- Isman, M.K., Pulat, E., Etemoglu, A.B. and Can, M., 2008. Numerical Investigation of Turbulent Impinging Jet Cooling of a Constant Heat Flux Surface. *Numerical Heat Transfer, Part A: Applications* 53 (10), p. 1109–1132.
- Jacobs, H.R., 1987. *Convection Heat Transfer: A. Bejan*. Elsevier.
- Jessen, S.W., Master Thesis. 2008. Mathematical Modeling of a Hall Hérault Aluminum Reduction Cell. Technical University of Denmark.
- Ji, Y., and Cook, M.J., 2007. Numerical Studies of Displacement Natural Ventilation in Multi-Storey Buildings Connected to an Atrium. *Building Services Engineering Research and Technology* 28 (3), p. 207–222.

- Ji, Y., Cook, M.J. and Hanby, V., 2007. CFD Modelling of Natural Displacement Ventilation in an Enclosure Connected to an Atrium. *Building and Environment* 42 (3), p. 1158–1172.
- Karlsen, M., Kielland, V., Kvande, H. and Vestre, S.B., 1998. Factors Influencing Cell Hooding and Gas Collection Efficiencies. *TMS-Light Metals*, p. 910–917.
- Kiss, L., and Dassylva-Raymond, V., 2008. Freeze Thickness in the Aluminum Electrolysis Cells. *TMS-Light Metals*, p. 431.
- Kolondzovski, Z., Belahcen, A. and Arkkio, A., 2009. Multiphysics Thermal Design of a High-Speed Permanent-Magnet Machine. *Applied Thermal Engineering* 29 (13), p. 2693–2700.
- Li, Z.R., Ai, Z.T., Wang, W.J., Xu, Z.R., Gao, X.Z. and Wang, H.S., 2013. Evaluation of Airflow Pattern in Wind-Driven Naturally Ventilated Atrium Buildings: Measurement and Simulation. *Building Services Engineering Research and Technology*.
- Llavona, M., 1988. Some New Considerations on the Measurement of Humidity, M. O. I. and L. O. I. *TMS-Light Metals*, p. 103–108.
- Logan, P.W., and Bernard, T.E., 1999. Heat Stress and Strain in an Aluminum Smelter. *American Industrial Hygiene Association Journal* 60 (5), 659–665.
- Lorentsen, O.A., Dyrøy, A., and Karlsen, M., 2009. Handling Co₂EQ from an Aluminum Electrolysis Cell. *TMS-Light Metals*, p. 263.
- Luo, Z., Cho, H., Luo, X. and Cho, K., 2008. System Thermal Analysis for Mobile Phone. *Applied Thermal Engineering* 28 (14), p. 1889–1895.
- Maarschalkerwaard, A., 2010. The Use of CFD Simulations to Optimise Ventilation of Potrooms. Minerals, Metals and Materials Society/AIME, 420 Commonwealth Dr., P. O. Box 430 Warrendale PA 15086 USA.
- Marois, M.A., Bertrand, C., Désilets, M., Coulombe M.M., and Lacroix, M., 2009. Comparison of Two Different Numerical Methods for Predicting the Formation of the Side Ledge in an Aluminium Electrolysis Cell. *TMS-Light Metals*, p. 563–568.
- McQuiston, F.C., Parker, J.D. and Spitler, J.D., 2010. *Heating, Ventilating, and Air Conditioning: Analysis and Design*. Vol. 6. Wiley.
- Meghlaoui, A., Farsi, Y.A.A. and Aljabri, N.H., 2002. Analytical and Experimental Study of Fluoride Evolution. *TMS-Light Metals*, p. 283–288.
- Menet, N., Girault, G., Monnet, N., Turpin, C., and Soulhac, L., 2013. Latest Developments in Potroom Building Ventilation CFD Modelling. *TMS-Light Metals*, p. 811–816.
- Menter, F.R., 1994. Two-Equation Eddy-Viscosity Turbulence Models for Engineering Applications. *AIAA Journal* 32 (8), p. 1598–1605.
- Mills, A.F., 1999. *Heat Transfer*. 2nd edition. New Jersey: Prentice Hall.
- Modest, M.F., 2013. *Radiative Heat Transfer*. Academic Press.

- Nagem, N.F., Batista, E., Silva, A.F., Gomes, V., Ferreira, H., Mendes, R.R.S. and Souza, L.J.P., 2006. Correlation of Fluoride Evolution with on Line off Gas Duct Temperature. *TMS-Light Metals*, p. 207.
- Nagem, N.F., Batista, E., Silva, A.F., Gomes, V., Venâncio, L.C.A. and Souza, L.J.P., 2005. Understanding Fugitive Fluoride Emissions at the Alumar. *TMS-Light Metals*, p. 289–292.
- Namboothiri, S., Lavoie, P., Cotton, D. and Taylor, M., 2009. Controlled Cooling of Aluminium Smelting Cell Sidewalls Using Heat Exchangers Supplied with Air. *TMS-Light Metals*, p. 317–322.
- Nowicki, C., and Gosselin L., 2012. An Overview of Opportunities for Waste Heat Recovery and Thermal Integration in the Primary Aluminum Industry. *JOM* 64 (8), p. 990–996.
- Nowicki, C., Gosselin, L. and Duchesne, C., 2012. Waste Heat Integration Potential Assessment through Exergy Analysis in an Aluminium Production Facility. *TMS-Energy Technology 2012: Carbon Dioxide Management and Other Technologies*, p. 165–172.
- Osen, K.S., Aarhaug, T.A., Solheim, A., Skybakmoen, E. and Sommerseth, C., 2011. HF Measurements inside an Aluminium Electrolysis Cell. *TMS-Light Metals*.
- Palyvos, J.A., 2008. A Survey of Wind Convection Coefficient Correlations for Building Envelope Energy Systems' Modeling. *Applied Thermal Engineering* 28 (8), p. 801–808.
- Parsons, K.C., 1999. International Standards for the Assessment of the Risk of Thermal Strain on Clothed Workers in Hot Environments. *Annals of Occupational Hygiene* 43 (5), p. 297–308.
- Patterson, E.C., Ph.D. Thesis. 2002. Fluoride Emissions from Aluminium Electrolysis Cells. ResearchSpace@Auckland.
- Perry, R.H., Green, D.W. and Maloney, J.O., 1984. *Perry's Chemical Engineering Handbook*. Don Green, New York.
- Ramponi, R., and Blocken, B., 2012. CFD Simulation of Cross-Ventilation for a Generic Isolated Building: Impact of Computational Parameters. *Building and Environment* 53, p. 34–48.
- Rye, K.A.A., Thonstad, J. and Liu X., 1995. Heat Transfer, Thermal Conductivity, and Emissivity of Hall-Heroult Top Crust. *TMS-Light Metals*, p. 630–638.
- Saathof, P.J., Stathopoulos, T. and Dobrescu, M., 1995. Effects of Model Scale in Estimating Pollutant Dispersion near Buildings. *Journal of Wind Engineering and Industrial Aerodynamics* 54, p. 549–559.
- Severo, D.S., and Gusberti, V., 2009. A Modelling Approach to Estimate Bath and Metal Heat Transfer Coefficients. *TMS-Light Metals*, p. 309–314.

- Severo, D.S., Schneider, A.F., Pinto, Elton C.V., Gusberti, V. and Potocnik, V., 2005. Modeling Magnetohydrodynamics of Aluminum Electrolysis Cells with ANSYS and CFX. *TMS-Light Metals*, p. 475-480.
- Sharif, M.A.R., and Mothe, K.K., 2009. Evaluation of Turbulence Models in the Prediction of Heat Transfer due to Slot Jet Impingement on Plane and Concave Surfaces. *Numerical Heat Transfer, Part B: Fundamentals* 55 (4), p. 273-294.
- Shcherbinin, S.A., Rozin, A.V. and Lukashchuk, S.Y., 2003. The 3D Modeling of MHD-Stability of Aluminum Reduction Cells. *TMS-Light Metals*, p. 373-378.
- Shen, X.C., Ph.D. Thesis. 2006. Top Cover and Energy Balance in Hall-Heroult Cells. ResearchSpace@ Auckland.
- Shen, X.C., Hyland, M. and Welch, B., 2008. Top Heat Loss in Hall-Heroult Cells. *TMS-Light Metals*, p. 501.
- Slaughaupt, M.L., Bruggeman, J.N., Tarcy, G.P. and Dando, N.R., 2003. Effect of Open Holes in the Crust on Gaseous Fluoride Evolution from Pots. *TMS-Light Metals*, p. 199-204.
- Smith, P.L., and Winkle, M.V., 1958. Discharge Coefficients through Perforated Plates at Reynolds Numbers of 400 to 3,000. *AIChE Journal* 4 (3), p. 266-268.
- Solheim, A., 2011. Some Aspects of Heat Transfer between Bath and Sideledge in Aluminium Reduction Cells. *TMS-Light Metals*, p. 381-386.
- Sommerseth, C., Osen, K.S., Aarhaug, T.A., Skybakmoen, E., Solheim, A., Rosenkilde, C. and Ratvik, A.P., 2011. Correlation between Moisture and HF Formation in the Aluminium Process. *TMS-Light Metals*, p. 339-344.
- Sørhuus, A., and Wedde, G., 2009. Pot Gas Heat Recovery and Emission Control. *TMS-Light Metals*, p. 987-992.
- Sorhuus, A., Wedde, G., Rye, K. and Nyland, G., 2010. Increased Energy Efficiency and Reduced HF Emissions with New Heat Exchanger. Minerals, Metals and Materials Society/AIME, 420 Commonwealth Dr., P. O. Box 430 Warrendale PA 15086 USA.
- Stamou, A.I., Katsiris, I. and Schaelin, A., 2008. Evaluation of Thermal Comfort in Galatsi Arena of the Olympics 'Athens 2004' Using a CFD Model. *Applied Thermal Engineering* 28 (10), p. 1206-1215.
- Tarcy, G.P., 2003. The Affect of Pot Operation and Work Practices on Gaseous and Particulate Fluoride Evolution. *TMS-Light Metals*, p. 193-198.
- Taylor, M.P., 2007. Anode Cover Material-science, Practice and Future Needs. In *Proceedings of 9th Australasian Aluminium Smelting Technology Conference*, p. 4-9.
- Taylor, M.P., Johnson, G.L., Andrews, E.W. and Welch, B.J., 2004. The Impact of Anode Cover Control and Anode Assembly Design on Reduction Cell Performance. *TMS-Light Metals*, p. 199-206.

- Taylor, M.P., 1984. The Influence of Process Dynamics on the Heat Balance and Cell Operation in the Electrowinning of Aluminium. ResearchSpace@ Auckland.
- Taylor, M.P., Zhang, W.D., Wills, V. and Schmid, S., 1996. A Dynamic Model for the Energy Balance of an Electrolysis Cell. *Chemical Engineering Research and Design* 74 (8), p. 913–933.
- Tessier, J., Duchesne, C., Gauthier, C. and Dufour, G., 2008. Image Analysis for Estimation of Anode Cover Material Composition. *TMS-Light Metals*, p. 293.
- Tjahyono, N., Gao, Y., Wong, D., Zhang, W. and Taylor, M.P., 2011. Fluoride Emissions Management Guide (FEMG) for Aluminium Smelters. *TMS-Light Metals*. John Wiley & Sons, Inc. Hoboken, NJ.
- Tomasino, T., Martin, C., Waz, E. and Renaudier S., 2004. Numerical Modeling of Heat Transfer around an Aluminum Reduction Pot Shell.” *TMS-Light Metals*, p. 433–438.
- True, J.P.J., Ph.D. Thesis. 2003. Openings in Wind Driven Natural Ventilation. Aalborg University, Faculties of Engineering, Science and Medicine, Institut for Bygningsteknik, Department of Building Technology and Structural Engineering.
- Vershenya, A., Shah, U., Broek, S., Plikas, T., Woloshyn, J. and Schneider, A.F., 2011. Modern Design of Potroom Ventilation. *TMS-Light Metals*, p. 531–535.
- Yu, H.L., Cui, Q.L., Liu, X.H., Zhao, X.M. and Tian, T.L., 2004. Analysis of 3D Thermo-Electric Field Potential for 300 kA Aluminum Electrolysis Cell Using ANSYS. *Non-Ferrous Mining and Metallurgy* 3, p. 009.
- Yurkov, V. and Mann, V., 2005. A Simple Dynamic Realtime Model for Aluminum Reduction Cell Control System. *TMS-Light Metals*, 423-428.
- Zhai, Z., Zhang, Z., Zhang, W. and Chen, Q., 2007. Evaluation of Various Turbulence Models in Predicting Airflow and Turbulence in Enclosed Environments by CFD: Part 1—Summary of Prevalent Turbulence Models. *Hvac&R Research* 13 (6), p. 853-870.
- Zhang, H., Li, J., Wang, Z., Xu, Y. and Lai, Y., 2010. The Numerical Modeling of Melt Flow and MHD Instabilities in an Aluminum Reduction Cell. *JOM* 62 (11), p. 26-31.
- Zhang, Z., Zhang, W., Zhai, Z. and Chen, Q., 2007. Evaluation of Various Turbulence Models in Predicting Airflow and Turbulence in Enclosed Environments by CFD: Part 2—Comparison with Experimental Data from Literature. *Hvac&R Research* 13 (6), p. 871-886.
- Zhao, R., Gosselin, L., Ousegui, A., Fafard, M. and Ziegler D.P., 2013. Heat Transfer and Airflow Analysis in the Upper Part of Electrolytic Cells Based on CFD.” *Numerical Heat Transfer, Part A: Applications* 64 (4), p. 317-338.
- Zhao, R., Gosselin, L., Fafard, M. and Ziegler D.P., 2013a. Heat Transfer in Upper Part of Electrolytic Cells: Thermal Circuit and Sensitivity Analysis. *Applied Thermal Engineering* 54 (1), p. 212–225.

- Zhao, R., Gosselin, L., Fafard, M. and Ziegler D.P., 2013b. Reduced Ventilation of Upper Part of Aluminum Smelting Pot: Potential Benefits, Drawbacks, and Design Modifications. *TMS-Light Metals*, p. 805–810.
- Zhao, R. and Gosselin, L., Natural Ventilation of a Tall Industrial Builindg: Investigation on the Impact of Modeling Assumptions. *eSim 2014*, May 7-10th, Ottawa.
- Zhao, R., Gosselin, L., and Tessier, J., 2014. Airflow and Thermal Conditions in Aluminum Smelting Potrooms under Different Conditions. *Building Services Engineering Research and Technology*, under review.
- Zueco, J. and Campo, A., 2006. Network Model for the Numerical Simulation of Transient Radiative Transfer Process between the Thick Walls of Enclosures. *Applied Thermal Engineering* 26 (7), p. 673–79.

APPENDIX

Detailed expressions of the main resistances involved in the thermal circuit of Fig. 2.2

	Equation	Description
R ₁	$\frac{1}{\dot{m}_{\text{air}} C_{p,\text{air}}}$ <p>\dot{m}_{air} : mass flow rate of the exhaust gas</p> <p>$C_{p,\text{air}}$: specific heat of air</p>	Ventilation in the cavity with potroom air
R ₂	$\frac{1}{\dot{m}_{\text{CO}_2} C_{p,\text{CO}_2}}$ <p>\dot{m}_{CO_2} : mass flow rate of the hot gas from bath</p> <p>C_{p,CO_2} : specific heat of CO₂</p>	Hot gas (CO ₂) released from the bath into the cavity
R ₃	$\frac{L_{\text{superhood}}}{k_{\text{al}} A_{\text{superhood}}} + \frac{1}{h_{\text{eff}} A_{\text{superhood}}}$ <p>h_{eff} : effective heat transfer coef. on the external surface of hoods and superstructure</p> <p>k_{al}: thermal conductivity of hood and super-structure</p> <p>$L_{\text{superhood}}$=0.01m, thickness of hoods and super-structure</p> <p>$A_{\text{superhood}}$=1.61m², total surface area of hoods and superstructure</p>	Total thermal resistance between internal surface of superstructure and hoods, and the ambient
R ₄	$\frac{1}{h_{\text{superhood}} A_{\text{superhood}}}$ <p>$h_{\text{superhood}}$: convective coef. on the internal surface of hoods and superstructure, Table 1</p> <p>$A_{\text{superhood}}$=2.37m², area of the surfaces of hoods and superstructure</p>	Convection resistance between the internal surface of superstructure and hoods, and gases in the cavity

R5	$\frac{1}{h_{\text{cover}} A_{\text{cover}}}$ <p>h_{cover}: convective coef. on the top surface of anode cover, Table 1</p> <p>$A_{\text{cover}}=1.33\text{m}^2$, area of the top surface of anode cover</p>	Convection resistance between top surface of anode cover, and gases in cavity
R6	$\frac{1}{h_{\text{bath-crust}} A_{\text{crust}}} + \frac{L_{\text{crust}}}{k_{\text{crust}} A_{\text{crust}}} + \frac{L_{\text{cover1}}}{k_{\text{cover}} A_{\text{crust}}}$ <p>$h_{\text{bath-crust}}$: effective heat transfer coef. from bath to crust</p> <p>k_{crust}: thermal conductivity of crust</p> <p>k_{cover}: thermal conductivity of cover</p> <p>$L_{\text{crust}}=0.05\text{m}$, thickness of crust</p> <p>$L_{\text{cover1}}=0.1\text{m}$, thickness of the anode cover on crust</p> <p>$A_{\text{crust}}=0.38\text{m}^2$, area of the bottom surface of crust facing the bath</p> <p>$A_{\text{cover1}}=A_{\text{crust}}$</p>	Total thermal resistance through the hot gas layer, crust and anode cover (note that there are three individual resistances in Fig. 2.2b)
R7	$\frac{L_{\text{cover2}}}{k_{\text{cover}} A_{\text{cover2}}}$ <p>$L_{\text{cover2}}=0.1\text{ m}$, thickness of the anode cover on anode</p> <p>$A_{\text{cover2}}=0.87\text{m}^2$, area of the anode cover on anode</p> <p>$A_{\text{stub, cross-section}}= 0.025\text{m}^2$, area of the cross-section of stub</p>	Conduction resistance of the anode cover on the top of the anode
R8	$\frac{1}{\left(\frac{2}{r_2} + \frac{1}{r_6}\right) + \left(\frac{T_{\text{yoke}} - T_{\text{gas}}}{T_{\text{stub}} - T_{\text{gas}}}\right) \frac{2}{r_4}}$ <p>$r_{2,4,6}$: equivalent convection resistances in yoke and stubs, as shown in Fig. 2.3b</p>	Equivalent convection resistance for the structure in Fig. 2.3b.

R ₉	$\frac{T_{\text{anode}} - T_{\text{stub}}}{q_9} = \frac{T_{\text{anode}} - T_{\text{stub}}}{k_{\text{st2}} A} \times$ $\left[\left(T_{\text{anode}} + \frac{n}{m^2} \right) m \sin(mL) - \left(\frac{T_{\text{stub}} + \frac{n}{m^2} - (T_{\text{anode}} + \frac{n}{m^2}) \cos(mL)}{\sin(mL)} \right) \cos(mL) \right]^{-1}$ <p>q₉: heat flux through three stubs immersed in cover k_{st2}: thermal conductivity of stubs immersed in cover m, n: fin parameters in Eq. (2.8) L=0.15 m, length of the stubs immersed in cover A=0.076m², three times the area for one stub</p>	Equivalent resistance of the portion of stubs immersed in the cover with Joule heating
R ₁₀	$\frac{1}{\frac{k_{\text{anode}} A_{\text{anode}}}{H} + \frac{I^2 \rho_{\text{anode}} H}{2A_{\text{anode}} (T_{\text{bath}} - T_{\text{anode}})}}$ <p>k_{anode} : thermal conductivity of carbon ρ_{eanode}: electrical resistivity of carbon H=0.3 m, height of anodic block, reference case A_{anode}= 0.943m², area of the cross-section of carbon anode</p>	Equivalent resistance of anode with Joule heating
R ₁₁	$\frac{T_{\text{collar}} - T_{\text{atm}}}{q_{11} + q_{\text{jh11}}} =$ $\frac{(T_{\text{collar}} - T_{\text{atm}})}{k_{\text{al}} A m \left[\left(T_{\text{collar}} - T_{\text{atm}} - \frac{n}{m^2} \right) \cosh(mL) + \frac{n}{m^2} \right] \frac{1}{\sinh(mL)} + \frac{I^2 \int_0^L (a+bT) dx}{A}}$ <p>q₁₁: heat flux through the note of collar in Fig. 2.2b qq_{jh11}: heat source due to joule heating in the rod outside of pot I: current through one rod m, n: parameters, see Eq. (2.18)</p>	Equivalent resistance of the rod extending out of the pot

	<p>k_{al}: thermal conductivity of aluminum rod</p> <p>$L=1.4$ m, length of the rod from collar to the top</p> <p>$A=0.022\text{m}^2$, area of the cross-section of rod</p>	
R_{12}	$\frac{T_{rod} - T_{gas}}{q_{12}} = \frac{\theta_b}{h_{rod} P \int_0^L \theta(x) dx}$ <p>q_{12}: convection heat transfer rate from rod to gas in cavity</p> <p>h_{rod}: convection coef. on the surface of rod, see Table 2.1</p> <p>$\theta_b = T_{rod} - T_{gas}$</p> <p>$P=0.6\text{m}$, perimeter of rod</p> <p>$L=0.6$ m, length of the rod in cavity</p>	Equivalent convection resistance between the rod and the gas in the cavity
R_{13}	$\frac{T_{rod} - T_{collar}}{q_{13}} = \frac{(\theta_b - \theta_L) \sinh mL}{k A m \left[\theta_b - \frac{n}{m^2} - \left(\theta_L - \frac{n}{m^2} \right) \cosh mL \right]}$ <p>q_{13}: heat flux through the node of collar in Fig. 2.2b</p> <p>m, n: fin parameters in Eq. (2.15)</p> <p>$\theta_b = T_{rod} - T_{gas}$</p> <p>$\theta_L = T_{collar} - T_{gas}$</p> <p>$k$: thermal conductivity of aluminum rod</p> <p>$L=0.6$ m, length of the rod in cavity</p> <p>$A=0.022\text{m}^2$, area of the cross-section surface of rod</p>	Equivalent resistance of the rod in the cavity
R_{14}	$\frac{1}{\frac{1}{r_5} + \left(\frac{T_{yoke} - T_{rod}}{T_{stub} - T_{rod}} \right) \frac{2}{r_3}}$ <p>$r_{3,5}$: equivalent conduction resistances in yoke and stubs, as shown in Fig. 2.3b</p>	Equivalent conduction resistance in the structure on Fig. 2.3b

